

August 2016

# Electrical Measurements and Attenuated Total Reflection Infrared Spectroscopic Study of Aromatic Isocyanides and Thiols on Gold

Rasha Khaled Abuflaha  
*University of Wisconsin-Milwaukee*

Follow this and additional works at: <https://dc.uwm.edu/etd>

 Part of the [Chemistry Commons](#)

---

## Recommended Citation

Abuflaha, Rasha Khaled, "Electrical Measurements and Attenuated Total Reflection Infrared Spectroscopic Study of Aromatic Isocyanides and Thiols on Gold" (2016). *Theses and Dissertations*. 1328.  
<https://dc.uwm.edu/etd/1328>

This Dissertation is brought to you for free and open access by UWM Digital Commons. It has been accepted for inclusion in Theses and Dissertations by an authorized administrator of UWM Digital Commons. For more information, please contact [open-access@uwm.edu](mailto:open-access@uwm.edu).

ELECTRICAL MEASUREMENTS AND ATTENUATED TOTAL  
REFLECTION INFRARED SPECTROSCOPIC STUDY OF  
AROMATIC ISOCYANIDES AND THIOLS ON GOLD

by

Rasha K. Abuflaha

A Dissertation Submitted in  
Partial Fulfillment of the  
Requirements for the Degree of

Doctor of Philosophy  
in Chemistry

at

The University of Wisconsin-Milwaukee

August 2016

## ABSTRACT

# ELECTRICAL MEASUREMENTS AND ATTENUATED TOTAL REFLECTION INFRARED SPECTROSCOPIC STUDY OF AROMATIC ISOCYANIDES AND THIOLS ON GOLD

by

Rasha K. Abuflaha

The University of Wisconsin-Milwaukee, 2016  
Under the Supervision of Professor W. T. Tysoe

In 1947, Bell Laboratories produced an amplifier design in which an electric field would enhance the flow of electrons near the surface of a layer of silicon, it was called the “point-contact transistor”, the world’s first semiconductor amplifier. In order to minimize the electronic circuit elements (device miniaturization), the ability to utilize single molecules that function as self-contained electronic devices (molecular electronics) has motivated researchers around the world. Molecular electronics investigates single molecules and collections of molecules assembled into electronic circuits. Currently, semiconductor devices are fabricated using a “top-down” approach that employs lithographic and etch techniques to pattern a substrate, but as feature sizes decrease, the top-down approach becomes challenging. As a result, circuits are synthesized using a “bottom-up” approach that builds small structures from molecules.

In 1959, Nobel Laureate Richard Feynman gave his famous lecture “There's Plenty of Room at the Bottom” to an American Physical Society meeting at Caltech, where he he discussed the use of single molecules or atoms to build nano-devices, sizes that cannot be built using traditional lithographic techniques.

In 1974, Aviram and Ratner postulated a very simple electronic device, based on the use of a single organic molecule, and by modulating HOMO and LUMO orbitals to produce a ‘molecular rectifier’.

In this work, a new strategy for building molecular electronics is investigated; by using different organic linkers that self-assemble and bridge gold nanoparticles in order to create electron-transfer pathways between them. This involves measuring the electrical properties and surface structures of isocyanide- and thiol-terminated aromatic molecules. It was found that diisocyanides and dithiols with one, two, and three benzene rings can form oligomeric chains linking between gold nanoparticle arrays on mica in order to decrease the tunneling barrier and enhance the conductivity. The results showed that these molecules generally form oligomeric bridges when dosed on gold-nanoparticle arrays, and that the tunneling barrier can be affected by the number of phenyl rings for each molecule where it was observed that the energy barrier increased when increasing the molecular length (number of benzene rings) of the linker molecule. For example, the slopes of plots of  $\ln$  (film resistance *versus*  $1/\sqrt{T}$ , denoted  $\alpha$  *versus*  $\ln(R_o)$ , where  $R_o$  is the resistance of the initial nanoparticle array before dosing, for 1,4-benzenedithiol (BDT), 4,4'-biphenyldithiol (BPDT), and 4,4''-terphenyldithiol (TPDT) were analyzed to show that the height of the tunneling barrier increases with increasing number of benzene rings, which means that increased extent of conjugation does not necessarily lead to lower tunneling barrier. Biphenyl and terphenyl molecules can adopt a twisted ring

configuration which appears to be observed for BPDT and TPDT. This distortion may decrease the conjugation by reducing the orbital overlap between adjacent aromatic rings. Consequently, the poly-phenyl dithiol molecules have higher tunneling barrier than benzene dithiol (*Chapter 6*).

Similar to dithiols, the tunneling barrier of diisocyanides increases when increasing the number of phenyl rings. Diisocyanides with one, two and three benzene rings can also adopt a twisted ring configuration. As a result, a possible reason for the increase in the height of the tunneling barrier as the number of benzene rings increases, is a reduced orbital overlap between adjacent benzene rings because of twisting. An alternative possibility is that increasing the number of phenyl rings increases the electron donation to the gold that leaves a partial positive charge on the isocyanide molecule which leads to a lowering the molecular orbital energies and moves the HOMO orbital away from the Fermi level, as evidenced by variations in the isocyanide stretching frequencies (*Chapter 7*).

The properties of an asymmetric molecule containing both isocyanide and sulfur groups are investigated by studying the surface structure and electrical properties by dosing gold films with 4,4'-disulfanediyldibenzoisonitrile (DBN) from solution. It is found that DBN has ability to form oligomers between gold nanoparticles and contributes to tuning the gold Fermi level and decrease the height of the electron tunneling barrier. The ATR-IR spectra provide information that is complementary to the electrical measurements and allow the surface structure of DBN molecules on the gold-nanoparticle array to be determined.

In *Chapter 9*, back-gating behavior was explored for three different linker molecules; an external field was applied using a back-gated device in order to modulate the conductivity of molecular wires that bridge gold nanoparticles in a granular thin film. It was found that the external field effect could both modulate the energy of the molecular orbitals (HOMO) of the molecular

wire to influence their alignment with respect to the Fermi level of gold nanoparticles, as well as polarizing charge from the gold nanoparticles, thereby modulating the current through the molecular layer. The field effect-conductivity results showed a small increase in the conductivity with increasing gate potential of either sign. Electrical measurements were performed using 1,4-PDI-, 1,4-BDT- and 1,3-BDT-linked gold nanoparticles where the maximum sheet resistance changes were ~1.5 to 2.3%. At a sample temperature of ~110K, for what the sheet resistance changed by 4.5% under a negative bias.

These results show that it is possible to form molecules linkages between gold nanoelectrodes by attaching the molecules either using isocyanide or sulfur groups, suggesting that this is a promising strategy for eventually fabricating molecular electronic circuits.

□

© Copyright by Rasha K. Abuflaha, 2016  
All Rights Reserved

*For my mother*

*In memory of my father*

*For my brothers, Ameer and Yazan*

*For my husband*

*For my children, Zain and Kenan*



# TABLE OF CONTENTS

<b>Chapter 1: Introduction</b> .....	1
<b>Chapter 2: Experimental Methods</b> .....	8
2.1 High Vacuum System .....	8
2.2 High Vacuum (HV) Chambers .....	9
2.3 Conductivity Measurement Chamber .....	9
2.4 Vacuum Pumps .....	12
2.4.1 Mechanical (rotary vane) Pump.....	12
2.4.2 Turbomolecular Pumps .....	13
2.4.3 Oil Diffusion Pumps .....	14
2.4.4 Ion Pumps (Sputter-ion pumps).....	15
2.5 Metal Thermal Evaporator .....	16
2.6 Sample Preparation .....	18
2.7 Attenuated Total Reflection Infrared Spectroscopy (ATR-IR) .....	20
2.7.1 ATR-IR Principle and Theory .....	20
<b>Chapter 3: Experimental and Theoretical Methods</b> .....	25
3.1 Introduction.....	25
3.2 Experimental .....	28
3.3 Results.....	30
3.4 Discussion.....	32
3.4.1 Theoretical Aspects (Abeles Theory of Conduction in Granular Materials).....	33
3.5 Conclusion .....	40
<b>Chapter 4: Surface Chemistry and Structures of 1,4-phenylene Diisocyanide on Gold Films from Solution</b> .....	41
4.1 Introduction.....	41
4.2 Experimental Methods .....	43
4.3 Results.....	44
4.4 Discussion.....	47
4.5 Conclusions.....	50
<b>Chapter 5: Surface Chemistry and Electrical Properties of 1,4-Benzendithiol and 1,3-Benzendithiol Oligomers Bridging Between Gold Nanoparticles On Mica</b> .....	54
5.1 Introduction.....	54

5.2 Experimental .....	56
5.3 Results .....	57
5.3.1 Electrical studies .....	57
5.3.2 Attenuated total internal reflection infrared spectroscopy (ATR-IR) characteristics .....	64
5.4 Discussion .....	68
5.5 Conclusion .....	73
<b>Chapter 6: Surface Chemistry and Electron Transport of 4,4'-Biphenyldiisocyanide and 4,4''-Terphenyldiisocyanide on Gold Films from Solution .....</b>	<b>75</b>
6.1 Introduction .....	75
6.2 Experimental .....	77
6.3 Results .....	78
6.3.1 Electrical Studies .....	78
6.3.2 Attenuated total internal reflection infrared spectroscopy (ATR-IR) characteristics .....	83
6.4 Discussion .....	89
6.5 Conclusion .....	92
<b>Chapter 7: Surface Chemistry and Electron Transport of 4,4'-Biphenyldithiol and 4,4''-Terphenyldithiol on Gold Films From Solution .....</b>	<b>94</b>
7.1 Introduction .....	94
7.2 Experimental .....	95
7.3 Results .....	97
7.3.1 Electrical measurements .....	97
7.3.2 Attenuated total internal reflection infrared spectroscopy (ATR-IR) measurements .....	100
7.4 Discussion .....	104
7.5 Conclusion .....	106
<b>Chapter 8: Asymmetric Electron Linker Molecule and Conductivity Measurements of 4,4'-Disulfanediylidibenzoisonitrile on Gold Films from Solution .....</b>	<b>108</b>
8.1 Introduction .....	108
8.2 Experimental .....	109
8.3 Results .....	110
8.3.1 Electrical studies .....	110
8.3.2 Attenuated total internal reflection infrared spectroscopy (ATR-IR) characteristics .....	112
8.4 Discussion .....	114
8.5 Conclusion .....	115

<b>Chapter 9: Back-Gate Modulation of Conductivity of Molecular Conductors</b> .....	117
9.1 Introduction.....	117
9.2 Theoretical aspects.....	122
9.3 Device fabrication and experimental setup.....	124
9.4 Results.....	126
9.5 Discussion.....	131
9.6 Conclusion .....	132
<b>Chapter 10: Conclusions</b> .....	135
<b>Curriculum vitae</b> .....	139

## LIST OF FIGURES

<b>Figure 1.1:</b> Molecular rectifier proposed by Aviram and Ratner, D- $\sigma$ -A molecule .....	2
<b>Figure 2.1:</b> Diagram of a stainless steel high-vacuum chamber.....	9
<b>Figure 2.2:</b> A typical combination for the electrical measurements chamber.....	11
<b>Figure 2.3:</b> An illustration for mica substrate placed on the copper sample holder and connected to feedthroughs using fine alligator clips.....	11
<b>Figure 2.4:</b> Block diagram of I/V measurement instrumentation .....	12
<b>Figure 2.5:</b> Rotary Mechanical Pump schematic .....	13
<b>Figure 2.6:</b> Turbomolecular pump schematic.....	14
<b>Figure 2.7:</b> Oil diffusion pump schematic.....	15
<b>Figure 2.8:</b> Ion pump schematic and operation .....	16
<b>Figure 2.9:</b> A) Cook Vacuum Products CVE 301 thermal evaporator. B) Inside the evaporator, tungsten basket filaments, pre-wetted with high purity gold .....	17
<b>Figure 2.10</b> Control the gold film thickness inside the evaporator .....	18
<b>Figure 2.11:</b> A multiple reflection across an ATR crystal .....	21
<b>Figure 2.12:</b> Illustration shows refractive index of crystal > sample .....	21
<b>Figure 2.13:</b> A single reflection ATR.....	22
<b>Figure 3.1:</b> Time-dependent sequence of images of Au-PDI chains collected every 53 seconds scanning a $5.0 \times 5.0 \text{ nm}^2$ region. A dotted line showing the chains has been included as a guide to the eye .....	26
<b>Figure 3.2:</b> Sequence of images of Au-PDI oligomers linking between gold nanoparticles on a Au(111) surface where the location of the nanoparticles is indicated by A, B and C .....	26

<b>Figure 3.3:</b> AFM image of a continuous film that represents a gold electrode (region A), and a nanoparticle array (dielectric regime as shown in region B) on mica substrate .....	28
<b>Figure 3.4:</b> Gold nanoparticles aging process. In this sample, the initial conductivity was 3.0 nS, the sample aged to ~0.6 nS. ....	29
<b>Figure 3.5:</b> Typical curve shows the increase in conductivity across a granular film as a function of 1,4-PDI dosing time. $R_0$ is the sheet resistance of the clean gold film before dosing. The inset shows a schematic depiction of the oligomer-linked nanoparticles .....	30
<b>Figure 3.6:</b> Typical plots of $\ln(R/\Omega)$ versus $T^{-1/2}$ , where the temperature is measured in degrees in Kelvin for various films with a range of initial films resistances. The value of the initials resistance values of the films, $R_0$ , are indicated on each of the plots.....	31
<b>Figure 3.7:</b> Plot of $\alpha$ values versus $\ln(R_0/\Omega)$ for the 12 films studied in this chapter. The linear is in agreement with the theory of activated tunneling in granular materials put forth by Abeles and Sheng. ....	32
<b>Figure 3.8:</b> Energy level diagram for gold nanoparticles linked by 1,4-PDI oligomers, where $\phi_C$ corresponds to the work function of the 1,4-PDI-covered gold nanoparticles (4.08 eV) and $\phi F$ is the tunneling barrier through the linker molecule measured to be $0.10 \pm 0.02$ eV.....	39
<b>Figure 4.1:</b> A series of ATR infrared spectra of PDI adsorbed on a thin gold film using aliquots of 200 $\mu$ l of solution of 0.5 mM PDI. The resulting PDI doses, in nmole/cm <sup>2</sup> , are indicated adjacent to the corresponding spectrum. ....	46
<b>Figure 4.2:</b> Plot of the conductivity of gold nanoparticles deposited onto a mica substrate, with an initial conductivity of 0.5 nS (nanoSiemens) after exposure to 50 $\mu$ l of serially diluted solutions of PDI in benzene as a function of the solution dose in nmole/cm <sup>2</sup> . ....	48
<b>Figure 5.1:</b> Large-area STM scan of a saturated layer of 1,4-BDT adsorbed on gold at 300 K ( $I_t = 163$ pA, $V_t = 0.25$ V) showing the formation of trans-induced zigzag oligomeric chains	55
<b>Figure 5.2:</b> Saturation dose of 1,3-BDT on Au(111). The crystal was dosed and imaged at room temperature. No sign of ordered structures were observed under these conditions .....	55
<b>Figure 5.3:</b> Variation in conductivity as a function of (a) 1,4-BDT and (b) 1,3-BDT dose in (mmoles/cm <sup>2</sup> ) measured when dosing a gold-nanoparticle-covered mica surface with an initial sheet resistance $R_0$ of $\ln(R_0/\Omega) = 21.4$ , from solution.....	58

**Figure 5.4:** Typical plots of  $\ln(R/\Omega)$  versus  $T^{-1/2}$ , for a) 1,4-BDT-linked gold nanoparticles, b) 1,3-BDT-linked gold nanoparticles, where the temperature is measured in degrees in Kelvin for various films with a range of initial films resistances. The value of the initial resistance values of the films,  $R_0$ , are indicated on each of the plots..... 60

**Figure 5.5:** Plot of  $\alpha$  values versus  $\ln(R_0)$  for the 13 different films obtained for 1,4-BDT linked gold nanoparticles, with a slope of  $4.2 \pm 0.1$ . The linear fit is in agreement with the theory of activated tunneling in granular materials put forth by Abeles and Sheng ..... 61

**Figure 5.6:** Plot of  $\alpha$  values versus  $\ln$  for the 15 different films obtained for 1,3-BDT linked gold nanoparticles. Black dots represent alpha values for samples with initial conductivities vary between 6.00 and 15.00 nS, orange dots represent alpha values for samples with initial conductivities vary between 1.00 and 5.00 nS ..... 62

**Figure 5.7:** Plot of  $\ln(C_s/C_0)$  as a function of the  $\ln(R_0/\Omega)$ , where  $R_0$  is the resistance after dosing 0.3 mmol/cm<sup>2</sup> of 1,3-BDT, shows that samples with low initial gold coverage (orange squares) produce low conductivity even after dosing 1,3-BDT, whereas samples with high initial coverage (black squares) produce high conductivity after dosing 1,3-BDT ..... 63

**Figure 5.8:** Plot of  $\alpha$  values for 1,3-BDT linked gold nanoparticles for samples with high initial conductivity ( $> 5.00$  nS), the slope is equal to  $4.6 \pm 0.3$  ..... 64

**Figure 5.9:** A series of ATR infrared spectra of 1,4-BDT adsorbed on a thin gold film using aliquots of 200  $\mu$ l of solution of 0.1 mM 1,4-BDT. The resulting BDT doses, in mole/cm<sup>2</sup>, are indicated adjacent to the corresponding spectrum. The inset is a spectrum of 0.1 mM solution of pure 1,4-BDT in benzene ..... 65

**Figure 5.10:** A series of ATR infrared spectra of 1,3-BDT adsorbed on a thin gold film using aliquots of 200  $\mu$ l of solution of 0.1 mM 1,3-BDT. The resulting BDT doses, in mole/cm<sup>2</sup>, are indicated adjacent to the corresponding spectrum. The inset is spectrum of 0.1 mM solution of pure 1,3-BDT in benzene. .... 66

**Figure 5.11:** Most stable structures obtained by DFT calculations for  $\eta^1$ -thiolates from 1,4-BDT adsorbed on Au(111) surfaces: (a) a hollow site ( $E_{ads} = 174$  kJ/mol) (b) a bridge site ( $E_{ads} = 172$  kJ/mol), and (c) on a gold adatom ( $E_{ads} = 226$  kJ/mol)..... 70

**Figure 5.12:** Structures obtained by DFT calculations for 1,3-BDT adsorbed on Au(111) surfaces: (a) top view of  $\eta^1$  adatom complex of 1,3-BDT ( $E_{ads} = -180$  kJ/mol) (b) One thiol is bonded to a gold adatom and the other to the hollow site of Au(111) surface ( $E_{ads} = -321$  kJ/mol), and (c) both thiolates are bonded to gold adatoms ( $E_{ads} = 381$  kJ/mol)..... 71

**Figure 6.1:** Plot of the conductivity of gold nanoparticles deposited onto a mica substrate, with an initial conductivity of 0.4 nS ( $\ln(R_o/\Omega) = 21.9$ ) after exposure to aliquots of (a) 0.005 mM BPDI in benzene as a function of the solution dose in nmole/cm<sup>2</sup>, and (b) 0.005 mM TPDI in benzene as a function of the solution dose in nmole/cm<sup>2</sup> ..... 79

**Figure 6.2:** The linear  $\ln(R)$  versus  $T^{-1/2}$  dependence for a sample with initial conductivity of 3.00 nS dosed with 0.15  $\mu\text{mole/cm}^2$  BPDI, is predicted by the model of Abeles and Sheng.  $R_o$  is the sheet resistance of the film prior to dosing ..... 80

**Figure 6.3:** Indicative of the formation of Au-BPDI oligomers between nanoparticles, the values of  $\alpha$  scale linearly with  $\ln(R_o)$ . The slope of the plot for BPDI is  $9.0 \pm 0.3$  ..... 81

**Figure 6.4:** The linear  $\ln(R)$  versus  $T^{-1/2}$  dependence for a sample with initial conductivity of 4.5 nS dosed with 0.15  $\mu\text{mole/cm}^2$  BPDI, is predicted by the model of Abeles and Sheng.  $R_o$  is the sheet resistance of the film prior to dosing ..... 82

**Figure 6.5:** Indicative of the formation of Au-TPDI oligomers between nanoparticles, the values of  $\alpha$  scale linearly with  $\ln(R_o)$ . The slope of the plot for TPDI is  $10.8 \pm 0.4$  ..... 82

**Figure 6.6:** A series of ATR infrared spectra of BPDI adsorbed on a thin gold film using aliquots of 0.005 mM BPDI. The resulting BPDI doses, in nmole/cm<sup>2</sup>, are indicated adjacent to the corresponding spectrum. .... 83

**Figure 6.7:** The variation in intensities of the 2161 and 2121 cm<sup>-1</sup> vibrational frequencies as a function of BPDI dose (in nmoles/cm<sup>2</sup>). ..... 84

**Figure 6.8:** A series of ATR infrared spectra of TPDI adsorbed on a thin gold film using aliquots of 0.005 mM TPDI. The resulting TPDI doses, in nmole/cm<sup>2</sup>, are indicated adjacent to the corresponding spectrum. .... 87

**Figure 6.9:** The variation in intensities of the 2167 and 2122 cm<sup>-1</sup> vibrational frequencies as a function of TPDI dose (in nmoles/cm<sup>2</sup>). ..... 88

**Figure 7.1:** Plot of the conductivity of gold nanoparticles deposited onto a mica substrate (a) change in conductivity as a function of the BPDT solution dose in nmole/cm<sup>2</sup> for mica sample with initial resistance of  $\sim 200 \text{ M}\Omega$  dosed with 0.05 mM BPDT in benzene. (b) Change in conductivity as a function of the TPDT solution dose in nmole/cm<sup>2</sup> for mica sample with initial resistance of  $\sim 600 \text{ M}\Omega$  dosed with 0.05 mM TPDT in benzene. .... 98

**Figure 7.2:** The linear  $\ln(R)$  versus  $T^{-1/2}$  dependence for two different samples is predicted by the model of Abeles and Sheng.  $R_o$  sheet resistance of the film prior to dosing, and scales with gold coverage. a) Gold nanoparticles with initial coverage of 15.00 nS linked with BPDT molecules and b) gold nanoparticles with initial coverage of 5.0 nS linked with TPDT..... 98

**Figure 7.3.** Indicative of the formation of Au-BPDT oligomers between nanoparticles, the values of  $\alpha$  scale linearly with  $\ln(R_o)$ . The slope of the plot for BPDT is  $8.3 \pm 0.4$  ..... 99

**Figure 7.4.** Indicative of the formation of Au-TPDT oligomers between nanoparticles, the values of  $\alpha$  scale linearly with  $\ln(R_o)$ . The slope of the plot for TPDT is  $11.4 \pm 0.4$ ..... 100

**Figure 7.5:** A series of ATR infrared spectra of BPDT adsorbed on a thin gold film using aliquots of 200  $\mu$ l of solution of 0.1 mM BPDT. The resulting BPDT doses, in nmole/cm<sup>2</sup>, are indicated adjacent to the corresponding spectrum. The inset is a spectrum of 0.1 mM solution of pure BPDT in benzene. .... 101

**Figure 7.6:** A series of ATR infrared spectra of TPDT adsorbed on a thin gold film using aliquots of 200  $\mu$ l of solution of 0.1 mM TPDT. The resulting TPDT doses, in mole/cm<sup>2</sup>, are indicated adjacent to the corresponding spectrum. The inset is a spectrum of 0.1 mM solution of pure TPDT in benzene ..... 102

**Figure 8.1:** Structure of 4,4'-Disulfanediyldibenzoisonitrile (DBN) ..... 109

**Figure 8.2:** Variation in conductivity as a function of DBN dose in nmoles/cm<sup>2</sup> measured when dosing a gold-nanoparticle-covered mica surface with an initial sheet resistance  $R_o$  of  $\ln(R_o/\Omega) = 19.47$ , from solution ..... 111

**Figure 8.3:** The linear  $\ln(R)$  versus  $T^{-1/2}$  dependence for a sample with initial conductivity of 15.3 nS dosed with 0.1  $\mu$ mole/cm<sup>2</sup> BPDI, is predicted by the model of Abeles and Sheng.  $R_o$  is the sheet resistance of the film prior to dosing..... 111

**Figure 8.4:** Plot of  $\alpha$  values versus  $\ln(R_o)$  for the 8 different films obtained for DBN-linked gold nanoparticles, with a slope of  $7.4 \pm 0.3$ . The linear fit is in agreement with the theory of activated tunneling in granular materials put forth by Abeles and Sheng ..... 112

**Figure 8.5** A series of ATR infrared spectra of DBN adsorbed on a thin gold film using aliquots of 200  $\mu$ l of solution of 0.1 mM DBN .The resulting isocyanothiol doses, in mole/cm<sup>2</sup>, are indicated adjacent to the corresponding spectrum. The inset is a spectrum of 0.1 mM solution of pure DBN in benzene ..... 113



<b>Figure 8.6:</b> DBN after adsorbing on a gold nanoparticle array .....	115
<b>Figure 9.1:</b> a) The Lilienfeld transistor patent in 1930. B) The first prototype of a working field-effect transistor demonstrated by Bell labs. c) The first Integrated Circuit of Jack Kilby and Robert Noyce.....	117
<b>Figure 9.2</b> A typical layout of field-effect transistor, consisting of a source and drain electrodes, a gate, a gate dielectric and a semiconductor .....	119
<b>Figure 9.3:</b> Schematic drawing of a single electron transistor with a metallic island that is isolated from the source, drain, and gate electrodes using a tunneling junction.....	120
<b>Figure 9.4:</b> a) Simplified model for gain charging. b) Energy of different charge states as a function of gate voltage.....	123
<b>Figure 9.5</b> a) Sample configuration for field effect measurements. b) Experimental setup for the field-effect device where the gold nanoparticles are linked with organic molecules. ....	125
<b>Figure 9.6:</b> Typical curve showing dramatic enhancement in conductivity across a granular film as a function of 1,4-PDI dosing .....	127
<b>Figure 9.7:</b> Temperature dependence of a granular gold film with 1,4-phenylene diisocyanide (1,4-PDI linkers in a field-effect device.....	128
<b>Figure 9.8:</b> An ambipolar field-effect in a granular gold film with 1,4-phenylene diisocyanide (1,4-PDI linkers, at ~110 K.....	128
<b>Figure 9.9:</b> 1,4-BDT dosed film (813 M $\Omega$ $\rightarrow$ 10.74 M $\Omega$ ). a) Upper curve acquired at room temperature. The lower curve acquired at ~110K. b) Proposed theoretical prediction of a quadratic dependence of charge state energy as a function of gate voltage, and a linear component that corresponds to a change in energy alignment compared to the gold Fermi levels.....	130
<b>Figure 9.10:</b> 1,3-BDT dosed film (235 M $\Omega$ $\rightarrow$ 25.10 M $\Omega$ ). The upper curve was acquired at room temperature. The lower curve acquired at ~95 K. ....	131

## LIST OF TABLES

<b>Table 5.1:</b> Vibrational frequencies and assignments of pure 1,4-BDT in solution, and adsorbed on a gold nanoparticle array.....	67
<b>Table 5.2:</b> Vibrational frequencies and assignments of pure 1,3-BDT in solution, and adsorbed on a gold nanoparticle array.....	68
<b>Table 6.1:</b> Vibrational frequencies and assignments of BPDI on gold.....	86
<b>Table 6.2:</b> Vibrational frequencies and assignments of TPDI on gold.....	89
<b>Table 7.1:</b> Vibrational frequencies and assignments for BPDT on gold.....	103
<b>Table 7.2:</b> Vibrational frequencies and assignments for TPDT on gold.....	104
<b>Table 8.1:</b> Comparison of vibrations of 1,4-BDT and DBN on gold film.....	114

## ACKNOWLEDGEMENTS

First and foremost, I want to thank my advisor, Prof. W.T. Tysoe. I thank him for his guidance, patience, encouragement, caring and support during the development of this work. He is unique example of a brilliant scientist and a great leader, who leads by example, whose actions come from passion, not position. Thank you Prof. Tysoe for teaching me how to be a part of a team, I am really honored to be one of your students.

I extend my sincerest thanks and appreciation to the members of my committee, Prof. Peter Geissinger, Prof. Dennis W. Bennett, Prof, Alan W. Schwabacher and Prof. Jorg C. Woehl; thank you for the feedback, directions, and assistance when I needed it. A special thanks to Prof Alan Schwabacher's group, particularly Tyler Fenske, for preparing the 4,4' Disulfanediylidibenzoisonitrile (DBN) compound as a part of this work.

Thanks are also extended to former and current group members. Dr. John Kestell, the first student I have met in Tysoe's group. He was my teacher and trainer; he is a very smart and creative scientist, and a really good friend, with his help we have accomplished much of what is presented in this dissertation. I would like to thank Dr. Mike Garvey for his support and valuable advice; he also performed the computational work presented here. Dr. Mausumi Mahapatra, a very patient and smart scientist, and a really good friend. Heather Adams, is also a good example of a hard worker who has passion about science, and a good friend who was always there when I needed support and encouragement.

Special thanks for the government of Jordan, Al al-bayt University, for their financial support through this project.

My mother (Soad), thank you for your unconditional love, care, concern and trust in me, this has made me a stronger person. Thank you for making your children the main priority in your life. I have done this to make you proud.

In memory of my father (Khalid), you have always believed in me, and wanted me to achieve the highest level of education. I wish I made you proud. Rest in peace.

My brothers (Ameer and Yazan), thank you for your love, encouragement and endless faith in me.

My husband (Ahmad), thank you for your love and support.

The sunshine of my life, my babies (Zain and Kenan), you two are my blessing, and you make my life worth living, you will never find anyone else in your life who loves, prays, cares and worries about you more than I do. You are my greatest motivation!

# Chapter 1

## Introduction

There are two possible strategies for constructing nanoscale electronic devices: either from the top down or from the bottom up. In the top-down approach, devices are made from bulk (macroscopic) materials. The best example of this is silicon integrated circuit technology. An integrated circuit is one in which circuit components such as transistors, diodes, resistors, capacitors etc. are an integral part of a small semiconductor chip [1]. At the moment, the most used top-down approach is photolithography. It has been used for decades to manufacture computer chips and produce structures smaller than 100 nm [2].

It was observed that, over the history of computing hardware, the number of transistors on integrated circuits doubles approximately every 18 months [3]. The Intel co-founder, Gordon E. Moore, predicted that that period for a doubling in chip performance is a combination of the effect of more transistors and their being faster [4]. According to Moore's law, the number of components in integrated circuits had doubled every year from the invention of the integrated circuit in 1958, until 1965 and predicted that the trend would continue "for at least ten years" [5]. His prediction has proven to be uncannily accurate, because the law is now used by the semiconductor industry to guide long-term planning and to set targets for research and development [6]. However, it is predicted that this trend will soon reach the limit of current photolithographic technology. Based on that, another route to making nanostructures has been proposed, the bottom-up route. Making electronic circuits by bottom-up techniques by using molecules as electronic components was first seriously discussed in the 1970s by Aviram and Ratner [7] when top-down integrated circuits still had fairly large dimensions. At that time, one of the major advantages of molecular electronics

was building circuits that are much denser and smaller than those possible by top-down technology. In this case, molecular building blocks are placed in the right environment and they assemble themselves into complicated structures. These approaches include the miniaturization of materials components (up to atomic level) with further self-assembly process leading to the formation of nanostructures. During self-assembly the physical forces operating at nanoscale are used to combine basic units into larger stable structures. Typical examples are quantum dot formation during epitaxial growth and formation of nanoparticles from colloidal dispersions [8].

Aviram and Ratner postulated a very simple electronic device, a rectifier, based on the use of a single organic molecule. Basically, an organic donor is linked via an inert spacer to an organic acceptor, the spacer is called the  $\sigma$  bridge, because it contains only saturated bonds (D- $\sigma$ -A) [9] as shown in *Figure 1.1*.

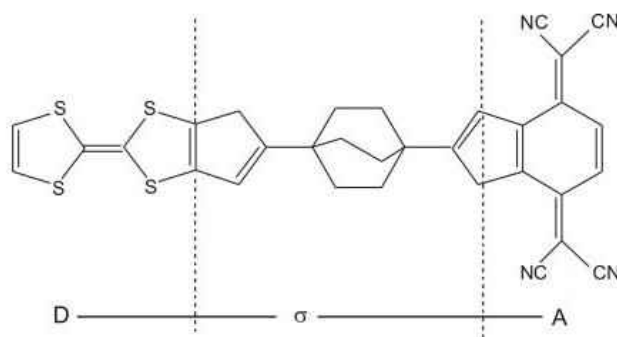


**Figure 1.1:** Molecular rectifier proposed by Aviram and Ratner, D- $\sigma$ -A molecule

Subsequently, experimental approaches were used to characterize transport properties by assembling monolayers on metal surfaces using a tip electrode in scanning tunneling microscopy (STM) [10], and the conductive probe atomic force microscopy (CP-AFM) [11], or by attaching

molecules in a mechanically controllable break junctions (MCBJ) to manipulate the electronic current at the atomic scale [12].

Aromatic compounds are of special interest in molecular transport. Their small highest occupied molecular orbital-lowest unoccupied molecular orbital (HOMO-LUMO) gap and functionalization capability make them attractive for potential molecular electronics applications. The molecular system of gold (Au)-sulfur on surfaces has been studied frequently owing to its facile fabrication [13]. Among various sulfur-containing adsorbates, aromatic thiols have attracted considerable attention because they show robust binding on gold [14]. Moreover, by taking advantage of two labile SH units and the delocalized  $\pi$ -electron conductivity, aromatic dithiol molecules have been introduced as a molecular alligator clip between electrode surfaces in molecular electronic devices [15].

Another interesting system is the organoisocyanides on metals. With a vertical orientation of isocyanides on many metal surfaces as well as the delocalized  $d\pi$ - $p\pi$  orbital system allowing electron density to shift between the metal and the molecule, a small contact barrier is expected. Isocyanides have also been suggested as possible “alligator clips” for molecular wires, and the electronic transport between metal contacts (gold or palladium) and 1,4-phenylenediisocyanide (PDI) [16] and longer diisocyanide phenylene oligomers has been explored [17].

In this work, the surface structure and transport properties of linked gold nanoparticles with self-assembled aromatic molecules terminated with thiolates (-SH) and/or isocyanide (-NC) “anchor groups” have been studied. This dissertation begins with discussing the requirement for working in high vacuum conditions ( $\sim 2 \times 10^{-8}$  Torr) and sample preparation techniques, as well as using attenuated total reflection infrared spectroscopy (ATR-IR) to characterize the surface structures of molecules of interest on gold films (*Chapter 2*). In *Chapter 3*, the electrical properties

of 1,4-phenylene diisocyanide on gold nanoparticle arrays were characterized, and the tunneling barrier through the linker molecule was found to be  $0.10 \pm 0.02$  eV [18]. In *Chapter 4*, infrared spectra of 1,4-phenylene diisocyanide adsorbed on gold films were measured and showed a single isocyanide stretching mode at low solution exposures. Higher PDI doses causes the isocyanide mode to split into two features, one of which is due to a free isocyanide, consistent with a vertically bonded species bound to the surface by one isocyanide group. This behavior rationalized the apparent disparity between the results obtained in ultrahigh vacuum and those obtained previously when dosing from solution [19]. *Chapter 5* explains the surface chemistry and electrical properties of 1,4-benzendithiol (1,4-BDT) and 1,3-benzendithiol (1,3-BDT) oligomers bridging between gold nanoparticles on mica. It was found that 1,4-benzendithiol adsorbs on Au(111) surfaces, with the two thiolates bound to a gold adatom to generate extended *zig-zag* chains, whereas 1,3-benzendithiol molecules were exclusively observed as monomeric species, which is the main reason why 1,4-benzendithiol has better electrical properties than 1,3-benzendithiol [20, 21]. According to the measured ATR-IR spectra, in both molecules, S-H bonds break and S-Au bonds form after adsorbing on gold films.

In order to study the influence of the lengths of diisocyanide and dithiol molecules, *Chapters 6* and *7* present electrical studies and surface structures of 4,4'-biphenyldiisocyanide (BPDI), 4,4'-terphenyldiisocyanide (TPDI), 4,4'-biphenyldithiol (BPDT) and 4,4'-terphenyldithiol (TPDT) on gold. As a result, in the case of dithiol aromatic molecules, the slopes of values derived from *I-V* measurements for BDT, BPDT and TPDT show that the height of the tunneling barrier increases with increasing the number of benzene rings in the linker backbone, which means that an increased extent of conjugation does not necessarily lead to higher conductivity. The biphenyl and terphenyl molecules have a twisted ring configuration which



appear to be observed for BPDT and TPDT. This distortion decreases the conjugation by reducing the orbital overlap between the aromatic rings. Therefore, the poly-phenyl dithiol molecules are not expected to be as conductive as benzene dithiol because of the higher tunneling barrier (*Chapter 6*).

The ATR infrared spectra of BPDI and TPDI adsorbed on a thin gold film showed the same behavior that was seen with 1,4-PDI on gold. At low solution exposures, a single isocyanide stretching mode was seen, while at higher solution concentrations the diisocyanide molecule orientation changes, and the free C≡N mode appears. Similar to dithiols, the electrical conduction of diisocyanides decreases when increasing the number of phenyl rings for two possible reasons; first, increasing the number of phenyl rings decreases the aromaticity because of the ring twisting configuration, which leads to increase the height of the tunneling barrier. Second, increase the number of phenyl rings in diisocyanide linkers increases the electron donation to the gold, that leaves a partial positive charge on the isocyanide molecule which leads to lowering the molecular orbital energies and moves the HOMO orbital away from the Fermi level (*Chapter 7*).

In *Chapter 8*, an asymmetric molecule with both isocyanide and S- terminated groups is explored, by studying the surface structure and electrical properties after dosing gold films with 4,4'-disulfanediyldibenzoisonitrile (DBN) from solution. As a result, DBN has ability to form oligomers between gold nanoparticles and contributes to tuning the gold Fermi level and increase the height of the electron tunneling barrier. The ATR-IR spectra provide information that is complementary to the electrical measurements, and allow the surface structure of DBN molecules on the gold-nanoparticle array to be determined.

Finally, in *Chapter 9*, back-gating behavior has been explored for three different devices. The field effect results showed a small increase in the conductivity with increasing the gate

potential of either sign. Electrical measurements were performed using 1,4-PDI-, 1,4-BDT- and 1,3-BDT-linked gold nanoparticles, and the maximum sheet resistance changes were ~1.5 to 2.3%. At a sample temperature of ~110K, the sheet-resistance changed by 4.5% under a negative bias.

## References

[1] Doris, B; Jeong, T. M.; Zhang, K. M.; Roy, R. A.; Dokumaci, O.; Ren, Z.; Jamin, F.; Shi, L.; Natzle, W.; Huang, H.; Mezzapelle, J.; Mocuta, A.; Womack, S.; Gribelyuk, M.; Jones, E. C.; Miller, R. J.; Wong, S. P.; Haensch, W.; *Digest. International pp.* **2002**, 267- 270.

[2] Likharev, K. K.; *Elsevier.* **2003**, 27-68.

[3] "Moore's Law to roll on for another decade" ([http:// news. cnet. com/ 2100-1001-984051. html](http://news.cnet.com/2100-1001-984051.html)). . Retrieved **2011-11-27**.

[4] Moore, Gordon E. (1965). "Cramming more components onto integrated circuits" ([http:// download. intel. com/ museum/ Moores\\_Law/ Articles-Press\\_Releases/ Gordon\\_Moore\\_1965\\_Article. pdf](http://download.intel.com/museum/Moores_Law/Articles-Press_Releases/Gordon_Moore_1965_Article.pdf)) (PDF). *Electronics Magazine.* p. 4. . Retrieved **2006-11-11**

[5] It's Moore's Law, But Another Had The Idea First ([http:// www. nytimes. com/ 2005/ 04/ 18/ technology/ 18moore. html](http://www.nytimes.com/2005/04/18/technology/18moore.html)) by John Markoff

[6] Law that has driven digital life: The Impact of Moore's Law ([http:// news. bbc. co. uk/ 2/ hi/ science/ nature/ 4449711. stm](http://news.bbc.co.uk/2/hi/science/nature/4449711.stm)) – A comprehensive BBC News article, 18 April **2005**

[7] Avarim, A.; Ratner, M.; *Chem. Phys. Lett.* **1974.** 29. 277-83.

[8] For a monograph, see for example: G. Roberts. *Langmuir–Blodgett Films.* Plenum Press, New York, **1990**.

[9] Metzger, R. M. *Biomolecular Electronics: Advances in Chemistry Series 240*, 81. R.R. Birge (Ed.), American Chemical Society, **1994**.

[10] Feyter, S.; De Schryver, F. C.; *Chem. Soc. Rev.*, **2003**, 32, 139–150

[11] Wold, D. J.; Haag, R.; Rampi, M. A.; Frisbie C. D.; *J. Phys. Chem. B*, **2002**, 106.

[12] Xiang, D.; Jeong, H.; Lee, T.; Mayer D.; *Adv. Mater.* **2013**, 25, 4845–4867

[13] Cohen, R.; Stokbro, K.; Martin, J.; Ratner, M. A.; *J. Phys. Chem. C* **2007**, 111, 14893-14902

[14] Pensa, E.; Cortés, E.; Corthey, G.; Carro, P.; Vericat, C.; Fonticelli, M. H. Benítez, G.; Rubert, A. A.; Salvarezza, R. C.; *Acc. Chem. Res.* **2012**, *45*, 1183.

[15] Ulman, A.; *Acc. Chem. Res.* **2001**, *34*, 855

[16] Murphy, K.; Tysoe W. T.; Bennet, D. W.; *Langmuir* **2004**, *20*, 1732-1738

[17] Hong, S.; Reifengerger, R.; *Superlattices and Microstructures*, **2000**, *28*, No. 4

[18] ] Kestell, J.; Abuflaha, R.; Boscoboinik, J.; Bai, Y.; Bennett, D.; Tysoe, W.T.; *Chem. Comm.* **2012**, *49*, 1422-4.

[19] Abuflaha, R.; Olson, D.; Bennett, D. W.; Tysoe, W. T.; *Surface Science.* **2016**, *649*, 56–59

[20] Kestell, J.; Abuflaha, R.; Garvey, M.; Tysoe, W. T.; *Phys. Chem. C* **2015**, *119*, 23042–23051

[21] Kestell, J. 2014. Ph.D. dissertation, University of Wisconsin-Milwaukee.

# Chapter 2

## Experimental Methods

### 2.1 High Vacuum System

In general, the essential requirements for performing thin-film experiments are a clean surface and a contaminant-free environment; consequently, all experiments were carried out under high-vacuum conditions where the pressure were maintained in the range of  $10^{-7}$ -  $10^{-8}$  Torr.

Low pressures help to reduce the density of contaminations and increase the mean free path of the gas molecules in the high-vacuum chamber. The mean free path is the average distance traveled by moving particles (such as atoms, molecules, photons) before colliding with another particle.

The mean free path  $\lambda$  can be calculated using the kinetic theory of gases from the following equation [1]

$$\lambda = \frac{k_B T}{\sqrt{2} \pi d^2 P} \quad (1)$$

where  $k_B$  is the Boltzmann constant,  $T$  is the temperature in Kelvin,  $d$  is the diameter of the molecule in meters, and  $P$  is the pressure in Pascal. At lower pressures, the mean free path increases and the collision rate reduces, which is a suitable condition for an experiment to be performed on a relatively clean surface.

## 2.2 High Vacuum (HV) Chambers

The high-vacuum chamber was made of corrosion-resistant, welded stainless-steel that allows the system to be baked up to  $\sim 150^{\circ}\text{C}$  for several days in order to remove the water layer and all other contaminations from the inner walls of the chamber shown in *Figure 2.1*.

Various tubes are welded to the chamber so that pumps, instrumentation, leak valves, and windows can be mounted to it. These tubes terminate in different types of flanges, such as Conflat flanges with knife-edged rims, allowing copper gaskets to be used to create a vacuum tight seal.

Alternatively, quick-release flanges, which are connected to each other by elastomer O-rings and are held together by a ring clamp, can be used for pump mounting.

It is important to ensure that the chamber and all the components inside the chamber are constructed from suitable materials with low vapor pressures. The inside of the chamber should be clean of high-vapor-pressure materials (such as finger-prints), and these can be removed using solvents, such as acetone.

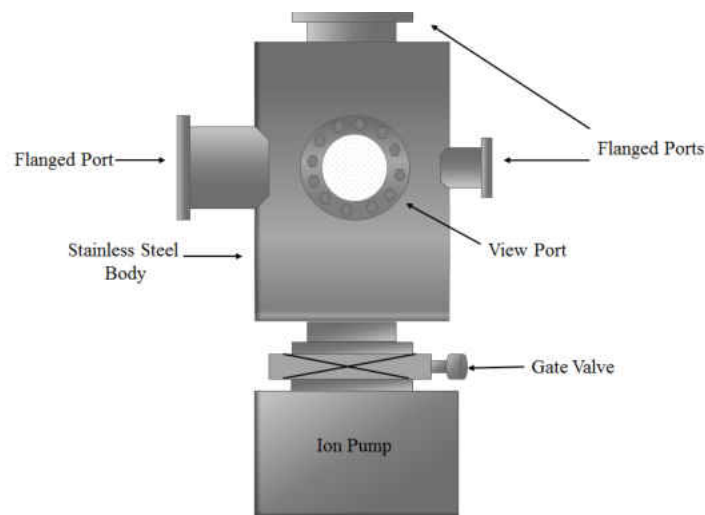


**Figure 2.1:** Diagram of a stainless steel high-vacuum chamber.

### 2.3 Conductivity Measurement Chamber

The conductivity measurement chamber is a standard UHV chamber, and is used for conductivity (current versus voltage) measurements of nanoparticle array samples (see section 2.6). It includes two high-vacuum feedthroughs to make electrical conduction to the sample. One feedthrough is installed on an X, Y, Z, theta manipulator that holds the copper plate which is designed to carry the sample under test (inside the vacuum) and connects it directly to a liquid-nitrogen filled reservoir (outside the vacuum) (*Figure 2.2*). This feedthrough has pins that are connected to two electrical wires terminated by two alligator clips which are carefully attached to the sample under test (*Figures 2.3*).

An additional feedthrough is attached to a chromel-alumel thermocouple that is spot-welded to the copper sample holder used to measure the sample temperature when it is cooled to liquid-nitrogen temperatures, or heated.

The current versus voltage (I/V) characteristics were measured by applying a voltage to the sample via a D/A converter controlled by a LabView program, and the resulting current is measured by means of a Keithley picoammeter placed in series with the circuit that converts the current to a voltage signal, which is sent back to the data acquisition card, so that an I/V curve is directly recorded and displayed on a PC screen (*Figure 2.4*). Once the sample is placed inside the chamber, the process of evacuation begins by pumping down, initially using rotary and turbomolecular pump and finally an ion pump, to a base pressure of  $\sim 10^{-8}$  Torr without baking the chamber to avoid sample damage.

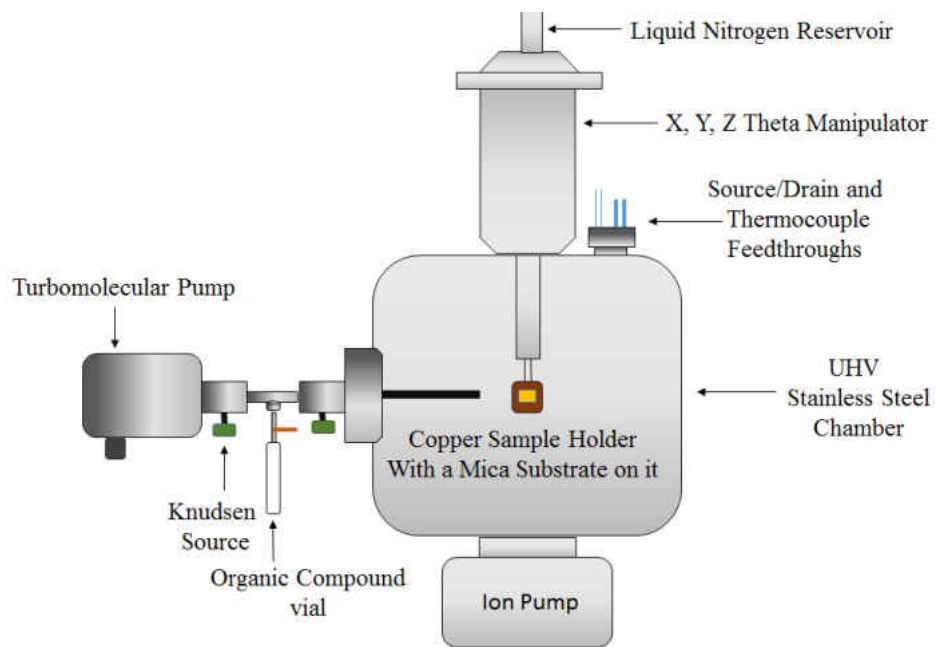


**Figure 2.2:** A typical combination for the electrical measurements chamber

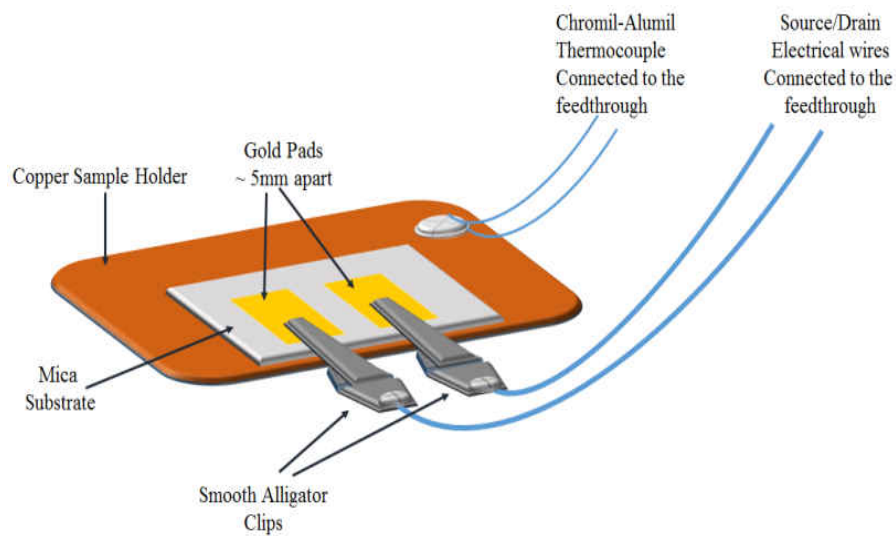


**Figure 2.3:** An illustration for mica substrate placed on the copper sample holder and connected to feedthroughs using fine alligator clips

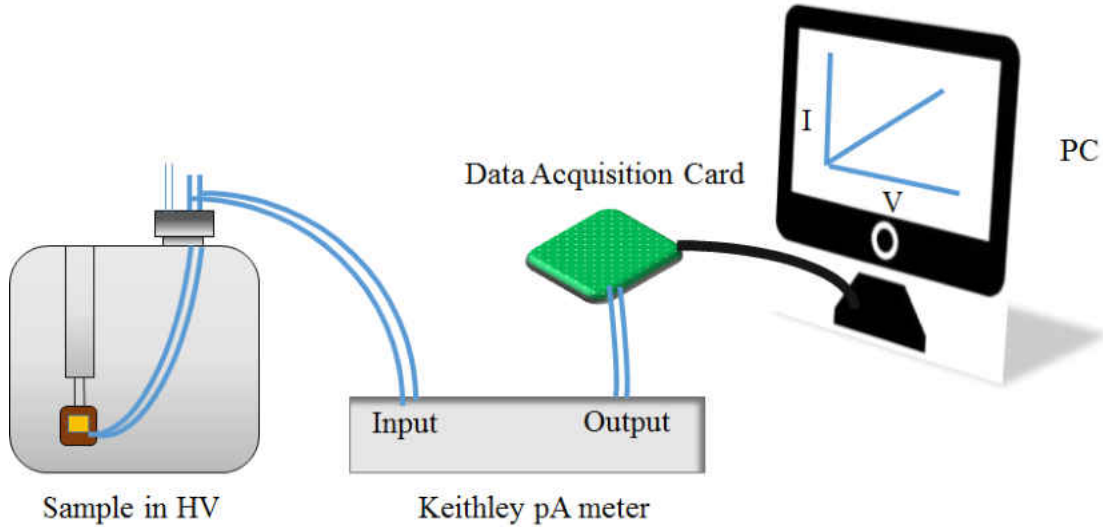


**Figure 2.4:** Block diagram of I/V measurement instrumentation

## 2.4 Vacuum Pumps

Achieving ultrahigh vacuum (UHV) where the pressure is  $\sim 5.0 \times 10^{-10}$  Torr or lower involves different stages of pumping and then baking the whole system to  $\sim 150^\circ$  C in order to remove adsorbed water from the inner walls. In case of conductivity measurement experiments, as mentioned above, baking the system while the sample is inside the chamber is not an option, and it was found to be adequate to pump the chamber for several hours until the pressure reached  $\sim 10^{-8}$  Torr.

### 2.4.1 Mechanical (Rotary Vane) Pump

A rotary vane pump is used for the first stage of pumping in the HV system, and operates between atmospheric pressure to  $\sim 10^{-3}$  Torr, and is used for rough pumping the vacuum chamber as well as a backing pump for oil diffusion and turbomolecular pumps. As is shown in *Figure 2.5*, the HV chamber is connected to the inlet of the pump, and the pressure in region I is equal to the chamber pressure. As the rotor turns, it traps a volume of gas at chamber pressure in region II, so that, as the rotor continues turning, and the gas molecules are forced to the outlet valve in region



III. The pressure increases until it exceeds atmospheric pressure, so that the gas is expelled through the outlet valve and through the oil into an exhaust vent [2].

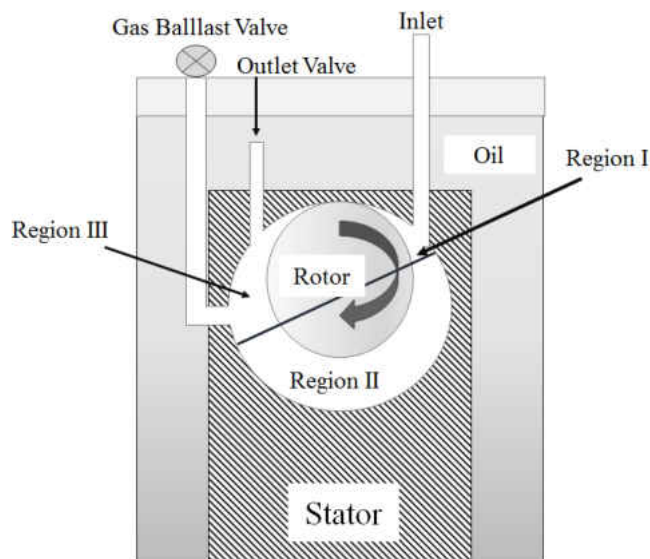


**Figure 2.5:** Rotary Mechanical Pump schematic

## 2.4.2 Turbomolecular Pumps

Turbomolecular pumps are often called “turbopumps” for simplicity, and they are used to reduce the pressure from  $\sim 10^{-3}$  Torr to  $\sim 10^{-7}$  Torr, and a mechanical pump is needed as backing pump. The turbopump consists of stack of rotors/slots with blades, so that when the blades are spinning (at  $\sim 20000$  rpm) they collide with the gas molecules in the pump and impart momentum to them, causing them to move to the next rotor. This series of blades drives the molecules towards the exhaust, where they are removed by the backing pump. Because of the rotor’s high speed, the pump’s temperature increases while running, so it is necessary to place a cooling fan on the pump while it is operating to maintain the pump temperature below  $30^{\circ}\text{C}$  (Figure 2.6).

Turbopumps are very clean, since they do not require oil to operate. They have the disadvantages that they can be noisy, are relatively expensive, and can introduce vibrations to the system [3].

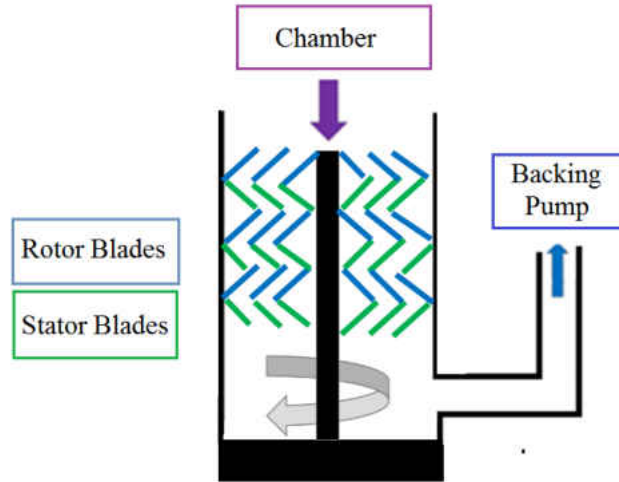


**Figure 2.6:** Turbomolecular pump schematic

### 2.4.3 Oil Diffusion Pumps

Oil diffusion pumps are used to further reduce the pressure from  $\sim 10^{-3}$  Torr to  $\sim 10^{-8}$  Torr, and require backing pumps in the same way as the turbomolecular pump. The pump consists of a pumping stack, and contains high-purity oil. As the oil is heated and evaporates, the stack confines it, so that the oil moves down the stack thereby colliding with gas molecules to drive them to the rotary pump, and then to the atmosphere. The oil vapor hits the sides of the pump that are cooled by water filled tubes, and the condensed oil returns back to the bottom to be reheated (*Figure 2.7*).

Since the pump relies on hot oil, there can be oil back-streaming to the HV chamber. To avoid back streaming of the oil, diffusion pumps use low-vapor-pressure, high-molecular-weight oils. To further eliminate oil from the chamber, the HV system is isolated from the pump using a liquid-nitrogen trap placed between the diffusion pump and the chamber [4].

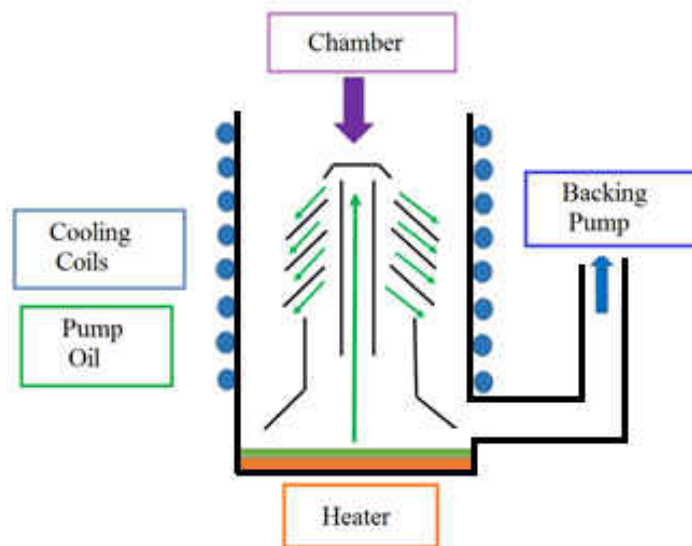


**Figure 2.7:** Oil diffusion pump schematic

#### 2.4.4 Ion Pumps (Sputter-ion pumps)

These pumps are capable to operate in the range  $\sim 10^{-5}$  to  $\sim 10^{-11}$  Torr. They form a closed system with the vacuum chamber, and they have no moving parts or additional valves and do not require the use of oil, and do not cause any vibrations inside the UHV system. There is no backing pump connected to the ion pump. However, the gate valve between the ion pump and the chamber cannot be opened until the HV chamber pressure drops below  $\sim 5.0 \times 10^{-5}$  Torr.

A sputter-ion pump consists of two electrodes, the anode and the cathode, where the anode is made of stainless steel, and the cathode plates are constructed from titanium. Titanium is inert when it is in its bulk form, but it is chemically reactive with most gases when it is deposited as a pure metallic film on a surface, and it serves as a gettering material on the anode tubes [5]. Strong magnets are placed outside the chamber, to create a high magnetic field inside it.

When the ion pump starts operating, free electrons are pulled towards the anode and get caught by the magnetic field that is created by the two magnets outside the chamber. The magnetic field forces the electrons to move and collide with incoming gas molecules, and the result of collisions is to create a positively charged ions that have sufficient kinetic energy to accelerate towards the cathode and be trapped in it. Ions will sputter titanium away from the cathode and form a gettering film on a neighboring surface and reacts to form stable chemical compounds with reactive gases, such as CO, CO<sub>2</sub>, O<sub>2</sub>, and N<sub>2</sub>. The anode assembly will be coated with these compounds (*Figure 2.8*). This process will keep sputtering small amount of cathode overtime, so that it will eventually develop craters from all the impacting ions and need to be replaced.

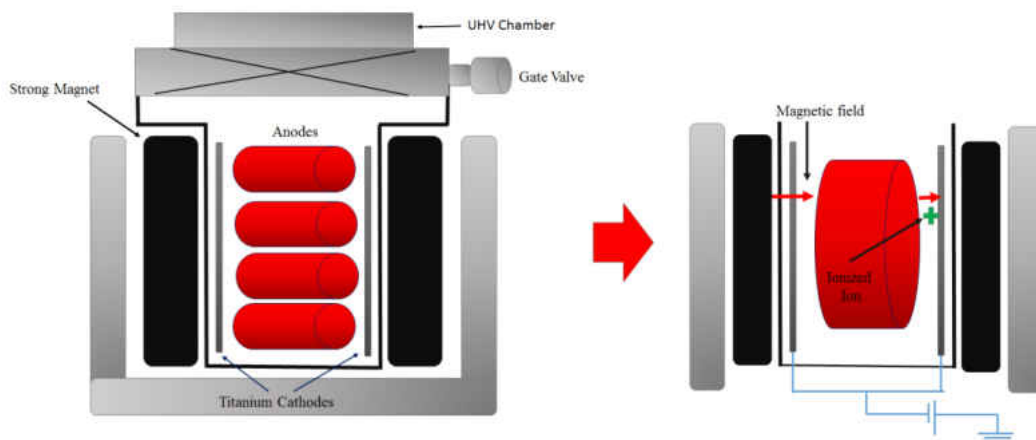


**Figure 2.8:** Ion pump schematic and operation

## 2.5 Metal Thermal Evaporator

In order to prepare samples for conductivity measurements, it was necessary to evaporate gold films to create nanoparticle arrays and gold electrodes. Gold thin film deposition, as a basic part of sample preparation for this work, was carried out in a Cooke Vacuum Products CVE 30 evaporator. This device is a thermal evaporator, and consists of a high-vacuum system which operates at  $\sim 10^{-8}$  Torr, and is used for vacuum deposition of metal thin films. As is shown in *Figure*

2.9, this device consists of a bell jar that is pumped using mechanical and diffusion pumps to a final pressure of  $\sim 10^{-8}$  Torr, in which the metal (gold) evaporation process is performed. For that purpose, the chamber contains a tungsten basket filament in which a piece of gold foil can be placed. An AC current is passed through the filament in order to heat it and the gold rapidly evaporates onto the sample to form a thin gold film.

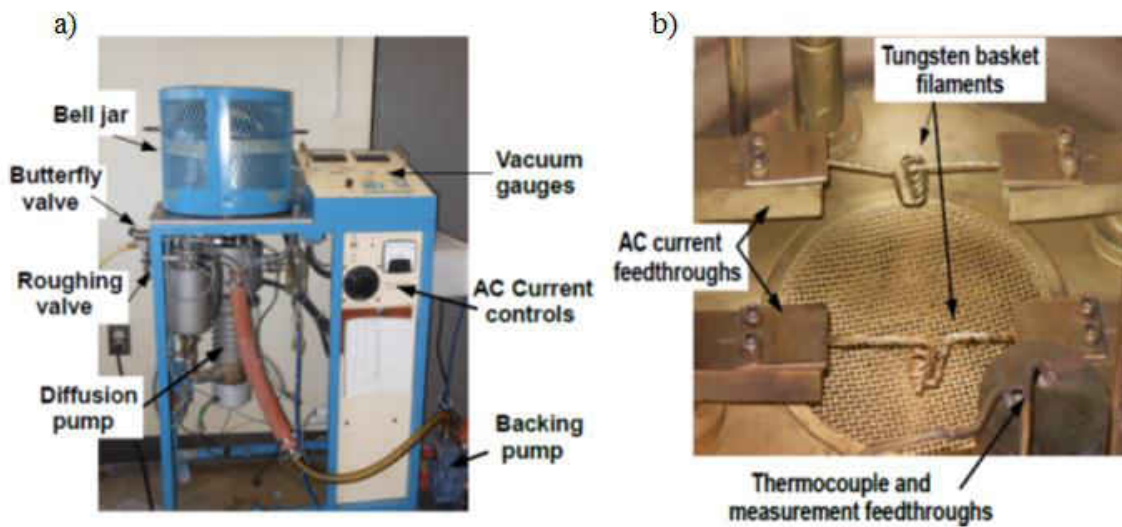


**Figure 2.9:** A) Cook Vacuum Products CVE 301 thermal evaporator. B) Inside the evaporator, tungsten basket filaments, pre-wetted with high purity gold [7].

This system is used to deposit both gold nanoparticle arrays and thicker gold electrodes.

The thickness of the gold electrode film deposited on mica substrate depends on the distance to the sample and the sample position. Inside the vacuum evaporator, the masked mica substrate is placed on a circle-shaped stand and faces the tungsten filament. The thickness of the gold film is calculated using the following equation:

$$t = \frac{m}{\rho 4\pi d^2} \quad (2)$$

where  $m$  is the gold mass,  $\rho$  is the gold density, and  $d$  is the distance between the tungsten filament and the sample. The temperature is sufficiently large to evaporate all the gold.

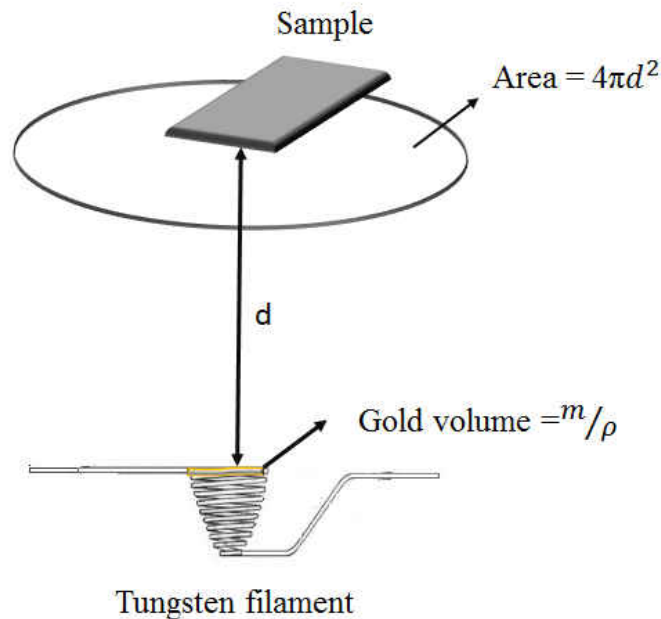


**Figure 2.10** Control the gold film thickness inside the evaporator

## 2.6 Sample Preparation

As shown in *Figure 2.3*, a  $1 \times 1 \text{ cm}^2$  cleaved mica substrate (highest grade, Ted Pella) was used as the sample support. Gold electrodes were fabricated by masking the central portion of the mica substrate and evaporating  $\sim 200 \text{ nm}$ -thick gold pads using the thermal evaporator with 99.999% purity gold (metal basis, Alfa Aesar) by passing a current of  $\sim 60 \text{ A}$  through the filament as described in *section 2.5*. After the gold pads were deposited, the sample was removed from the evaporator, the mask removed, and then the gold pads were attached to smooth alligator clips

inside the evaporator in order to monitor the resistance change while depositing gold nanoparticles on the mica substrate. After placing the sample into the chamber and pumping the evaporator to  $\sim 10^{-8}$  Torr, the deposition was carried out by passing a  $\sim 20$  A current through the tungsten filament. In this work, all the samples were prepared with different initial resistance values while continually monitoring the sample resistance. After reaching the desired initial resistance, the sample was left under vacuum for to age until the resistance stabilized. This typically requires a few hours, after which then the bell jar was opened to atmosphere, and the sample was removed.

The samples could be dosed with organic molecules after depositing gold nanoparticles, either by vapor deposition, or dosing from solution. Vapor deposition was carried out in the HV chamber using the Knudsen source, as shown in *Figure 2.2*. It is attached to one of HV chamber flanges, so that the end of the source faces the sample holder. The organic compound was placed in a glass vial and attached to the Knudsen source using a Swagelok connector, and the system was evacuated separately to outgas the sample while the valve between the Knudsen source and the HV chamber was closed. The gold nanoparticle-covered sample was attached to the copper sample holder in the HV chamber, and the chamber was pumped to  $\sim 10^{-8}$  Torr, and the valve between the Knudsen source and the chamber was opened to allow the sample to be dosed with the sublimed organic molecules. The resistance change across the gold pads was continually monitored and the dosing process was stopped after no further change in sample resistance was measured. Electrical conductivity measurements were then made as a function of sample temperature.

In case of dosing from solution, after the sample was again allowed to age and removed from the thermal evaporator, the sample was dosed by adding 50  $\mu\text{L}$  of the compound in a solution (generally benzene) with a certain concentration. The excess solution was removed by washing

using the same solvent, and the sample allowed to dry in air. It was mounted in the HV chamber to carry out the electrical measurements at different temperatures, as discussed above.

Sample cooling was achieved by pouring liquid nitrogen into the tube that is attached to the sample manipulator, and in a direct thermal contact with the copper sample holder. The sample temperature was monitored using a chromel-alumel thermocouple that is attached between the feedthrough and the sample holder. *I-V* measurements were carried out as the sample temperature was changing between room temperature and liquid nitrogen temperature.

## **2.7 Attenuated Total Reflection Infrared Spectroscopy (ATR-IR)**

### **2.7.1 ATR-IR Principle and Theory**

While traditional IR spectrometers have been used to analyze solids, liquids, and gases by means of transmitting the IR beam directly through the sample, ATR uses the reflection of the beam instead [8]. This technique measures the change that occurs in a totally internally reflected IR beam when it comes in contact with the sample (*Figure 2.11*). The IR beam is directed into an ATR crystal with a relatively higher refractive index, so that the beam reflects from the internal surface of the crystal creating an evanescent wave that extends 0.5-5  $\mu\text{m}$  into the sample held in contact with the crystal. The attenuated radiation is returned to the detector, then the system generates an IR spectrum [9].



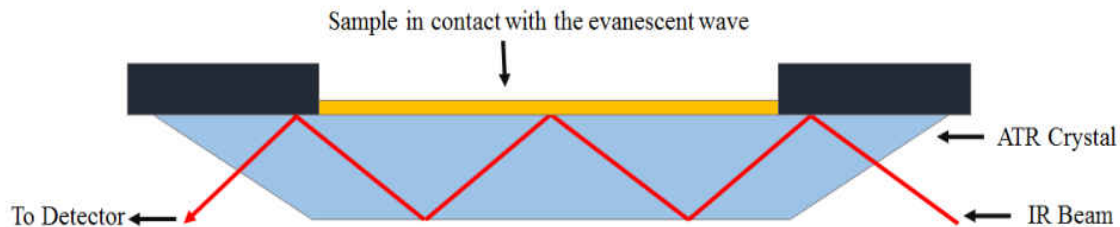


**Figure 2.11:** A multiple reflection across an ATR crystal

The condition which must exist to obtain total internal reflectance is that the angle of the incident radiation,  $\theta$ , must exceed the critical angle,  $\theta_c$ . The critical angle is a function of the refractive indices of the sample and ATR crystal and is defined as

$$\theta_c = \sin^{-1} \frac{n_2}{n_1} \quad (3)$$

where  $n_1$  is the refractive index of the ATR crystal, and  $n_2$  is the refractive index of the sample. The refractive indices of the crystal and the sample are important considerations in the ATR sampling technique, since  $n_1$  must be significantly greater than  $n_2$  (Figure 2.12), otherwise the beam will be transmitted rather than internally reflected in the crystal [10].

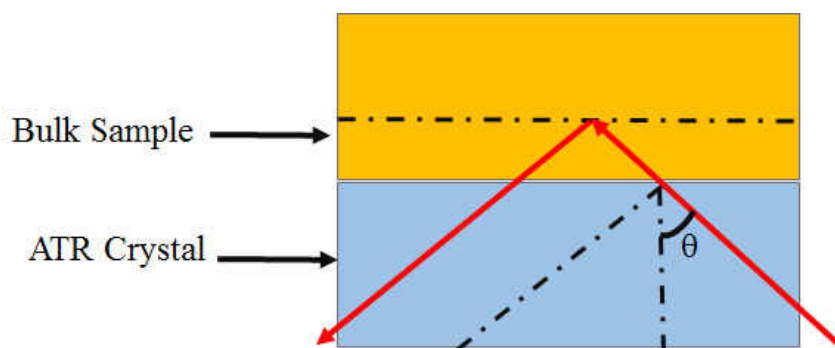


**Figure 2.12:** Illustration shows refractive index of crystal > sample

A further useful consideration for ATR analysis is the depth of penetration ( $d_p$ ) of the IR beam into the sample (*Figure 2.13*), which is defined by

$$d_p = \frac{\lambda}{2\pi(n_1^2 \sin^2 \theta - n_2^2)^{1/2}} \quad (4)$$

where  $\lambda$  is the wavelength of light and  $\theta$  is the angle of incidence of the IR beam [11]. As mentioned above, typical depth of penetration in the ATR ranges from 0.5-5 $\mu\text{m}$  depending upon the experimental conditions.

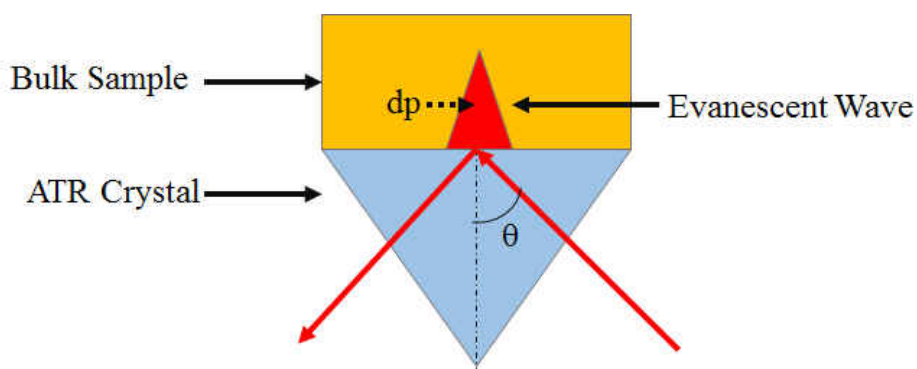


**Figure 2.13:** A single reflection ATR

In this work, the ATR-IR technique is used as a method for solution-phase surface studies to explore the structures of different organic molecules when coordinated to gold surfaces.

Zinc Selenide (ZnSe) was used as an ATR crystal ( $1 \times 8 \times 0.7 \text{ cm}^3$ ), which has refractive index of 2.4, while the typical values for organic substances range from 1.2 to 1.5, which means that a large majority of IR-active samples can be measured [12].

Infrared spectra were collected by evaporating a gold thin film on to the ZnSe crystal, in exactly the same way as depositing gold thin films on a mica substrate. A mica substrate with gold pads was used as a reference sample for resistance monitoring while depositing gold films on the ATR crystal. The gold film thickness is critical and it was selected to allow reasonable infrared transmission through the sample. After gold thin film deposition, different organic molecules with different concentrations were dosed onto the sample and then washed with benzene to rinse away the excess.

In order to clean the crystal, the gold film was removed by polishing the crystal using 1  $\mu\text{m}$  (MetaDi) diamond polishing compound. One drop of polishing compound was placed on the crystal and few drops of distilled water were added, using delicate-task Kimwipes, after which the crystal was polished manually and carefully until the gold film is completely removed. Then the polishing compound was washed away using distilled water and the crystal was left to dry before depositing a new gold film.

IR spectra were collected using Vertex infrared spectrometer operating at a resolution of  $4\text{cm}^{-1}$  by collecting 2000 scans using DTGS detector.

## References

- [1] Chapman and T.G. Cowling, The mathematical theory of non-uniform gases, 3rd. edition, Cambridge University Press, **1990**, ISBN 0-521-40844-X, p. 88
- [2] Hablanaian, M. H.; Vac, J.; *Sci. Technol.* **1994**, A 12, 897
- [3] Chapter 10: Turbomolecular Pumps. Vacuum Technology 60A & 60B. Las Positas College
- [4] Oil Diffusion Vacuum Pump Setup, Operation & Maintenance. Clinton Engineer Works. Optical Coating Facilities.
- [5] Ion Pumps – Operation and Applications. Duniway Stockroom Corp. Vacuum Equipment and Supplies.
- [6] Audi, M.; *Vacuum.* **1987**, 37. pp. 629
- [7] Kestell, J. **2014**. Ph.D. dissertation, University of Wisconsin-Milwaukee.
- [8] Introduction to Attenuated Total Internal Reflectance (ATR). Spectra-Tech
- [9] Hind, A. R.; Bhargava, S. K.; McKinnon, A.; *Advances in Colloid and Interface Science* **2001**, 93 (1-3), 91-114
- [10] Kazarian, S. G.; Chan, K. L. A. *Biochimica Et Biophysica Acta-Biomembranes* **2006**, 1758 (7), 858-867.
- [11] Mirabella, F. M.; Practical Spectroscopy Series; Internal reflection spectroscopy: Theory and applications, Marcel Dekker, Inc.; Marcel Dekker, Inc., **1993**, 17-52
- [12] Kassis, A. S. Ph.D. Dissertation. **2011**, Seton Hall University Department of Chemistry and Biochemistry

# Chapter 3

## Experimental and Theoretical Approaches

### 3.1 Introduction

The idea of “molecular electronics” was first proposed in 1970, when Aviram and Ratner postulated a very simple electronic device, a rectifier, based on the use of a single organic molecule [1]. Experimental approaches have been made to characterize transport properties by assembling monolayers on metal surfaces and use a tip electrode in scanning tunneling microscopy (STM) [2], and by conductive probe atomic force microscopy (CP-AFM) [3], or by attaching molecules in a mechanically controllable break junctions (MCBJ) to manipulate the electronic current at the atomic scale [4]. The transport in granular materials between metallic electrodes have been studied by using molecular linkers to control spacing between metallic nanoparticles [5].

In this chapter, the transport properties of linked gold nanoparticles with self-assembled 1,4-PDI linkers to form  $-(\text{Au-PDI})_n-$  oligomers is examined to illustrate the approach used in this work. PDI has been proposed as a prototypical molecular electronic component and a suitable candidate for electronic devices [5].

Scanning tunneling microscopy (STM) studies on Au (111) studies showed that PDI can form long, one-dimensional chains by extracting low-coordination gold atoms from surface defect sites, with a repeat distance of  $\sim 1.1$  nm [5] (*Figure 3.1*). If the distance between gold nanoparticles in granular films is greater than 1.1 nm, then  $-(\text{Au-PDI})_n-$  oligomers can be formed to fill the gap. This idea was explored by measuring the conductivity of PDI-dosed granular gold films.

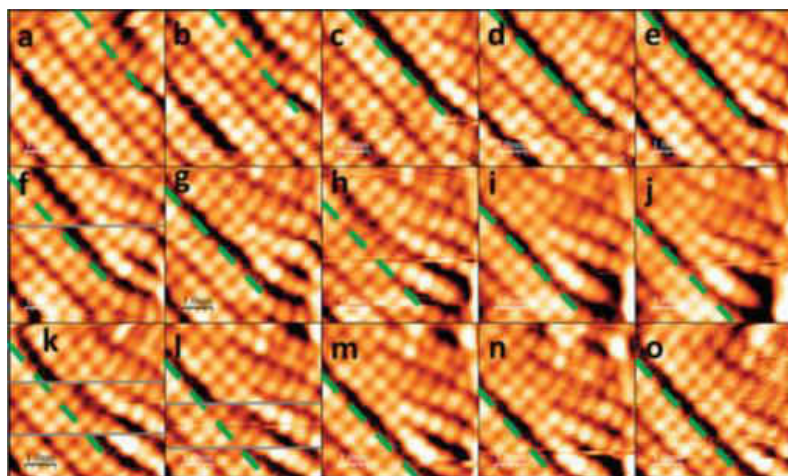


**Figure 3.1:** Time-dependent sequence of images of Au–PDI chains collected every 53 seconds scanning a  $5.0 \times 5.0 \text{ nm}^2$  region. A dotted line showing the chains has been included as a guide to the eye [5].

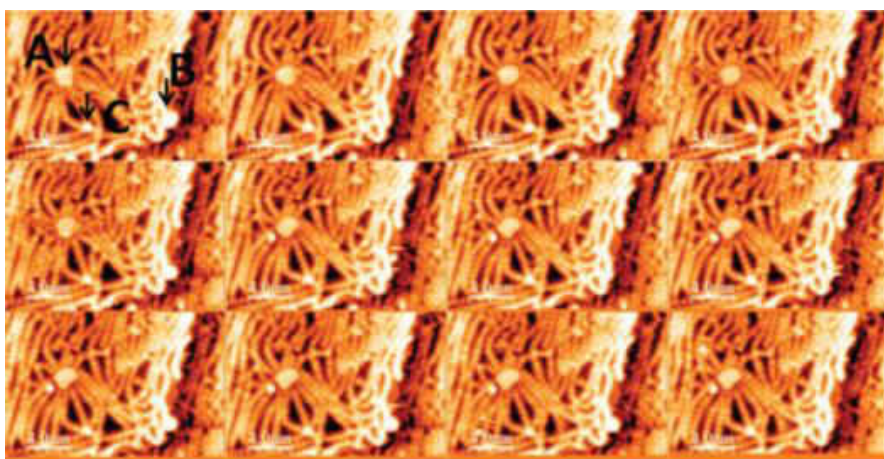


**Figure 3.2:** Sequence of images of Au–PDI oligomers linking between gold nanoparticles on a Au(111) surface where the location of the nanoparticles is indicated by A, B and C [5].

The ability of the mobile oligomers to bridge nanoparticles is illustrated by the series of STM images (*Figure 3.2*) of a Au(111) surface containing nanoparticles (Labelled A, B and C).

Clearly, the Au–PDI oligomers are capable of bridging between the gold nanoparticles (as depicted in the inset to *Figure 5*) and the images show the same chain mobility as seen in *Figure 1* [5].

The electrical properties of linker molecules are studied by depositing an array of gold nanoparticles on an insulating mica substrate. There are three distinct structural regimes in granular materials [7]. First, the metallic regime, where the metal concentration is high enough so that the grains can touch and form a continuous film. In this regime, the resistance increases with increasing temperature, which means that the temperature coefficient of resistivity (TCR) is positive, but still much smaller than in pure metals. Second, in the dielectric regime, where small isolated metal particles are formed, electrical transport is due to tunneling between the isolated particles. Finally, a transition regime occurs, in which the dielectric inclusions become interconnected to form a maze structure, and the electrical conductivity in this regime is due to percolation along the metallic maze and electron tunneling between isolated metal particles. In both dielectric and transition regimes the resistance decreases with increasing temperature, they both have a negative TCR.

In this work, the films were prepared by evaporating gold on a mica substrate to grow isolated gold nanoparticles with different average spacings by maintaining the gold thickness in the dielectric regime (*Figure 3.3*), above which a continuous metallic film can be formed. The sheet resistance decreases by increasing the number of gold nanoparticles (particle density) between the gold electrodes, which can be controlled by passing a set current through the evaporator in one evaporation step to some specific initial resistance, and then by allowing the sample to age until the sheet resistance stabilizes. As long as the gold nanoparticles are not touching, the charge will be transferred through tunneling or hopping mechanisms.

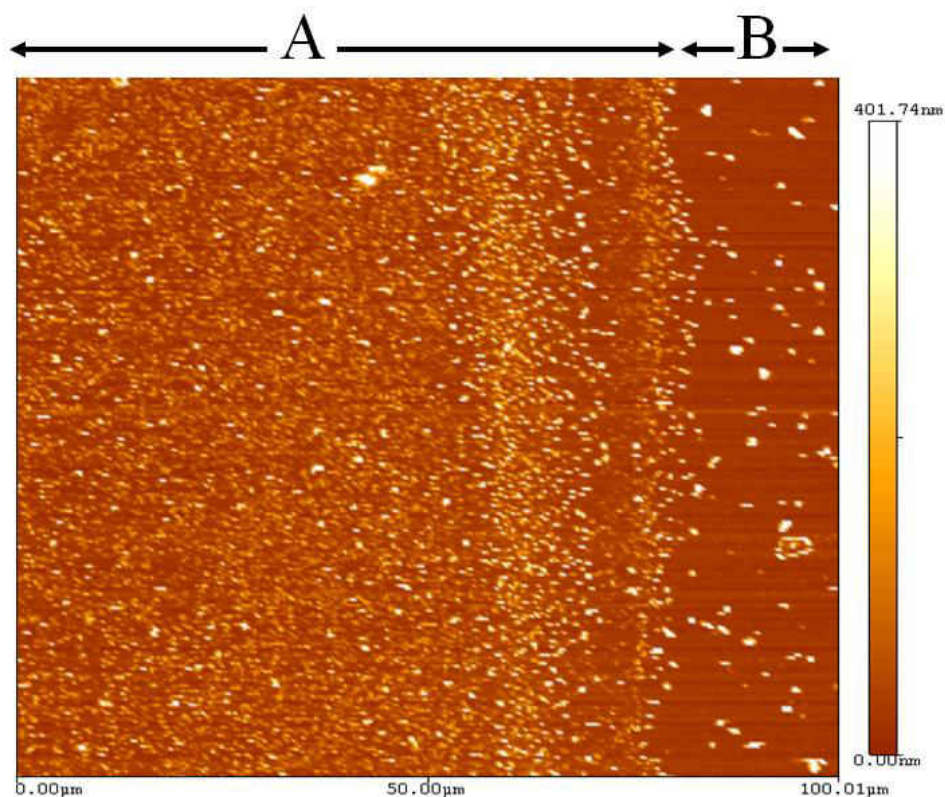


**Figure 3.3:** AFM image of a continuous film that represents a gold electrode (region A), and a nanoparticle array (dielectric regime as shown in region B) on mica substrate

### 3.2 Experimental

The experimental strategy has been discussed in detail in *Chapter 2*; briefly, a  $1\text{ cm} \times 1\text{ cm}$  mica substrate was used with  $\sim 200\text{-nm}$  thick gold electrodes, with a  $\sim 1\text{ mm}$  distance in between them. Deposition process takes place in a thermal evaporator. Gold nanoparticles were deposited to some initial resistance value. After deposition, the sample was left in the evaporator to age until the sheet resistance becomes stable. Gold nanoparticles were deposited until the conductivity between gold electrodes increased from zero to  $\sim 3.0\text{ nS}$ . As shown in *Figure 3.4*, the sample was left to age, during which, the gold nanoparticles aggregate to form larger clusters, which minimizes the number of electron tunneling junctions between the gold pads, causing the conductivity to



decrease as the number of gold nanoparticle decreases,. After  $\sim 2.5$  hours, the conductivity has decreased and became stable at  $\sim 0.6$  nS after the aging process had stopped.

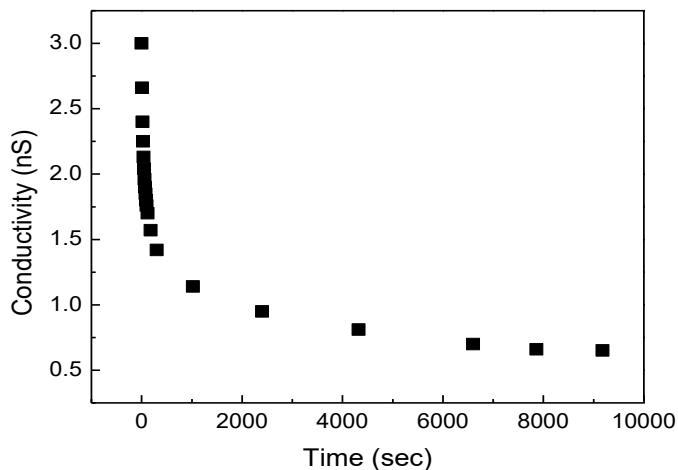


**Figure 3.4:** Gold nanoparticles aging process. In this sample, the initial conductivity was 3.0 nS, the sample aged to  $\sim 0.6$  nS.

The sample was moved from the thermal evaporator and placed inside the HV chamber, and the chamber was pumped to  $10^{-8}$  Torr, after which the 1,4-PDI was deposited in situ from the gas phase. Conductivity started to gradually increase from 0.6 nS, so that after  $\sim 2$  hours, the sample was saturated and the measured conductivity was equal to  $\sim 30$  nS (*Figure 3.5*).

Electrical measurements were carried out as described in *Chapter 2*, where resistance values were measured as a function of temperature by cooling the sample holder to liquid nitrogen temperature. Similar experiments were performed for samples with different initial resistance values.

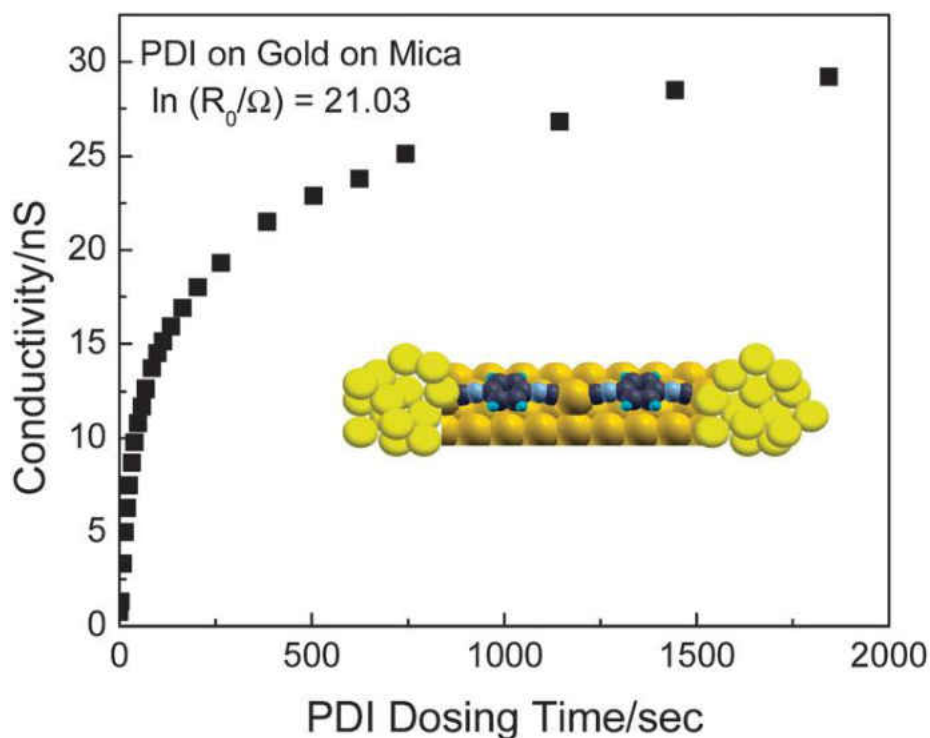


**Figure 3.5:** Typical curve shows the increase in conductivity across a granular film as a function of 1,4-PDI dosing time.  $R_0$  is the sheet resistance of the clean gold film before dosing. The inset shows a schematic depiction of the oligomer-linked nanoparticles

### 3.3 Results

The initial resistance ( $R_0$ ) values for all measured films in this study ranged between  $\sim 30$  M $\Omega$  to 990 M $\Omega$  where, in all samples, the  $R_0$  values dropped dramatically after dosing with 1,4-PDI from gas phase, proposed to be due to the formation of  $-(\text{Au-PDI})_n-$  oligomers between the gold nanoparticles [5]. Another possible reason is that the gold nanoparticles film changes from dielectric regime to transition regime because of the morphology of gold nanoparticles. AFM measurements of the particle morphology before and after dosing with PDI [5].

$I/V$  curves were measured as a function of change in temperature for all of the samples. They show Ohmic behavior up to a bias voltages of  $\pm 4$  V. Plots of  $\ln(R)$  versus  $T^{-1/2}$  have shown

a good linearity (*Figure 3.6*). The excellent linear fits of the  $\ln(R)$  versus  $T^{-1/2}$  plots in this system confirms the model proposed by Abeles and Sheng [6]. However, Arrhenius plots of  $\ln(R)$  versus  $T^{-1}$  were constructed and showed pronounced nonlinearity, Arrhenius behavior was predicted by Nuegbauer and Webb by the theory of activated tunneling in granular materials [7].

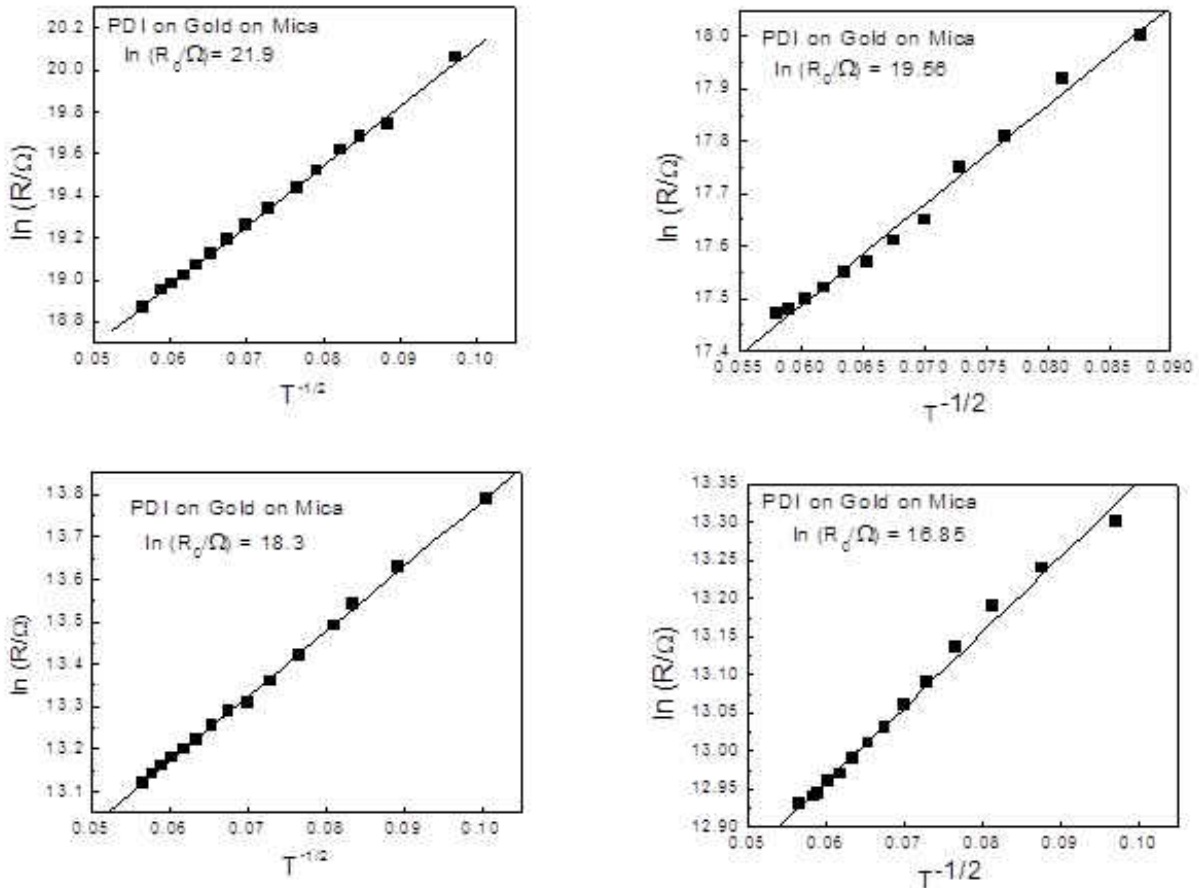


**Figure 3.6:** Typical plots of  $\ln(R/\Omega)$  versus  $T^{-1/2}$ , where the temperature is measured in degrees in Kelvin for various films with a range of initial films resistances. The value of the initials resistance values of the films,  $R_o$ , are indicated on each of the plots.

The slopes of the plots of  $\ln(R)$  versus  $T^{-1/2}$  were obtained for films spanning a wide range of initial (undosed) resistances,  $R_o$ . The slopes of these plots ( $\alpha$ ) was found to vary linearly with  $\ln(R_o)$  (*Figure 3.7*). The slope of this plot was found to be  $3.7 \pm 0.2$  with an intercept of  $-52 \pm 3$ .

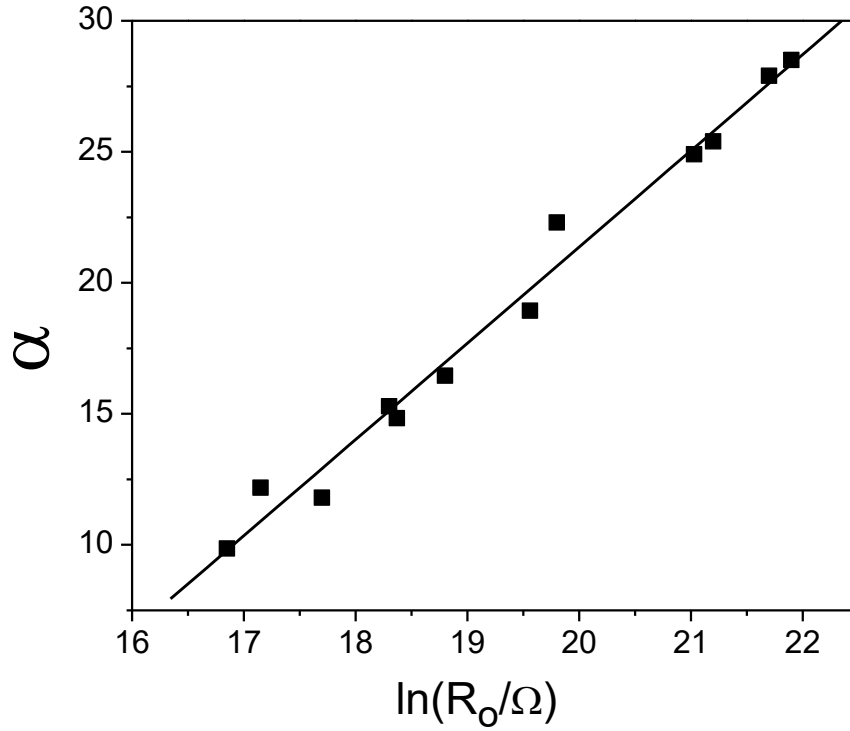


**Figure 3.7:** Plot of  $\alpha$  values versus  $\ln(R_0)$  for the 12 films studied in this chapter. The linear is in agreement with the theory of activated tunneling in granular materials put forth by Abeles and Sheng [6].

### 3.4 Discussion

Electrical conduction measurements have been performed in the granular regime, where all studied films have a negative temperature coefficient of resistivity (TCR), and showed a decrease in resistance with increasing temperature; the conduction mechanism is not the same as in metallic films. The linear  $\ln(R)$  versus  $T^{-1/2}$  variation is predicted by Abeles theory for thermally assisted tunneling through granular materials. This model provides an explicit dependence of the conductivity on the size and separation of the nanoparticles, which has been experimentally

verified elsewhere [5]. This theory, which provides the basis for the analyses of the conductive behavior of linked gold nanoparticles, is described in the next section.

### 3.4.1 Theoretical Aspects (Abeles Theory of Conduction in Granular Materials)

All samples show a linear relationship between  $\ln(R)$  and  $T^{-1/2}$  that can be attributed to the form of the density of states near the Fermi level [6] which is predicted by the Abeles model for thermally assisted tunneling through granular materials [6] which also provides an explicit dependence of conductivity on the size and separation of the nanoparticles.

The theory of Abeles and Shang analyzes the conductivity through an array on nanoparticles as a function of applied voltage. In particular, since there are a large number of nanoparticles contained between the electrodes, the voltage drop between adjacent electrodes is small and the current versus voltage characteristics are analyzed in the low-voltage limit.

The model assumes that electron transport between adjacent nanoparticles is controlled by two effects. The first effect arises because of the small size, and therefore capacitance of adjacent nanoparticles which requires a significant threshold energy for an electron to be transported from one nanoparticle to an adjacent one, the so-called Coulomb charging energy,  $E_C$ . The second effect is the direct tunneling of the electron from one nanoparticle to the next and is analyzed using the WKB approximation.

The energy required to charge a capacitor with capacitance  $C$  with one electron of charge  $e$  is given by  $\frac{e^2}{2C}$  so that the Coulomb charging energy is given by:

$$E_C = \frac{e^2}{2C} \quad (5)$$

If  $d$  is the size of a particle, which are separated by a distance  $s$ , the capacitance between particles will depend on  $d$  and  $s$ , where the details depend on the shape and arrangements of the particles. Abeles analyses this by using a model for the capacitance of a particle diameter  $d$ , where the effect of the surrounding nanoparticles is modeled by an annulus around the central nanoparticle separate by a distance  $s$ . The energy density of an electric field  $\underline{E}$  is given by  $\frac{1}{2}\epsilon\epsilon_0|\underline{E}|^2$ , where  $\epsilon_0$  is the permittivity of free space, and  $\epsilon$  is the relative permittivity of the material between the nanoparticles. For the simple model for the capacitor given above, this yields:

$$E_C = \frac{1}{2}\epsilon\epsilon_0 \int_{d/2}^{d/2+s} \left(\frac{e}{4\pi\epsilon\epsilon_0 r}\right)^2 4\pi r^2 dr \quad (6)$$

where  $e$  is the electronic charge. This can be straightforwardly integrated to give:

$$E_C = \frac{e^2}{4\pi\epsilon\epsilon_0 d} \left(\frac{s/d}{\frac{1}{2} + (s/d)}\right) \quad (7)$$

Thus, the Coulomb charging energy can be written as:

$$E_C = \frac{e^2}{4\pi\epsilon\epsilon_0 d} F\left(\frac{s}{d}\right) \quad (8)$$

It is also assumed that the tunneling probability depends on the particle separation,  $s$ , and the height of the barrier,  $\phi$ . Writing  $\chi = \left[\frac{2m\phi}{\hbar^2}\right]^{\frac{1}{2}}$  where  $m$  is the mass of the electron,  $\hbar$  is Plancks constant divided by  $2\pi$ , the tunneling probability is  $\sim \exp(-2\chi s)$ .

The number of charge carriers depends on the temperature  $T$ , and is proportional to  $\exp\left(-\frac{E_C}{2k_B T}\right)$ , where  $k_B$  is the Boltzmann constant. Thus, the total low-field conductivity  $\sigma_L$  is proportional to the product of the tunneling mobility multiplied by the temperature-dependent number of charge carriers integrated over all possible percolation paths through the sample:

$$\sigma_L \propto \int_0^\infty \beta(s) \exp\left(-2\chi s - \frac{E_C}{2k_B T}\right) ds \quad (9)$$

where  $\beta(s)$  is the density of percolation paths associated with  $s$ . Writing  $C = \chi s E_C$  gives:

$$\sigma_L \propto \int_0^\infty \beta(s) \exp\left(-2\chi s - \frac{C}{2\chi s k_B T}\right) ds \quad (10)$$

In this case,  $C$  depends on  $s$ . However, Abeles *et al* argue that the product  $sE_C$  is approximately constant. It is assumed that the particles on the surface are produced from some total volume  $V$  of material (in this work, gold) and is sufficiently small that it forms  $n$  isolated particles per unit area of average diameter  $d$  separated by an average distance  $s$ . If the nanoparticles that are formed have an approximately equal thickness  $t$ , then  $V \sim n t d^2$ . If the particles are separated by an average distance  $s$  and have a diameter  $d$ , then the average area occupied by each particle  $\sim (s + d)^2$ . The number of particle per unit area is then the reciprocal of this value so that  $V \sim \frac{t}{(1 + \frac{s}{d})^2}$ . This indicates that the ratio  $s/d$  is approximately constant for a given loading of metal on the surface. This simple analysis assumes that the heights of the nanoparticles is approximately constant and this has been disputed. Nevertheless, it provides a convenient model for our purposes since it yields values of the tunneling barriers for the molecular linkers and the experimental results are in good agreement with the theory. Thus from Eqn. 7:

$$sE_C = \frac{e^2}{4\pi\epsilon\epsilon_0} \left( \frac{(s/d)^2}{\frac{1}{2} + \frac{s}{d}} \right) \quad (11)$$

and, from the above arguments, is a constant since it depends only on  $s/d$ , which is argued to be a constant for a given metal loading. Note that, even if the value of  $t$  does vary,  $C$  will only be a relatively weakly varying function of  $s/d$ . Consequently, the value of  $C$  is given by:

$$C = \frac{\chi e^2}{4\pi\epsilon\epsilon_0} \left( \frac{(s/d)^2}{\frac{1}{2} + \frac{s}{d}} \right) \quad (12)$$

The next step is to calculate the of  $s$ ,  $s_m$  which gives the maximum conductivity. Eqn. 6 contains two factors,  $\beta(s)$  and  $\exp(f(s))$ , where  $f(s) = -2\chi s - \frac{c}{2\chi s k_B T}$ , and is a peaked function of  $s$ . From percolation theory,  $\beta(s)$  is a relatively slowly varying function of  $s$  [8], so that the effect of changing  $s$  is dominated by variations in  $f(s)$ , which is a strongly peaked function. To obtain the value of  $s_m$ ,  $f(s)$  is differentiated, assuming that  $C$  is constant, and put to zero to give:

$s_m = \sqrt{\frac{c}{k_B} \frac{1}{2\chi}}$ . Expanding the integral  $f(s)$  around  $s_m$  gives:

$$f(s) = f(s_m) + \frac{1}{2} f''(s_m)(s - s_m)^2 + \dots = -2\sqrt{\frac{c}{2k_B T}} - \sqrt{\frac{k_B T}{c}} (2\chi s - 2\chi s_m)^2 + \dots \quad (13)$$

Substituting into Eqn. 10 gives:

$$\sigma_L \propto \beta(s_m) \left[ \exp\left(-2\sqrt{\frac{c}{k_B T}}\right) \int_0^\infty \exp\left\{-\sqrt{\frac{k_B T}{c}} \left(2\chi s - \sqrt{\frac{c}{k_B T}}\right)^2\right\} ds \right] \quad (14)$$

where the value of  $s_m$  is the spacing at the maximum of the conductivity and  $\beta(s_m)$  is the density of percolation paths, taken to be approximately constant, and  $s_m = \left(\sqrt{\frac{c}{k_B T}}\right)/2\chi$ . Putting  $\sqrt{\frac{c}{k_B T}} = \alpha$  yields:

$$\sigma_L \propto \beta(s_m) [\exp(-2\alpha)] \int_0^\infty \exp\left\{-\frac{1}{\alpha} (2\chi s - \alpha)^2\right\} ds \quad (15)$$



The integral becomes  $\int_0^\infty \exp\left\{-\left(\frac{2\chi s}{\sqrt{\alpha}} - \sqrt{\alpha}\right)^2\right\} ds$ . Put  $p = \frac{2\chi s}{\sqrt{\alpha}} - \sqrt{\alpha}$  and the integral becomes

$\frac{\sqrt{\alpha}}{2\chi} \int_{-\sqrt{\alpha}}^\infty e^{-p^2} dp$ . Assuming (following Abeles) that  $\alpha$  is large, the integral becomes  $\frac{\sqrt{\alpha}}{\chi} \int_0^\infty e^{-p^2} dp$

and gives:

$$\sigma_L \propto \beta(s_m) [\exp(-2\alpha)]^{\frac{\sqrt{\pi\alpha}}{2\chi}} \quad (16)$$

Assuming that the temperature dependences of  $\beta(s_m)$  and  $\frac{\sqrt{\pi\alpha}}{2\chi}$  are relatively small gives:

$$\sigma_L = \sigma_0 \exp\left(-2\sqrt{\frac{c}{2k_B T}}\right) \quad (17)$$

We now apply the model to either a clean (gold) nanoparticle film, or a film proposed to be linked by oligomer chains. Since, in the majority of experiments, the resistance rather than the conductivity was measured, Eqn. 17 is rewritten as:

$$R = R_0 \exp\left[+2\sqrt{\frac{c}{k_B T}}\right] \quad (18)$$

Note that this temperature dependence is found for the films dosed by organic linkers in this work, suggesting that the above approximations are reasonable. Thus, the resistance,  $R_C$ , of the clean gold film (prior to dosing) provides a convenient parameter for describing its properties and, from equation (18) is:

$$\ln R_C = \ln R_C^0 + 2\sqrt{\frac{c_c}{300k}} \quad (19)$$

where  $T = 300$  K, the temperature at which the resistance was measured. Taking  $\varepsilon = 1$  for a vacuum and substituting for  $C$  yields:

$$\ln R_C = \ln R_C^0 + \sqrt{\frac{e^2 f(s,d)}{k}} \times \sqrt{\frac{4}{75}} \times \sqrt{\chi_C} \quad (20)$$

In the case of films dosed with organic linkers, the slopes of plots of  $\ln(R)$  versus  $1/\sqrt{T}$  are found to vary linearly with  $\ln(R_C)$ . Since from above,  $\alpha = 2\sqrt{\frac{C_F}{k}}$ , where  $C_F = \frac{4\chi_F e^2 f(s,d)}{\varepsilon_F}$ ,  $\alpha$  is given by:

$$\alpha = \sqrt{\frac{16\chi_F e^2 f(s,d)}{\varepsilon_F}} \quad (21)$$

Since  $f(s,d)$  is identical for clean and organic-covered films, rearranging equation (21) and substituting into equation (20) gives a relationship between  $\alpha$  (the slope of  $\ln(R)$  versus  $1/\sqrt{T}$ ), and the initial resistance of the clean film ( $R_C$ ) as:

$$\alpha = 17.32 \sqrt{\frac{\chi_F}{\varepsilon_F \chi_C}} \times \ln R_C - 17.32 \sqrt{\frac{\chi_F}{\varepsilon_F \chi_C}} \times \ln R_C^0 \quad (22)$$

This plot is found to be linear for the majority of the organic linker molecules and can be used to estimate the height of the tunneling barrier from  $\chi_F$ .

The slope in *Figure 7* ( $\alpha$  versus  $\ln(R_C)$ ) is  $3.7 \pm 0.2$ , which indicates that  $\frac{\chi_F}{\varepsilon_F \chi_C} = 0.045 \pm 0.005$ . PDI has a dielectric constant ( $\varepsilon_F$ ) value of 3.5, and since  $X = \left(\frac{2m\phi}{\hbar^2}\right)^{1/2}$  where  $\phi$  is the height of the tunneling barrier, then  $\frac{\phi_F}{\phi_C} = 0.025 \pm 0.005$ , where  $\phi_F$  and  $\phi_C$  are the barrier heights for the PDI dosed and the clean gold films respectively. Work function of clean gold ( $\phi_C$ ) is  $\sim 5.5$  eV, which makes  $\phi_F$  equals to 0.14 eV. However, PDI adsorbed on Au lowers the work function ( $\phi_C$ ) to 4.08 eV, which modulates the barrier height ( $\phi_F$ ) to  $1.1 \pm 0.02$  eV (*Figure 3.8*).

According to STM measurements of several phenyl-based isocyanides and diisocyanides, it was found that the value of  $(\phi_F)$  is equal to  $0.38 \pm 0.1$  eV for 1,4-PDI bridging gold [9]. Spectroscopic studies of Au–PDI oligomers on Au (111) show that the HOMO of the oligomer lies  $\sim 0.88$  eV below the Fermi level, with a LUMO  $\sim 3.32$  eV above it, consistent with a HOMO tunneling barrier [10]. More recent experiments found a barrier height of  $0.19 \pm 0.02$  eV [11], where the difference from previous results was ascribed to different numbers of PDI molecules in the contact. Break-junction measurements suggested a thermionic barrier height of  $0.22$  eV for PDI between gold electrodes [12].

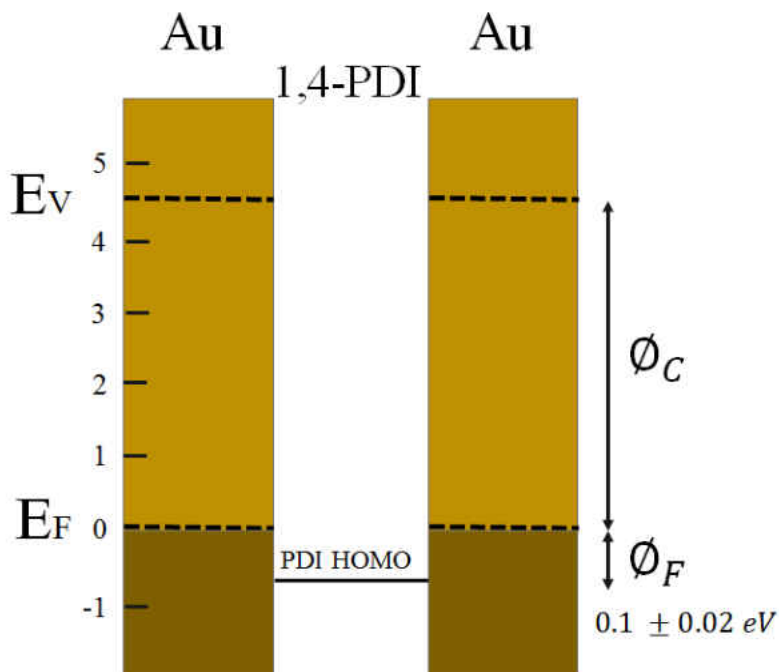


**Figure 3.8:** Energy level diagram for gold nanoparticles linked by 1,4-PDI oligomers, where  $\phi_C$  corresponds to the work function of the 1,4-PDI-covered gold nanoparticles (4.08 eV) and  $\phi_F$  is the tunneling barrier through the linker molecule measured to be  $0.10 \pm 0.02$  eV.

### 3.5 Conclusion

PDI on Au(111) self-assembles with gold to form oligomers that are sufficiently mobile to bridge between gold nanoparticles. The conductivity of gold nanoparticles on mica increases substantially when exposed to PDI and requires both the presence of the nanoparticles and two isocyanide groups. The temperature dependence of the conductivity is in accord with the particles being electrically linked with a tunneling barrier height of  $\sim 0.1$  eV.

### References

- [1] Avarim, A.; Ratner, M.; *Chem. Phys. Lett.* **1974**, *29*, 277-83
- [2] Feyter, S.; De Schryver, F. C.; *Chem. Soc. Rev.*, **2003**, *32*, 139–150
- [3] Wold, D. J.; Haag, R.; Rampi, M. A.; Frisbie C. D.; *J. Phys. Chem. B*, **2002**, *106*.
- [4] Xiang, D.; Jeong, H.; Lee, T.; Mayer D.; *Adv. Mater.* **2013**, *25*, 4845–4867
- [5] Kestell, J.; Abuflaha, R.; Boscoboinik, J.; Bai, Y.; Bennett, D.; Tysoc, W.T.; *Chem. Comm.* **2012**, *49*, 1422-4.
- [6] Abeles, B.; Sheng, P.; Coutts, M. D.; Arie, Y. *Advances in Physics* **1975**, *24*, 407.
- [7] Neugebauer, C. A.; Webb, M. B.; *Journal of Applied Physics*. **1962**, *33*, 74.
- [8] Thomsen C.; *Physical Review*. **2002**, *E 65*, 065104.
- [9] Kim, B.; Beebe, J. M.; Jun, Y.; Zhu, X.y.; Frisbie, C. D.; Am, J.; *Chem. Soc.*, **2006**, *128*, 4970–4971.
- [10] Zhou, J.; Acharya, D.; Camillone, N.; Sutter, P.; White, M. G.; *J. Phys. Chem. C*, **2011**, *115*, 21151–21160.
- [11] Lörtscher, E.; Cho, C. J.; Mayor, M.; Tschudy, M.; Rettner, C.; Riel, H.; *Chem Phys Chem*, **2011**, *12*, 1677–1682
- [12] Chen, J.; Wang, W.; Klemic, J.; Reed, M. A.; Axelrod, B. W.; Kaschak, D. M.; Rawlett, A. M.; Price, D. W.; Dirk, S. M.; Tour, J. M.; Grubisha, D. S.; Bennett, D. W.; *Ann. N. Y.; Acad. Sci.*, **2002**, *960*, 69–99.

## Chapter 4

# Surface Chemistry and Structures of 1,4-phenylene Diisocyanide on Gold Films from Solution

### 4.1 Introduction

Adsorbing 1,4-phenylene diisocyanide (PDI) on Au(111) single crystal surfaces in ultrahigh vacuum at room temperature results in the spontaneous formation of one-dimensional chains parallel to the surface which are observed when the surface is imaged using scanning tunneling microscopy (STM). The one-dimensional assemblies have been assigned to oligomeric chains comprising alternating gold and PDI units [1-4] that form by extracting gold atoms from low-coordination sites on the gold substrate, where the structure was confirmed by comparing the simulated images of oligomer structures calculated using density function theory (DFT) calculations and from the reflection absorption infrared spectra of oligomer-covered surfaces [4]. Adatom structures formed on coinage metals are relatively common [5-8]. Density functional theory (DFT) calculations of the oligomer formation pathway reveal that a vertical Au-PDI adatom complex provides the propagating monomer that inserts to the isocyanide terminus of a tilted PDI molecule bound to a surface defect such as a step edge [9].

In contrast to these observations, the results of previous work to explore the chemistry of PDI adsorbed onto planar gold surfaces and powdered gold from solution proposed structures in which the PDI adsorbed *via* one of the isocyanide groups, leaving a pendant, isolated isocyanide group [10-15]. Compelling evidence for this structure comes from the detection of a vibrational stretching mode due to an unbound isocyanide. There appears therefore to be a discrepancy

between the results obtained under ultrahigh vacuum (UHV) conditions on Au(111) and those found when dosing from solution. However, it has recently been shown that adsorbing carbon monoxide on a PDI-covered Au(111) surface covered by  $-(\text{Au-PDI})-$  oligomer chains results in the decoordination of one of the isocyanide groups in the oligomer chain to form a vertical PDI species adsorbed to a gold adatom, that exhibits two vibrational modes due to free and bound isocyanide groups [16]. Similar isocyanide decoordination, induced by PDI adsorption rather than by CO, as in the above example, would rationalize the apparent discrepancy between the results for PDI on gold films and nanoparticles and the work on Au(111) single crystals in UHV. This would involve the initial formation of  $-(\text{Au-PDI})-$  oligomer chains oriented parallel to that surface that then decoordinate at higher PDI exposures to form vertically oriented species.

This issue is addressed here first by measuring the infrared spectra of PDI on gold films dosed from solution as a function of solution dose using attenuated total internal reflection infrared spectroscopy (ATR-IR) to determine the structure and orientation of adsorbed PDI. The molecular orientation can be determined using the surface selection rules [17-19], combined with comparison of the experimental vibrational frequencies with those from previous work.

In addition, it has been shown that gold-containing PDI oligomers can bridge between gold nanoparticles on a mica substrate (*Chapter 3*) [20]. Since the oligomers maintain their  $\pi$  conjugation, this provides a conductive pathway between the gold nanoparticles, thereby causing the conductivity to increase. This observation is confirmed since the experimentally measured variation in conductivity with temperature and nanoparticle spacing is in accord with the Abeles model for conductivity through an array of nanoparticles [21, 22]. It was also found that PDI decoordination to form vertical PDI molecules induced by CO co-adsorption resulted in an decrease in conductivity due to an interruption of the conductive pathway [16]. Similar

decoordination induced by additional solution exposure to PDI should therefore also result in conductivity decrease. Accordingly, the conductivity of a gold-nanoparticle array grown on an insulating mica support was measured after exposing it to increasing PDI doses from solutions. It is anticipated that if the PDI restructures at the higher exposures available by solution dosing to induce adsorption in an  $\eta^1$ -configuration *via* one isocyanide group, the conductive path should also be interrupted, thereby lowering the conductivity to providing an additional *in situ* probe of any change in molecular configuration. The results of these experiments are reported here, where it is found that, at low PDI doses from solution, the infrared spectra show a single isocyanide peak at a similar frequency to that found for PDI on Au(111), due to Au–PDI oligomer chains, where the conductivity of a PDI-dosed nanoparticle array increases over the same range of PDI doses. At higher doses, the free isocyanide mode appears in the infrared spectrum, accompanied by a conductivity decrease, in accord with PDI decoordination to form an  $\eta^1$  species.

## 4.2 Experimental Methods

The conductivity of PDI on nanoparticle-covered mica was measured as described in detail elsewhere [20]. 10  $\mu$ l aliquots of serially diluted PDI solutions (with a 5 mM initial solution concentration) in benzene were deposited on a gold nanoparticle array, the sample was then rinsed with benzene to remove any remaining weakly bound PDI and allowed to dry in air.

Electrical measurements were made at base pressure of  $\sim 2 \times 10^{-8}$  Torr. The temperature was monitored by means of a chromel-alumel thermocouple attached to the sample, and the I/V characteristics were measured by applying a voltage *via* a D/A converter and the resulting current measured by means of a picoammeter that was monitored by an A/D converter to yield I/V curves directly.

Infrared spectra of PDI gold films were also collected by evaporating gold onto the zinc selenide ATR plate for 2000 scans using a DTGS detector. The gold film thickness was selected to allow reasonable infrared transmission through the sample to be obtained and spectra were collected after dosing with 200  $\mu\text{l}$  aliquots of a 0.5 mM PDI solution in benzene. The sample was allowed to dry in air and then rinsed with benzene to remove any residual, weakly bound PDI.

### 4.3 Results

*Figure 4.1* shows a series of ATR-IR spectra of a gold film dosed sequentially with solutions of PDI in benzene as a function of PDI solution dose, where the PDI doses are indicated adjacent to the corresponding spectrum. Initial PDI exposure gives rise to a single, relatively broad feature centered at  $\sim 2166\text{ cm}^{-1}$  in the  $\text{C}\equiv\text{N}$  stretching region. The peak frequency remains constant at this value up to a dose of  $\sim 40\text{ nmoles/cm}^2$ . The detection of a single isocyanide stretching mode is consistent with the presence of a single type of isocyanide group expected for the formation of a  $-(\text{Au-PDI})-$  oligomer chain. When formed on Au(111), the oligomers exhibit a single  $\text{C}\equiv\text{N}$  mode at  $\sim 2154\text{ cm}^{-1}$  at low coverage, shifting to lower frequencies ( $\sim 2139\text{ cm}^{-1}$ ) at higher exposures, likely due to coupling between the isocyanide groups as the chains grow, so that the isocyanide mode frequencies found by solution dosing are within the range expected for oligomer chains [4, 9, 23].

After dosing with  $50\text{ nmoles/cm}^2$  of PDI solution, the  $\sim 2166\text{ cm}^{-1}$  mode shifts to a slightly lower frequency, with a sharper peak appearing at  $\sim 2120\text{ cm}^{-1}$ . Adding further PDI shifts the broad feature slightly to  $\sim 2158\text{ cm}^{-1}$  and is accompanied by the growth in intensity of the  $\sim 2120\text{ cm}^{-1}$  peak. These spectra are in reasonable agreement with the results from previous work on 1,4-PDI on gold films [10] that suggested that the molecules adsorb perpendicularly to the surface with the



free isocyanide group exhibiting a vibrational frequency of  $2120\text{ cm}^{-1}$ . Note that weakly adsorbed molecule PDI would also give rise to a free isocyanide mode. However, this possibility is excluded since the dosed surfaces were rinsed with benzene after exposure to the PDI solution to remove any excess PDI. Other work [11] showed similar frequencies of  $2121$  (free) and  $2172$  (surface-bound)  $\text{cm}^{-1}$  for solution-dosed gold. Sum-frequency generation (SFG) results [24] provided corresponding vibrational frequencies of  $2122$  and  $2195\text{ cm}^{-1}$  for the free and bound isocyanide groups, respectively. An average of the values of the vibrational frequencies of isocyanide SAM's on gold from the literature (summarized in reference [24]) yields a value of  $2123 \pm 1\text{ cm}^{-1}$  for a free isocyanide group and  $2181 \pm 4\text{ cm}^{-1}$  for a surface-bound group. The spectrum shown in *Figure 4.1* after dosing more than  $50\text{ nmoles/cm}^2$  of PDI is thus indicative of a vertical PDI species since it clearly exhibits a free isocyanide mode at  $\sim 2120\text{ cm}^{-1}$ . Large PDI exposures on a Au(111) surface in vacuo also show the appearance of a shoulder at  $\sim 2123\text{ cm}^{-1}$  assigned to a free isocyanide group with an additional, more intense peak at  $\sim 2136\text{ cm}^{-1}$  [4], similar to that seen in *Figure 4.1*, but with much lower intensity.

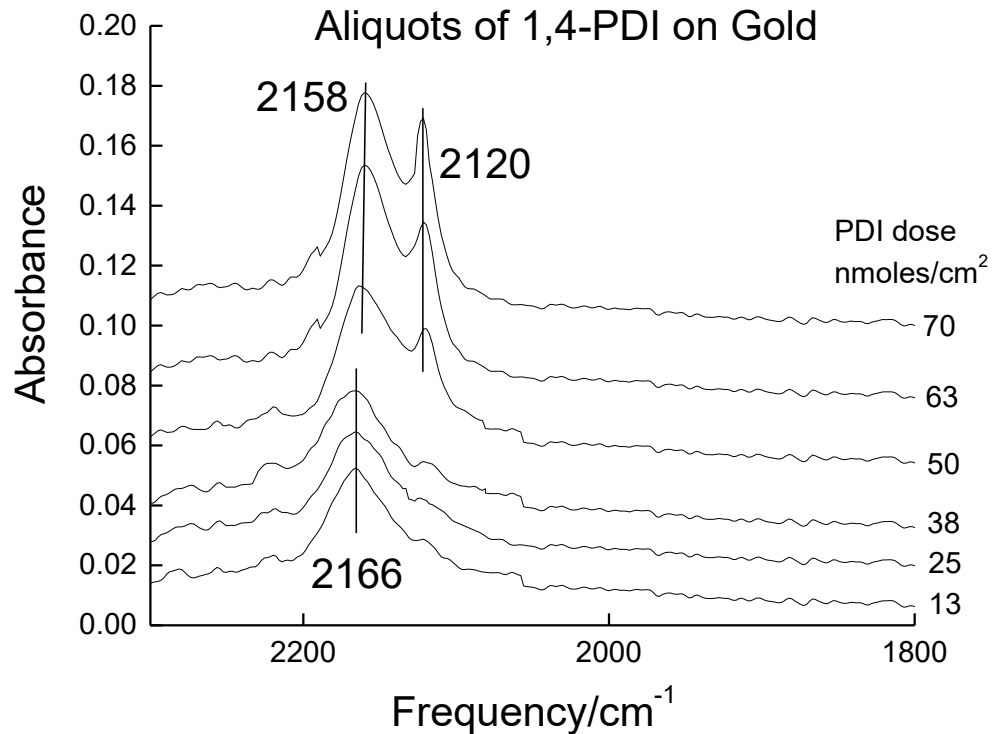


**Figure 4.1:** A series of ATR infrared spectra of PDI adsorbed on a thin gold film using aliquots of 200  $\mu\text{l}$  of solution of 0.5 mM PDI. The resulting PDI doses, in  $\text{nmole}/\text{cm}^2$ , are indicated adjacent to the corresponding spectrum.

The conductive properties of gold nanoparticles deposited onto a mica substrate exposed to 50  $\mu\text{l}$  aliquots of serially diluted PDI solutions in benzene are summarized in *Figure 4.2*, which plots the conductivity versus the PDI dose in  $\text{nanomoles}/\text{cm}^2$ . The clean sample, prior to PDI dosing, had a conductivity of  $\sim 0.5$  nS. The conductivity of the sample increases monotonically with PDI dose from solution to reach a maximum value of  $18 \pm 2$  nS. The experiment was repeated several times, giving consistent results yielding a dose at which the conductivity reached its maximum value of  $45 \pm 5$   $\text{nmoles}/\text{cm}^2$ . This maximum conductivity is in reasonable agreement with that found by gas-phase dosing (of  $\sim 23$  nS) [20]. However, in the case of gas-phase dosing,

the conductivity saturates over the range of PDI doses accessible in high vacuum while, when dosing from solution at higher doses, the conductivity decreases, initially quite rapidly, to a value of  $\sim 8$  nS and then more slowly as the PDI dose exceeds  $\sim 60$  nanomoles.

#### 4.4 Discussion

The above infrared results suggest that PDI on a gold film initially adsorbs with the PDI plane parallel to the surface with symmetrically equivalent isocyanide vibrational modes, consistent with the formation of  $-(\text{Au-PDI})-$  oligomer chains, but then changes orientation at higher exposures to exhibit a free isocyanide frequency, consistent with a decoordinates species. The gas-phase vibrational spectrum of 1,4-PDI ( $D_{2h}$  symmetry) has been assigned [25] and the most intense infrared vibrations are at 850 ( $B_{1g}$  symmetry, aryl ring mode), 1505 ( $B_{1u}$  aryl ring mode), 2127 ( $A_g$ , symmetric  $\text{N}\equiv\text{C}$  stretch) and 2132  $\text{cm}^{-1}$  ( $B_{1u}$ , asymmetric  $\text{N}\equiv\text{C}$  stretch). This is consistent with the 2166  $\text{cm}^{-1}$  mode being due to an isocyanide vibration and the presence of a single mode is consistent with a  $-(\text{Au-PDI})-$  oligomer chain. However, the vibrational frequency found on the gold thin films is slightly higher than for PDI on Au(111) where peaks appear between  $\sim 2154$  and 2139  $\text{cm}^{-1}$ . This shift on Au(111) was ascribed to changes in chain length and may imply that the chains on the gold film are relatively short.

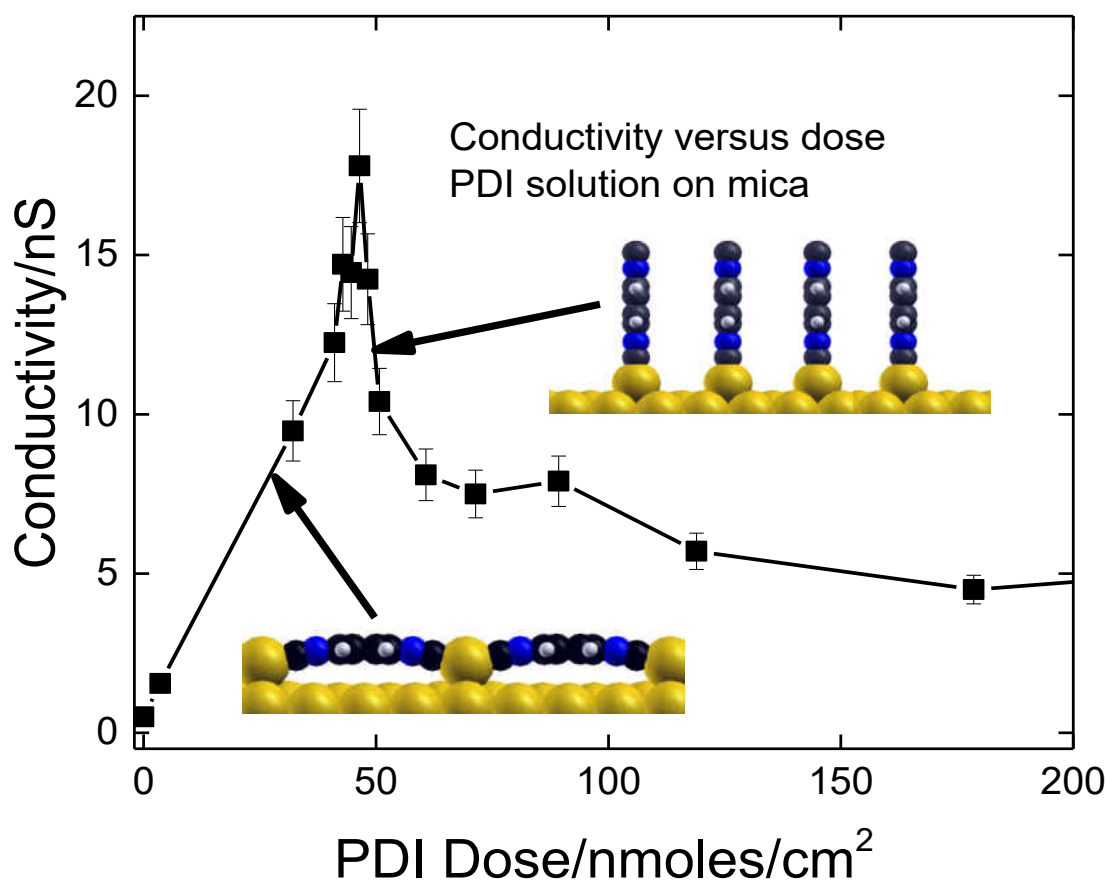


**Figure 4.2:** Plot of the conductivity of gold nanoparticles deposited onto a mica substrate, with an initial conductivity of 0.5 nS (nanoSiemens) after exposure to 50  $\mu$ l of serially diluted solutions of PDI in benzene as a function of the solution dose in nmole/cm<sup>2</sup>.

The vibrational frequencies after a larger doses of PDI solution (at 2158 and 2120  $\text{cm}^{-1}$ ) are in excellent agreement with the results of previous studies where the PDI was proposed to have a vertical geometry [10, 11, 26], although there is some variability in the frequency of the bound isocyanide mode (from 2172 to 2195  $\text{cm}^{-1}$ ). The bound isocyanide mode for PDI on Au(111) is at

$\sim 2136\text{ cm}^{-1}$  [4], suggesting that the nature of the substrate (oxidic *versus* Au(111)) can influence the frequency of the Au–C $\equiv$ N mode.

Measurements of conductivity as a function of PDI dose from solution are shown in *Figure 4.2*. Analogous experiments in which the gold nanoparticles were exposed to PDI *in vacuo* showed that the conductivity increased from  $\sim 0.5\text{ nS}$  for the nanoparticle array prior to dosing, to a maximum value of  $\sim 23\text{ nS}$  when the sample was saturated with PDI [20]. This effect was ascribed to the linking of the nanoparticles by conductive Au–PDI oligomers. A similar initial increase in conductivity is found experimentally for solution dose up to  $45 \pm 5\text{ nanomoles/cm}^2$  (*Figure 4.2*) leading to a maximum conductivity of  $\sim 18\text{ nS}$ , in reasonable agreement with the results by gas-phase dosing ( $\sim 23\text{ nS}$ ). Thus the initial increase in conductivity is ascribed to the formation of conductive Au–PDI oligomers, depicted in *Figure 4.2*, that self-assemble to interconnect gold nanoparticles on mica. However, at higher PDI doses, the conductivity decreases substantially indicating that the conductive pathway is being disrupted, although there is some residual conductivity in the neighborhood of  $\sim 8\text{ nS}$ . This result is clearly consistent with the idea that the initial Au–PDI oligomer chains change structure to form a vertical Au–PDI species at higher PDI concentrations, where the structure is depicted in *Figure 4.2*, as suggested by the infrared data (*Figure 4.1*). In particular, the dose at which the conductivity starts to decrease (*Figure 4.2*), coincides with the appearance of the free isocyanide mode (at  $\sim 2120\text{ cm}^{-1}$  with a PDI dose of  $\sim 50\text{ nmoles/cm}^2$ ) in the infrared spectra (*Figure 4.2*). A similar decrease in conductivity was found for a gold-covered mica surface dosed with PDI and then exposed to CO, in that case, the decrease in conductivity was ascribed to the disruption of the conductive pathways between the gold nanoparticles by the formation of similar vertical Au–PDI species that were assigned using infrared spectroscopy and imaged by scanning tunneling microscopy (STM) [16]. The decoordination

caused by CO co-adsorption was rationalized by a kinetic process in which small fluctuations in the isocyanide coordination in the one-dimensional chains allowed CO to rapidly diffuse into the interchain region to prevent the oligomer chains from reforming. We refer to such a process as a “foot-in the door” mechanism.

While the dosing times and solvents were different for earlier infrared experiments for PDI on gold films and nanoparticles from the ones used in this work, it is instructive to compare the conditions used to collect the data shown in *Figures 4.1* and *4.2* with those used to obtain the previous results. Work on PDI on gold films dosed with 15 mM solutions of PDI in DMSO were exposed overnight [11], clearly corresponding to the region in which additional PDI adsorbs on the surface (*Figure 4.1*). Other work on gold films [10] used a 1 mM PDI solution in methylene chloride or THF for an exposure time of 12 hours likely also to result in additional PDI adsorption. Interestingly, experiments on powdered gold [12] that used PDI concentrations up to 1 mM in methanol in which the suspension was shaken for a relatively short time of ~30 s, also showed clear evidence for a free isocyanide group (at  $2121\text{ cm}^{-1}$ ).

#### **4.5 Conclusions**

The infrared spectrum of 1,4-phenylene diisocyanide adsorbed on gold films displays a single isocyanide stretching mode at low solution exposures, consistent with the presence of  $-(\text{Au}-\text{PDI})-$  oligomer chains identified previously on Au(111) surface where the PDI was dosed in ultrahigh vacuum. Higher PDI doses causes the isocyanide mode to split into two features, one of which is due to a free isocyanide, consistent with a vertically bonded species bound to the surface by one isocyanide group. This behavior rationalized the apparent disparity between the results obtained in ultrahigh vacuum and those obtained previously when dosing from solution. The conversion of the flat-lying PDI in the oligomer chains to the vertical species is analogous to the

PDI decoordination induced by CO adsorption, which was proposed to occur by a kinetic “foot-in-the-door” mechanism in which small fluctuations in the isocyanide coordination in the one-dimensional chains allows molecules to rapidly diffuse into the interchain region to prevent the oligomer chains from reforming. Since linking gold nanoparticles on a mica substrate by  $-(\text{Au}-\text{PDI})-$  oligomer chains provides a conductive pathway between the chains, disrupting the linkages at higher PDI doses should cause a conductivity decrease. This is found to occur, thereby providing corroborative evidence of PDI reorientation at higher coverages.

## References

- [1] Boscoboinik, J.; Kestell, J.; Garvey, M.; Weinert, M.; Tysoe, W.; *Top. Catal.*, **2012**, 54, 20-25.
- [2] Boscoboinik, J. A.; Calaza, F. C.; Habeeb, Z.; Bennett, D. W.; Stacchiola, D.J.; Purino, M.A.; Tysoe, W. T.; *Physical Chemistry Chemical Physics*, **2010**, 12, 11624-11629.
- [3] Zhou, J.; Acharya, D.; Camillone, N.; Sutter, P.; White, M. G.; *The Journal of Physical Chemistry C*, **2011**, 115, 21151-21160.
- [4] Kestell, J.; Abuflaha, R.; Boscoboinik, J. A.; Garvey, M.; Bennett, D. W.; Tysoe, W. T.; *The Journal of Physical Chemistry Letters*, **2014**, 5, 3577-3581.
- [5] Maksymovych, P.; Sorescu, D. C.; Yates, J. T.; *Phys. Rev. Lett.*, **2006**, 97.
- [6] Maksymovych, P.; Yates, J. T.; *Journal of the American Chemical Society*, **2008**, 130, 7518-7519.
- [7] Lennartz, M.C.; Atodiresei, N.; Müller-Meskamp, L.; Karthäuser, S.; Waser, R.; Blügel, S.; *Langmuir*, **2008**, 25, 856-864.
- [8] Voznyy, O.; Dubowski, J. J.; Yates, J.T.; Maksymovych, P.; *Journal of the American Chemical Society*, **2009**, 131, 12989-12993.
- [9] Garvey, M.; Kestell, J.; Abuflaha, R.; Bennett, D. W.; Henkelman, G.; Tysoe, W. T.; *The Journal of Physical Chemistry C*, **2014**, 118, 20899-20907.
- [10] Henderson, J.I.; Feng, S.; Bein, T.; Kubiak, C. P.; *Langmuir*, **2000**, 16, 183-6187.
- [11] Swanson, S. A.; McClain, R.; Lovejoy, K. S.; Alamdari, N.B.; Hamilton, J.S.; Scott, J.C.; *Langmuir*, 21 (2005) 5034-5039.



- [12] Robertson, M.J.; Angelici, R.J.; *Langmuir*, **1994**, 10, 1488-1492.
- [13] Shih, K.-C.; Angelici, R.J.; *Langmuir*, **1995**, 11, 2539-2546.
- [14] Angelici, R.J.; Lazar, M.; *Inorg. Chem.*, 2008, 47, 9155-9165.
- [15] Angelici, R.J.; *J. Organomet. Chem.*, **2008**, 693, 847-856.
- [16] Kestell, J.; Boscoboinik, J.A.; Cheng, L.; Garvey, M.; Bennett, D. W.; Tysoe, W. T.; *The Journal of Physical Chemistry C*, **2015**.
- [17] Greenler, R. G.; *The Journal of Chemical Physics*, **1966**, 44, 310-315.
- [18] Greenler, R.G.; *The Journal of Chemical Physics*, **1969**, 50, 1963-1968.
- [19] Kottke, M.L.; Greenler, R.G.; Tompkins, H.G.; *Surf. Sci.*, **1972**, 32, 231-243.
- [20] Kestell, J.; Abuflaha, R.; Boscoboinik, J.A.; Bai, Y.; Bennett, D. W.; Tysoe, W. T.; *Chem Commun*, 2013, 49, 1422-1424.
- [21] Abeles, B.; Sheng, P.; Coutts, M. D.; Arie, Y.; *Advances in Physics*, **1975**, 24, 407-461.
- [22] Sheng, P.; Abeles, B.; Arie, Y.; *Phys. Rev. Lett.*, **1973**, 31, 44-47.
- [23] Kestell, J.; Abuflaha, R.; Garvey, M.; Tysoe, W. T.; *The Journal of Physical Chemistry C*, 2015, 119, 23042-23051.
- [24] Ito, M.; Noguchi, H.; Ikeda, K.; Uosaki, K.; *Phys. Chem. Chem. Phys.*, 2010, 12, 3156-3163.
- [25] Han, H. S.; Han, S. W.; Joo, S. W.; Kim, K.; *Langmuir*, 1999, 15, 6868-6874.
- [26] Ikeda, K.; Fujimoto, N.; Uehara, H.; Uosaki, K.; *Chem. Phys. Lett.*, 2008, 460, 205-208.

## Chapter 5

# Surface Chemistry and Electrical Properties of 1,4-Benzendithiol and 1,3-Benzendithiol Oligomers Bridging Between Gold Nanoparticles On Mica

### 5.1 Introduction

Organic compounds have the ability to serve as molecular components for electronic devices, the most widely studied and well-characterized systems include alkanethiols, dialkyl sulfides, and dialkyl disulfides on gold and silver [1-5]. Aromatic dithiols are known to adsorb on gold as dithiolates by forming two Au-S bonds [6], so that, it is important to understand electrical conduction through small arrays of conjugated organic dithiol molecules that might serve as molecular wires sandwiched between two metal electrodes.

The adsorption and self-assembly of 1,4-benzenedithiol (1,4-BDT) and 1,3-benzenedithiol (1,3-BDT) was studied on a Au (111) surface using scanning tunneling microscopy (STM) [7,8]. Based on previous observations that analogous 1,4-PDI forms oligomers in which each isocyanide binds to a gold adatom [9], 1,4-BDT also adsorbs to gold by extracting adatoms from the substrate and form *zigzag* structures because two thiolate groups bound to the gold adatom can adopt either *cis* or *trans* configurations (*Figure 5.1*), in contrast to the linear chains formed from 1,4-PDI on Au (111) [6]. Unlike 1,4-PDI and 1,4-BDT, 1,3-BDT on Au (111) did not show any evidence for the creation of oligomers, or even dimers on the surface (*Figure 5.2*) [8].

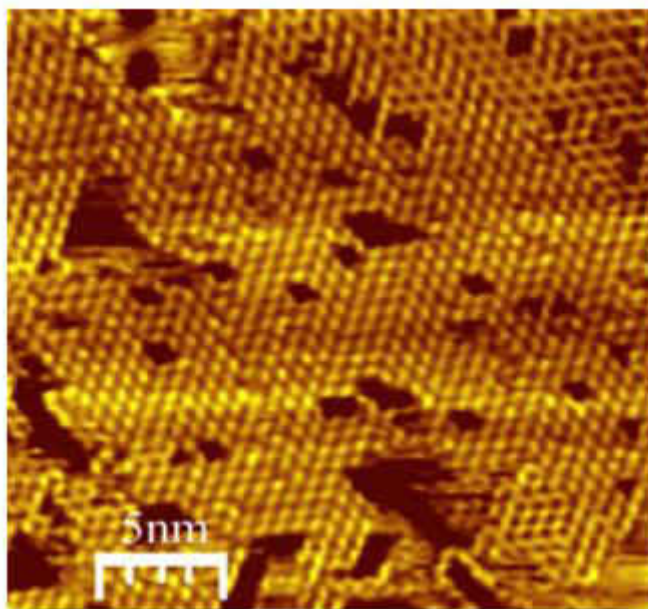


**Figure 5.1:** Large-area STM scan of a saturated layer of 1,4-BDT adsorbed on gold at 300 K ( $I_t = 163$  pA,  $V_t = 0.25$  V) showing the formation of trans-induced zigzag oligomeric chains [7,8]

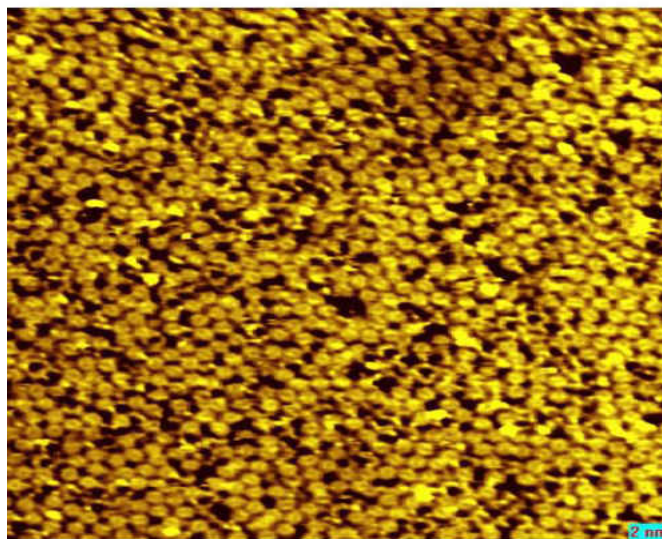


**Figure 5.2:** Saturation dose of 1,3-BDT on Au(111). The crystal was dosed and imaged at room temperature. No sign of ordered structures were observed under these conditions [8]

Because of the ability of  $-(\text{Au-PDI})-$  oligomer chains to bridge between gold nanoparticles supported on an insulating mica substrate to provide a conductive pathway between them (*Chapters 3 and 4*), similar experiments were carried out herein to explore whether 1,4-BDT and 1,3-BDT molecules can form analogous conductive bridges. The surface structures of both molecules were characterized using attenuated total internal reflection infrared spectroscopy (ATR-IR).

## 5.2 Experimental

The conductivity of 1,4-BDT on a nanoparticle array was measured as described in *Chapter 4*. Briefly, gold nanoparticles of  $\sim 8$  nm in diameter were deposited by evaporation onto a cleaved mica substrate (highest grade, Ted Pella). Gold electrodes were fabricated by masking the central portion of the mica substrate and depositing gold electrode pads  $\sim 200$  nm thick. The sample was dosed with 1,4-BDT or 1,3-BDT from solution after the gold-nanoparticle covered sample had been allowed to age until there was no further change in the sheet resistance, a process that was complete after  $\sim 2$  h, depending on the initial gold coverage. A droplet of 1,4-BDT solution (0.1 mM in benzene) was placed on the surface of the nanoparticle-covered sample for 10 s, and the excess washed away using benzene.

Electrical measurements were made in a stainless-steel vacuum chamber that was pumped by means of an ion pump to a base pressure of  $\sim 2 \times 10^{-8}$  Torr without baking to avoid altering the sample during bakeout. The sample temperature was measured by means of a chromel–alumel thermocouple, and the current versus voltage (I/V) characteristics were measured by applying a voltage via a D/A converter and the resulting current measured by means of a Keithly picoammeter that was monitored by an A/D converter to yield I/V curves directly. 1,4-benzenedithiol (1,4-BDT) and 1,3-benzenedithiol (1,3-BDT) were obtained commercially (Aldrich Chemicals, 99% purity)

and further purified by several freeze–pump–thaw cycles by heating using a water bath and cooling to allow it to recrystallize.

Infrared spectra of 1,4-BDT and 1,3-BDT adsorbed on gold films were also collected by evaporating gold onto a zinc selenide (ZnSe) ATR plate with an  $\sim 8 \text{ cm}^2$  area, and the infrared spectra collected using a Bruker Vertex infrared spectrometer operating at a resolution of  $4 \text{ cm}^{-1}$ , typically for 2000 scans using a DTGS detector. The gold film thickness was selected to allow reasonable infrared transmission through the sample to be obtained and spectra were collected after dosing with 200  $\mu\text{l}$  aliquots of a 0.1 mM 1,4-BDT and 0.1 mM 1,3-BDT solutions in benzene. The samples were allowed to dry in air for  $\sim 5$  minutes and then rinsed with benzene to remove any residual.

## 5.3 Results

### 5.3.1 Electrical studies

It has been shown previously that  $-(\text{Au-PDI})_n-$  oligomer chains are capable of bridging between gold nanoparticles deposited onto a mica surface (*Chapters 3 and 4* [9]). In this case, it was proposed that the PDI molecules are able to extract gold atoms from low-coordination sites on the gold nanoclusters and thereby propagate to form one-dimensional oligomeric chains to form molecular electronic linkages between the nanoparticles. The observation of similar effects when dosing a gold-nanoparticle-covered mica surface with 1,4-BDT would provide corroborative evidence for the formation of similar one-dimensional chains as found for PDI [7].

The variation in conductivity of a gold-nanoparticle-covered mica sample with an initial conductivity of 0.5 nS (corresponding to  $\ln(R_0/\Omega) = 21.4$ ), where  $R_0$  is the initial sheet resistance, was measured following exposure of the nanoparticle-covered mica sample to solutions of various

concentrations of 1,4-BDT for 10 s, and then washing away the excess solution with benzene, and the results are plotted in *Figure 5.3a* as a function of 1,4-BDT dose (in mmoles/cm<sup>2</sup>). This shows a rapid increase in conductivity up to ~13 nS after dosing ~0.1 mmoles/cm<sup>2</sup> of 1,4-BDT. The conductivity do not vary at higher solution doses, becoming constant at ~16 nS for doses larger than ~0.3 mmoles/cm<sup>2</sup>. *Figure 5.3b*, shows the variation in conductivity of a gold-nanoparticle-covered mica sample with the same initial resistance following exposure of the nanoparticle-covered mica sample to solutions of various doses of 1,3-BDT for 10 s and then washing away the excess solution with benzene. There was a rapid increase in conductivity to ~6 nS, for doses 0.03-0.3 mmoles/cm<sup>2</sup> of 1,3-BDT, after which the measured conductivity was stable even after dosing 0.5 mmoles/cm<sup>2</sup>.

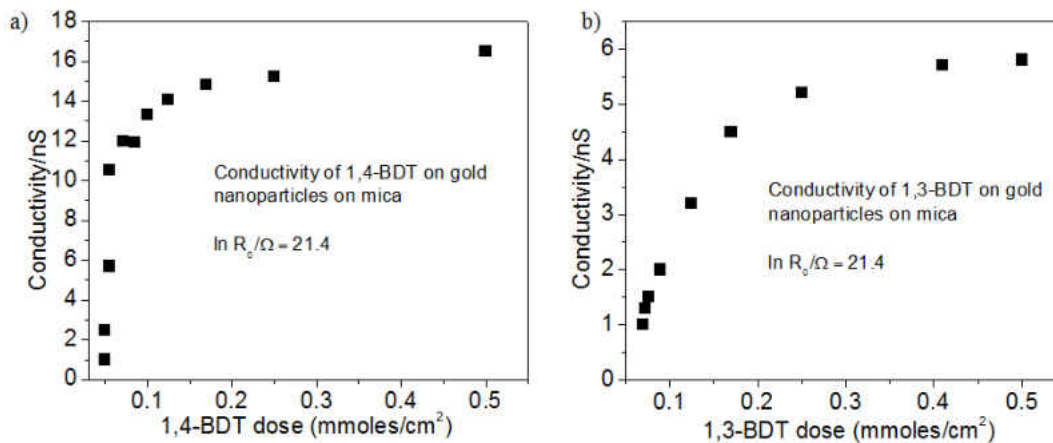


**Figure 5.3:** Variation in conductivity as a function of (a) 1,4-BDT and (b) 1,3-BDT dose in (mmoles/cm<sup>2</sup>) measured when dosing a gold-nanoparticle-covered mica surface with an initial sheet resistance  $R_0$  of  $\ln(R_0/\Omega) = 21.4$ , from solution.

Typical temperature variations in resistance of gold-nanoparticle-covered mica, saturated with 1,4-BDT or 1,3-BDT as a function of initial gold loading, indicating by changes in  $\ln(R_o)$ , are shown in *Figure 5.4a* and *5.4b*, respectively. In this case, the temperature variations in the sheet resistances  $R$  are plotted as  $\ln(R)$  versus  $1/\sqrt{T}$  rather than an Arrhenius form (where they would vary as  $1/T$ ) since this yielded linear plots, while the Arrhenius plots were curved. Similar behavior has been found for PDI-linked gold nanoparticles (*Chapter 3*) and provides corroborative evidence that 1,4-BDT [8] and 1,3-BDT form similar linkages. It has been shown previously that this behavior can be adequately reproduced for 1,4-PDI on a gold nanoparticle array by a model due to Abeles for thermally assisted tunneling through an array of nanoparticles [10].

The slopes of the plots of  $\ln(R)$  versus  $T^{-1/2}$  were obtained for films spanning a wide range of initial (undosed) conductivities,  $R_o$ . The slopes of these plots ( $\alpha$ ) was found to vary linearly with  $\ln(R_o)$  (*Figure 5.5*) for 1,4-BDT on a gold nanoparticle array. The slope of this plot was found to be  $4.2 \pm 0.1$ .

As mentioned above, electrical measurements for 1,3-BDT-linked gold nanoparticles showed an increase in conductivity of a gold-nanoparticle-covered mica sample with  $\ln(R_o/\Omega)=2.14$  (*Figure 3b*) following exposure to solutions of various doses of 1,3-BDT, to a maximum of  $\sim 6$  nS, for doses 0.03-0.3 mmol/cm<sup>2</sup> of 1,3-BDT. This is less than half the value obtained after dosing mica samples with same initial coverage with 1,4-BDT (*Figure 3a*). The slopes of the plots of  $\ln(R)$  versus  $T^{-1/2}$  were obtained for films spanning a wide range of initial (undosed) conductivities,  $R_o$ . The slopes of these plots ( $\alpha$ ) was found to vary linearly with  $\ln(R_o)$  only for samples with high initial coverages ( $> 5.00$  nS),  $\ln(R_o/\Omega) < 19.2$  (*Figure 5.6*).

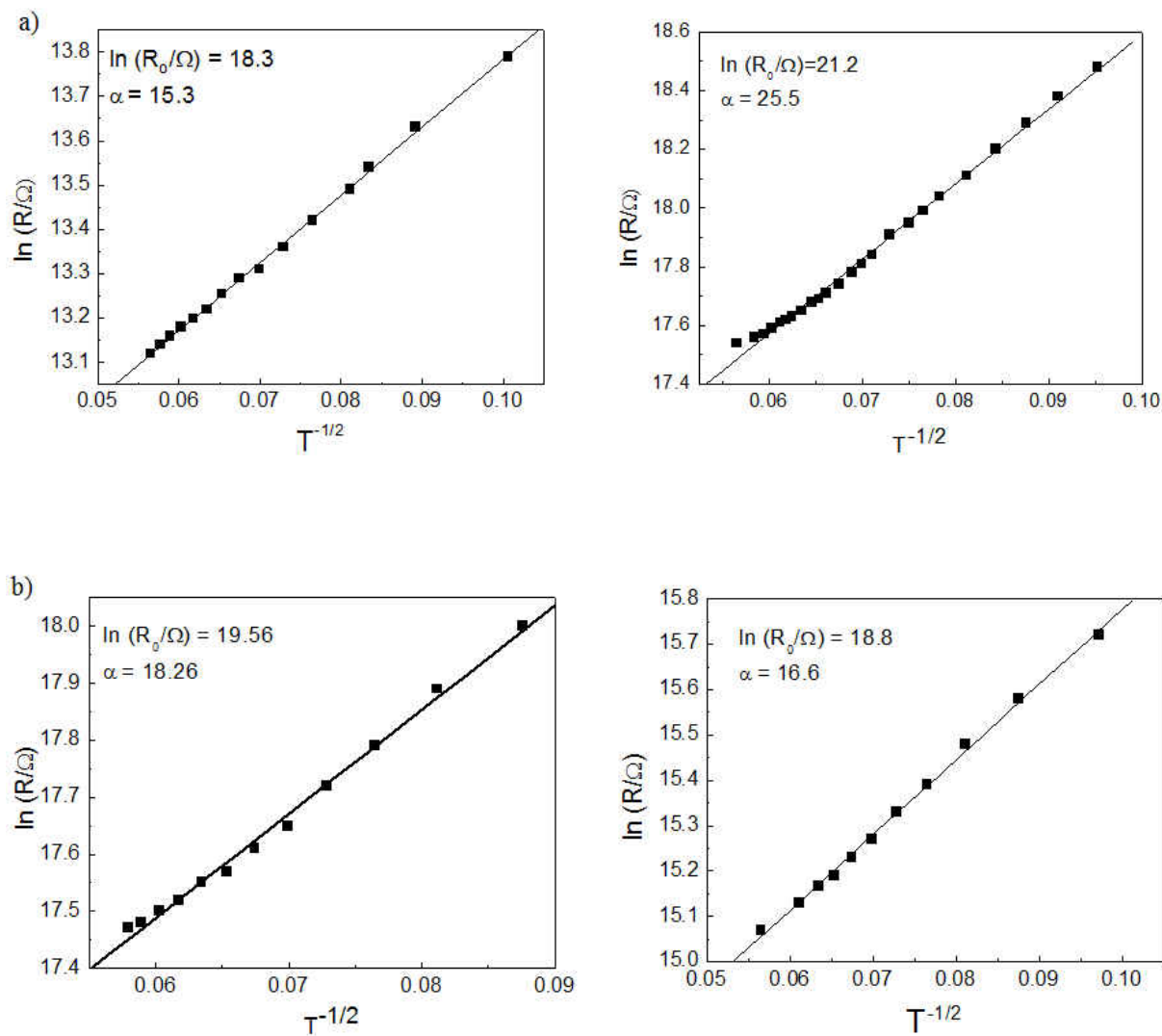


**Figure 5.4:** Typical plots of  $\ln(R/\Omega)$  versus  $T^{-1/2}$ , for a) 1,4-BDT-linked gold nanoparticles, b) 1,3-BDT-linked gold nanoparticles, where the temperature is measured in degrees in Kelvin for various films with a range of initial films resistances. The value of the initials resistance values of the films,  $R_0$ , are indicated on each of the plots.



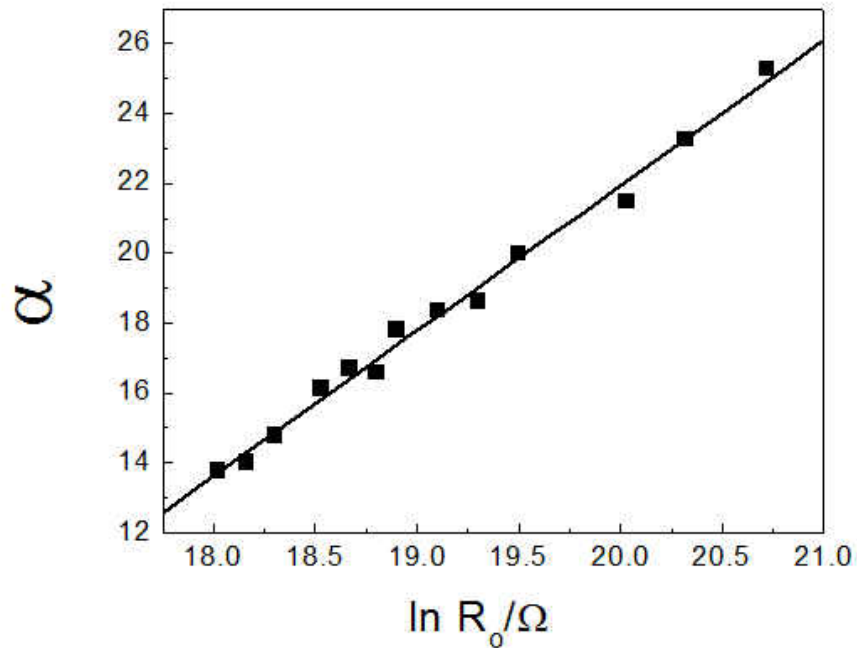


**Figure 5.5:** Plot of  $\alpha$  values versus  $\ln(R_0)$  for the 13 different films obtained for 1,4-BDT linked gold nanoparticles, with a slope of  $4.2 \pm 0.1$ . The linear fit is in agreement with the theory of activated tunneling in granular materials put forth by Abeles and Sheng [10]

As shown in *Figure 5.6*, a plot of  $\alpha$  versus  $\ln(R_0/\Omega)$  was obtained for samples over a wide range of initial conductivities, where the orange squares represent  $\alpha$  values for samples with initial conductivities between 1.00 and 5.00 nS, whereas the linear plot (black squares) represents samples with initial conductivities between 6.00 and 15.00 nS.

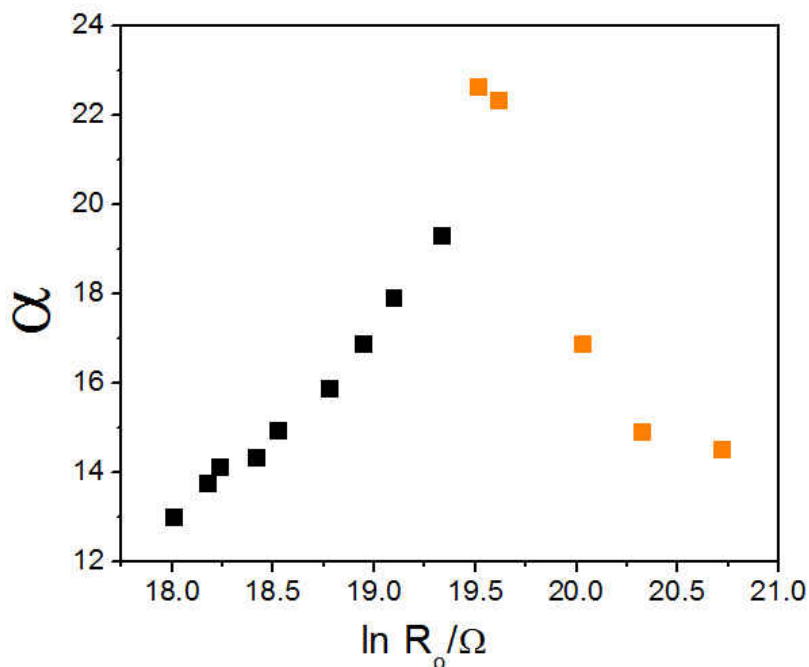


**Figure 5.6:** Plot of  $\alpha$  values versus  $\ln(R_0)$  for the 15 different films obtained for 1,3-BDT linked gold nanoparticles. Black dots represent alpha values for samples with initial conductivities vary between 6.00 and 15.00 nS, orange dots represent alpha values for samples with initial conductivities vary between 1.00 and 5.00 nS

*Figure 5.7* displays a plot of  $\ln(C_S/C_0)$  as a function of the  $\ln(R_0/\Omega)$ , where  $C_S$  is the maximum sample conductivity after dosing 1,3-BDT,  $C_0$  is initial sample conductivity before dosing 1,3-BDT, and  $R_0$  is the clean sample resistance (before dosing 1,3-BDT). This plot shows that samples with low initial gold coverage (orange squares) produce low conductivity even after dosing 1,3-BDT, whereas samples with high initial coverage (black squares) produce high conductivity after dosing 1,3-BDT. Samples with gold nanoparticle arrays with low initial conductivity produce only very small ( $\sim 1.6$ ) increases in the sample conductivity.

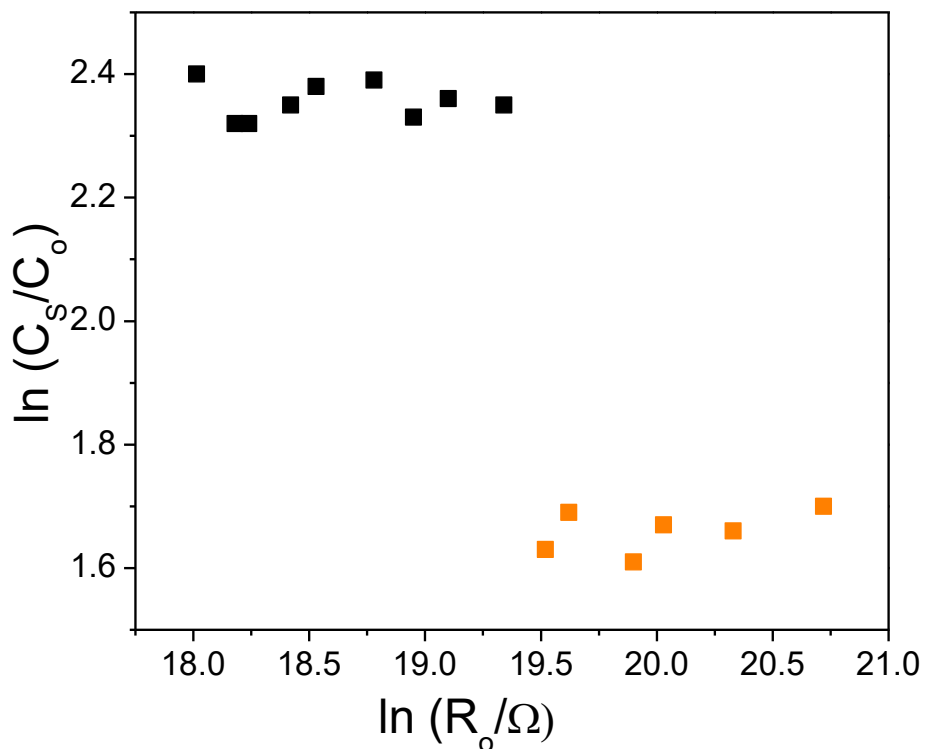


**Figure 5.7:** Plot of  $\ln(C_s/C_o)$  as a function of the  $\ln(R_o/\Omega)$ , where  $R_o$  is the clean sample resistance, shows that samples with low initial gold coverage (orange squares) produce low conductivity even after dosing 1,3-BDT, whereas samples with high initial coverage (black squares) produce high conductivity after dosing 1,3-BDT

As shown in *Figure 5.8*, an approximately straight line was obtained after plotting  $\alpha$  as a function of  $\ln(R_o)$ , where  $R_o$  is the clean sample resistance, for samples with initial conductivities for the gold nanoparticle arrays greater than 5.00 nS, with a slope equal to  $4.8 \pm 0.3$ .

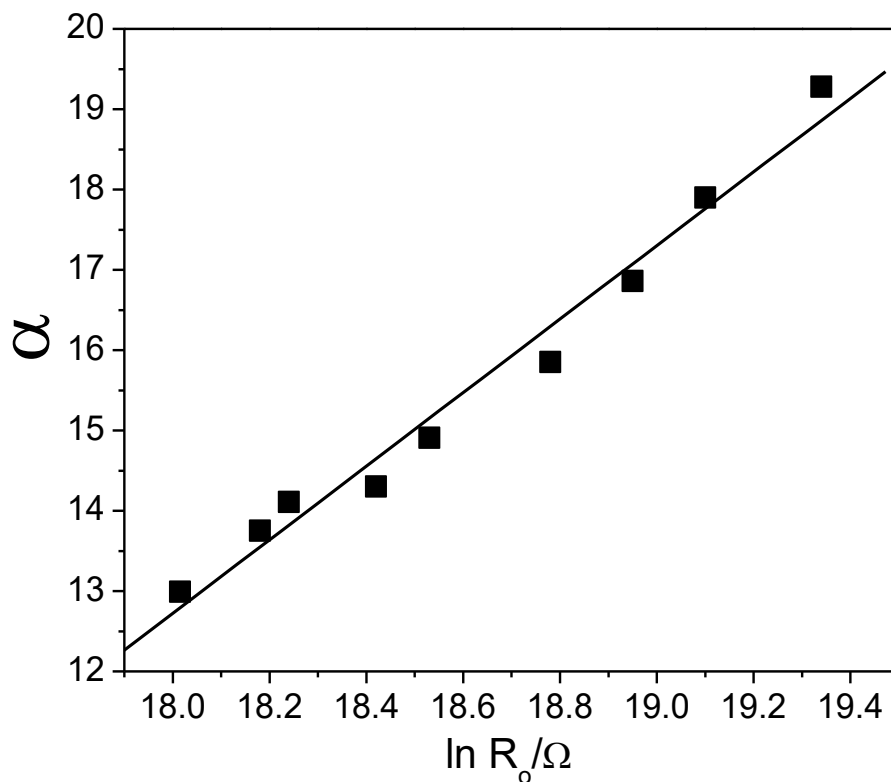


**Figure 5.8:** Plot of  $\alpha$  values for 1,3-BDT linked gold nanoparticles for samples with high initial conductivity ( $> 5.00$  nS), the slope is equal to  $4.6 \pm 0.3$

### 5.3.2 Attenuated total internal reflection infrared spectroscopy (ATR-IR) characteristics

*Figures 5.9 and 5.10* show ATR-IR spectra for 1,4-BDT and 1,3-BDT respectively as a function of BDT dosed in nmoles per  $\text{cm}^2$  of the crystal. The infrared spectra were collected after dosing a gold film-covered ZnSe crystal with 0.1 mM aliquots of BDT, then allowing the sample to dry in air for  $\sim 5$  minutes and then rinsing with benzene to remove any residual, weakly bonded molecules.

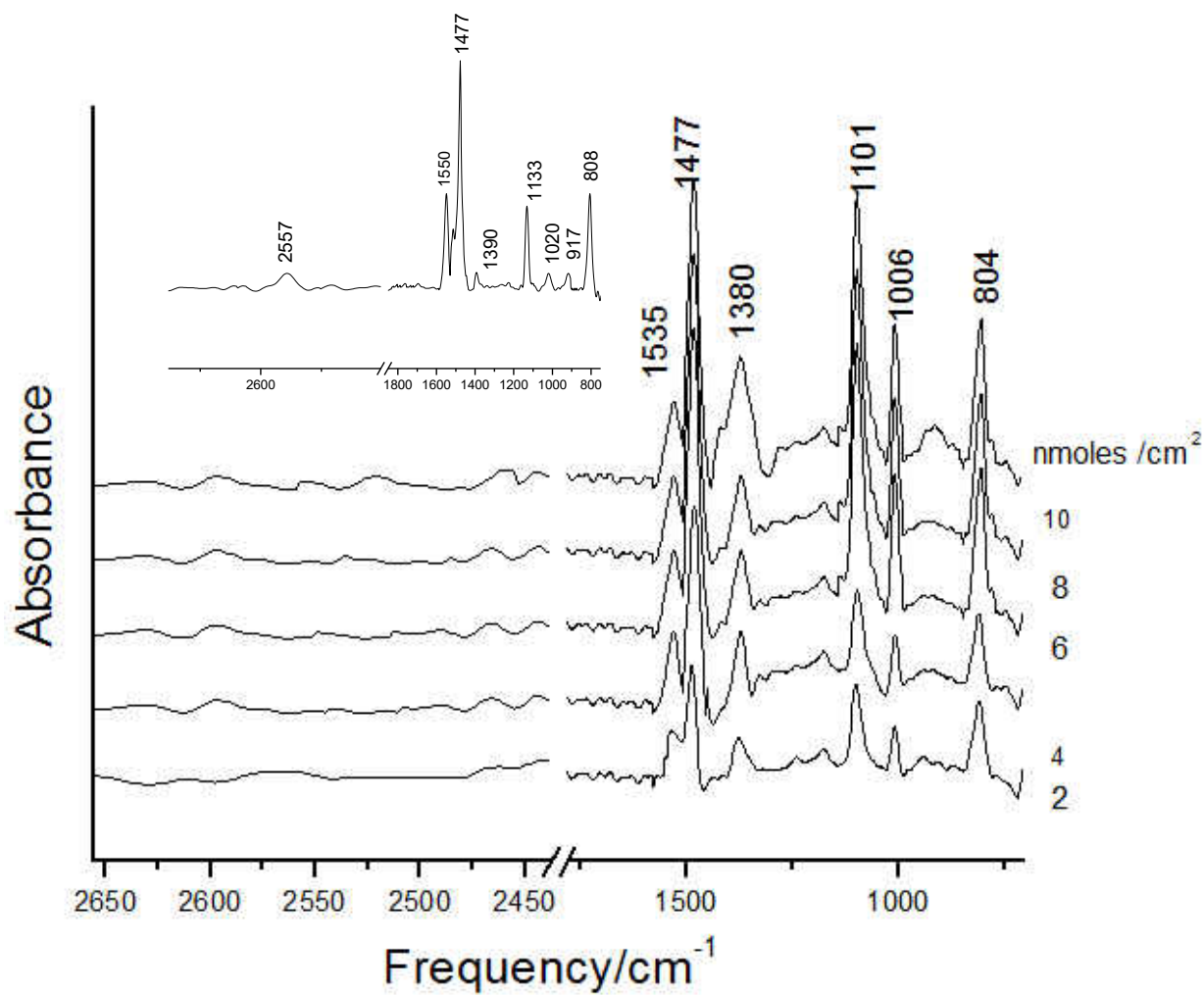


**Figure 5.9:** A series of ATR infrared spectra of 1,4-BDT adsorbed on a thin gold film using aliquots of 200  $\mu\text{l}$  of solution of 0.1 mM 1,4-BDT. The resulting BDT doses, in  $\text{nmol}/\text{cm}^2$ , are indicated adjacent to the corresponding spectrum. The inset is a spectrum of 0.1 mM solution of pure 1,4-BDT in benzene.

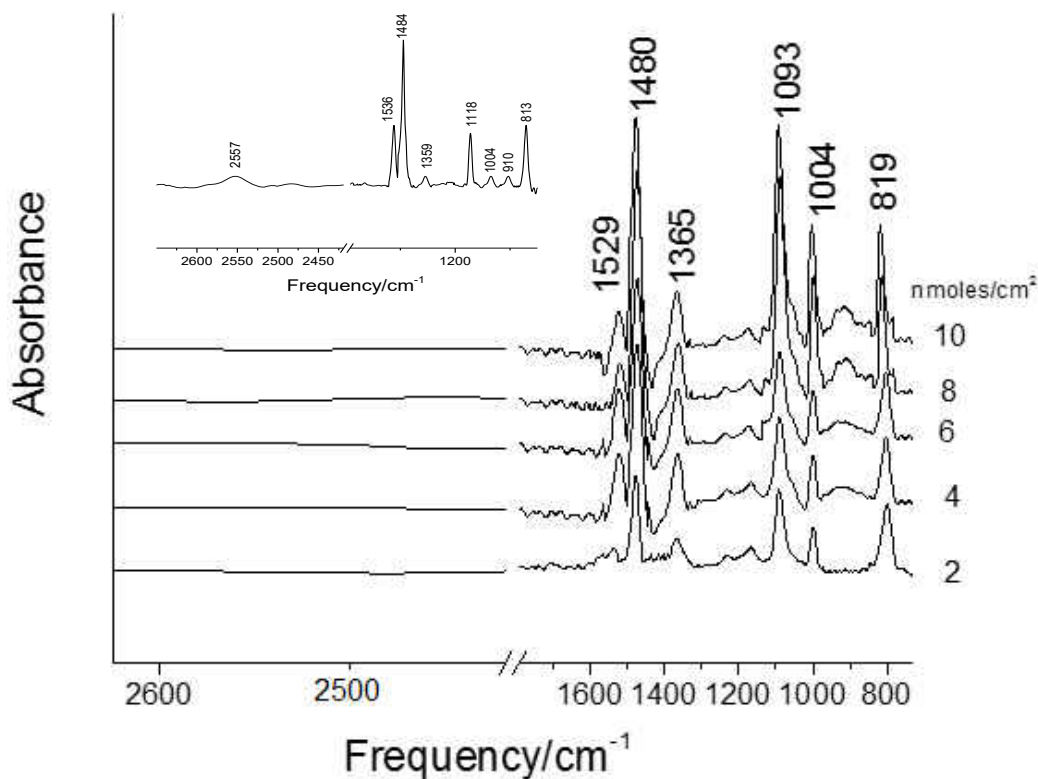


**Figure 5.10:** A series of ATR infrared spectra of 1,3-BDT adsorbed on a thin gold film using aliquots of 200  $\mu\text{l}$  of solution of 0.1 mM 1,3-BDT. The resulting BDT doses, in mole/ $\text{cm}^2$ , are indicated adjacent to the corresponding spectrum. The inset is spectrum of 0.1 mM solution of pure 1,3-BDT in benzene.

It is common to use  $D_{2h}$  symmetry for 1,4-BDT [7] and the resulting symmetry assignments based on this point group are also shown in *Table 5.1*. The majority of the observed modes are due to aryl ring vibrations, as shown in the insets of *Figures 5.9* and *5.10* for pure 1,4- and 1,3-BDT. S-H rocking vibrations are evident at  $\sim 917\text{ cm}^{-1}$  and stretching modes appear as a broad band centered at  $\sim 2557\text{ cm}^{-1}$ . The ring modes are still evident for BDT-linked gold nanoparticle arrays. However, the most drastic changes are noted for the S-H bending and stretching modes, where

the absence of the  $\sim 917\text{ cm}^{-1}$  S–H rocking and S–H stretching modes at  $\sim 2557\text{ cm}^{-1}$  indicates the formation of a dithiolate species. An intense mode is found at  $\sim 804\text{ cm}^{-1}$  and  $\sim 819\text{ cm}^{-1}$  suggests that 1,4-BDT forms one-dimensional oligomer chains with the aryl ring parallel to the surface since this mode is assigned to an out-of-plane C–H bending mode [11]. However, the appearance of a ring vibration at  $\sim 1101\text{ cm}^{-1}$  indicates that some of the aryl rings are tilted with respect to the surface.

Frequency ( $\text{cm}^{-1}$ ) of 1,4-BDT in solution	Frequency ( $\text{cm}^{-1}$ ) of 1,4-BDT adsorbed on Au nanoparticle array	Assignment
808	804	B <sub>3u</sub>
917	-	SH rock
1020	1006	B <sub>1u</sub>
1133	1101	B <sub>2u</sub>
1390	1380	B <sub>2u</sub>
1477	1477	B <sub>1u</sub>
1550	1535	B <sub>1u</sub>
2557	-	SH stretch

**Table 5.1:** Vibrational frequencies and assignments of pure 1,4-BDT in solution, and adsorbed on a gold nanoparticle array

The vibrational spectrum for 1,3-BDT on a gold film is very similar to that for 1,4-BDT and the frequencies are summarized in *Table 5.2*. In particular, the absence of S-H rocking and stretching modes following adsorption on the gold film indicate the formation of a dithiolate species on the surface.

Frequency (cm <sup>-1</sup> ) of 1,4-BDT in solution	Frequency (cm <sup>-1</sup> ) of 1,4-BDT adsorbed on Au nanoparticle array	Assignment
813	819	SH rock
910	-	
1004	1004	
1118	1093	
1359	1365	
1484	1480	
1535	1529	
2557	-	SH stretch

**Table 5.2:** Vibrational frequencies and assignments of pure 1,3-BDT in solution, and adsorbed on a gold nanoparticle array

## 5.4 Discussion

ATR-IR spectra for pure 1,4-BDT and 1,3-BDT are similar to that reported for 1,4-BDT on Au(111) [7]. For pure BDT solutions, vibrational modes at  $\sim 804\text{ cm}^{-1}$ ,  $\sim 1006\text{ cm}^{-1}$ ,  $\sim 1100\text{ cm}^{-1}$ ,  $1380\text{ cm}^{-1}$ ,  $\sim 1480\text{ cm}^{-1}$ , and  $\sim 1560\text{ cm}^{-1}$  can be assigned to benzene ring modes (*Tables 5.1 and 5.2*). Vibrational modes at  $\sim 2550\text{ cm}^{-1}$  and  $\sim 907\text{ cm}^{-1}$  are assigned to S-H stretching and rocking modes respectively. After adsorbing BDT onto a gold film, ring modes are still evident but drastic changes are noted for the S-H bending and stretching modes, where the absence of the  $\sim 917\text{ cm}^{-1}$  S-H rocking and S-H stretching mode at  $\sim 2557\text{ cm}^{-1}$  indicates the formation of dithiolate species.

It was found previously that the diisocyanide oligomers could bridge between gold nanoparticles on a mica substrate to form a conductive pathway between them (*Chapters 4 and 5*). Similar behavior appears to occur for BDT, where the resistance decreases substantially as shown



in *Figure 5.3*. The conductivity increased when increasing the BDT dose, where the same concentration of 1,4-BDT and 1,3-BDT were used for these experiments. However, according to data shown in *Figure 5.3*, 1,4-BDT adsorption was able to increase the conductivity of a nanoparticle array by three times more than 1,3-BDT, although same initial gold coverage was used for both samples with identical BDT concentrations (0.1 mM). According to scanning tunneling microscopy (STM) studies, 1,4-BDT adsorbs on Au(111) surfaces with the two thiolate groups bound to a gold adatom to generate an extended *zig-zag* chains (*Figure 5.1*)[7]. On the other hand, 1,3-BDT molecules do not form extended oligomeric structures, in contrast to the other molecules used in this work. STM studies showed that 1,3-BDT molecules were exclusively observed as monomeric species (*Figure 5.2*) [8]. This effect was investigated using density functional theory (DFT) where the resulting most stable structures of adsorbed 1,4-BDT, both directly bonded to Au(111) and to a gold adatom, are displayed in *Figure 5.11*. Adsorption energies were calculated from the difference between the sum of the energy of the clean surface plus the gas-phase molecule energy, and the energy of the molecule adsorbed on the surface. The  $\eta^1$ -thiolate is more stable on the Au(111) surface on the bridge ( $E_{\text{ads}} = \sim 172$  kJ/mol) and 3-fold sites ( $E_{\text{ads}} = \sim 174$  kJ/mol) than the atop site ( $E_{\text{ads}} = \sim 102$  kJ/mol). However, binding to a gold adatom substantially stabilizes the adsorbed thiolate ( $E_{\text{ads}} = \sim 226$  kJ/mol). The thiolate group binds to one side of the gold adatom with the S–H group remote from the surface, thereby preventing it from directly accessing the surface and suggesting that it should oligomerize in a similar fashion as found for PDI [9] as found experimentally in this chapter.

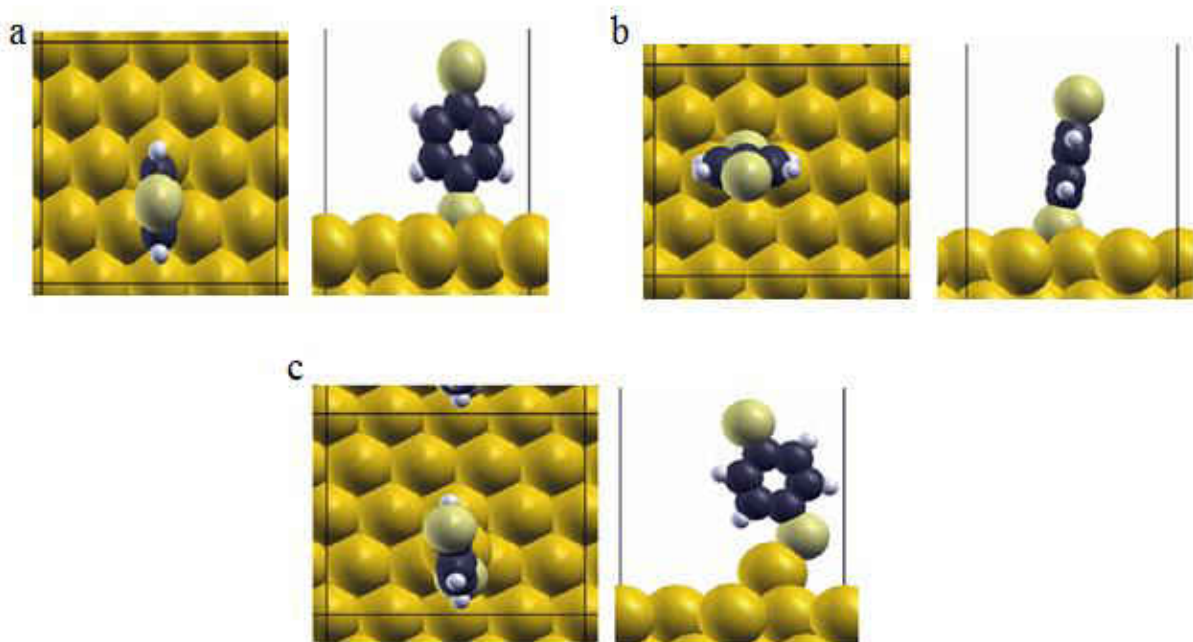


**Figure 5.11:** Most stable structures obtained by DFT calculations for  $\eta_1$ -thiolates from 1,4-BDT adsorbed on Au(111) surfaces: (a) a hollow site ( $E_{\text{ads}} = 174$  kJ/mol) (b) a bridge site ( $E_{\text{ads}} = 172$  kJ/mol), and (c) on a gold adatom ( $E_{\text{ads}} = 226$  kJ/mol).

Similar DFT calculations were also carried out for various 1,3-BDT species on Au(111). As shown in *Figure 5.12*, the structure of an upright molecule was calculated with one thiolate coordinated to a gold adatom with an absorption energy of -180 kJ/mol. A more stable structure was obtained when both thiolates were bonded to the gold surface and a gold adatom ( $E_{\text{ads}} = -321$  kJ/mol), while the most stable structure was obtained when both thiolate groups were bonded to gold adatoms ( $E_{\text{ads}} = -381$  kJ/mol), and explains the lower mobility for surfaces exposed to 1,3-BDT as well as their lower conductivity.

The temperature dependences are also similar to that found for diisocyanide-linked gold nanoparticles (*Chapter 3*) and yield linear plots of  $\alpha$  versus  $\ln$  (initial film resistance) (*Figures 5.5*

and 5.8). The slope of this plot is proportional to  $\sqrt{(X_F/X_C \epsilon_F)}$  where the subscript  $C$  refers to the undosed nanoparticle array,  $F$  to an array of linked nanoparticles,  $X = \sqrt{2m\phi/\hbar^2}$ , where  $\phi$  is the height of the tunneling barrier, and  $\epsilon_F$  is the dielectric constant.

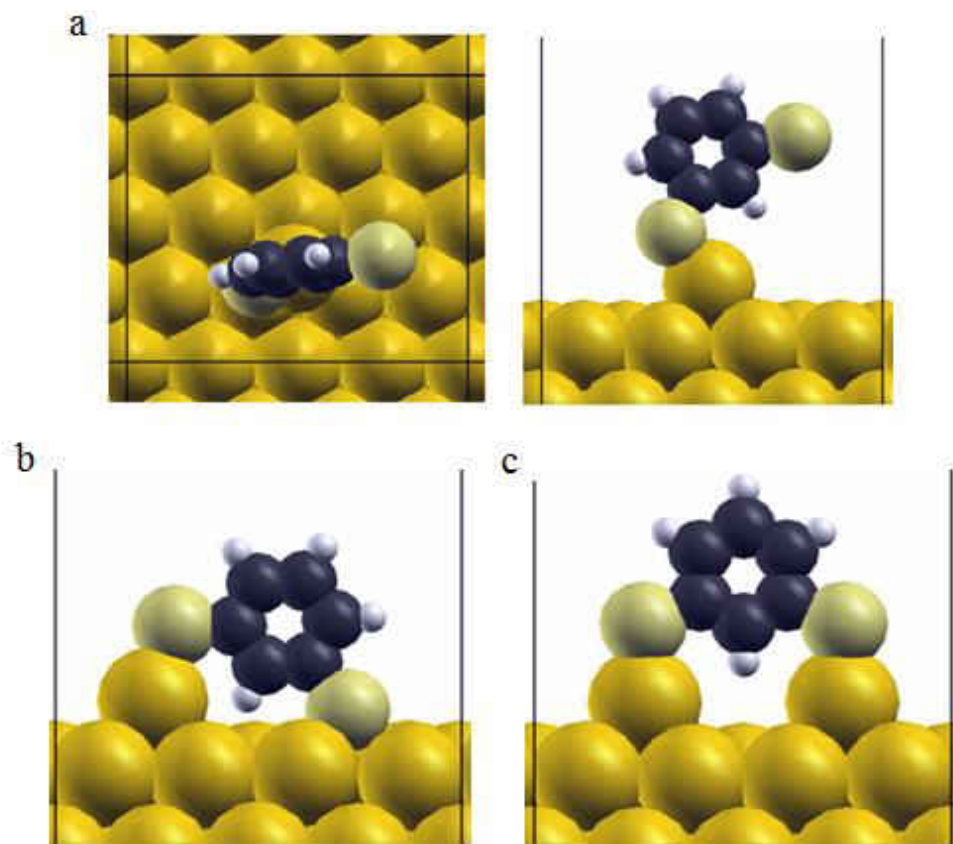


**Figure 5.12:** Structures obtained by DFT calculations for 1,3-BDT adsorbed on Au(111) surfaces: (a) top view of  $\eta^1$  adatom complex of 1,3-BDT ( $E_{\text{ads}} = -180$  kJ/mol) (b) One thiol is bonded to a gold adatom and the other to the hollow site of Au(111) surface ( $E_{\text{ads}} = -321$  kJ/mol), and (c) both thiolates are bonded to gold adatoms ( $E_{\text{ads}} = 381$  kJ/mol).

The Abeles model predicts that the value of  $\alpha$  in the above equation should depend on  $\ln$  (initial film resistance) and such a plot is displayed in *Figure 5.5*, for gold nanoparticles linked

with 1,4-BDT molecules, which yields a good straight line with a slope of  $4.2 \pm 0.1$ , which is slightly higher than for the corresponding plot for PDI-linked nanoparticles (slope =  $3.7 \pm 0.2$ ). By using the  $4.2 \pm 0.2$  slope value, and assuming that the dielectric constant ( $\epsilon_F$ ) = 3.5, similar to that for PDI and using the work function of gold = 4.08 eV, the calculated value of the tunneling barrier of gold nanoparticles linked with 1,4-BDT molecules is  $0.17 \pm 0.3$  eV.

Measurements of the conductivity change as a function of temperature for samples of 1,3-BDT-linked gold nanoparticles, yielded two regimes (*Figure 5.6*), where dosing samples with low initial conductivities with 1,3-BDT did not lead to a plot of  $\alpha$  versus  $\ln(R_o/\Omega)$  that correspond to the straight line shown in *Figure 5.8*. The samples with high initial gold coverages yielded a value of  $\alpha$  to  $4.8 \pm 0.25$  (*Figure 5.8*). According to Abeles model discussed before, the calculated tunneling barrier between the gold electrode Fermi level for 1,3-BDT is  $\sim 0.29$  eV. As shown by STM imaging (*Figure 5.2*), 1,3-BDT does not form chains on Au (111). This implies that at low gold nanoparticle coverages, the spacing between adjacent gold nanoparticles is large sufficiently to prevent 1,3-BDT molecules for forming conductive bridges between them. At higher gold nanoparticle coverages, the spacing between adjacent gold nanoparticles reduces so that 1,3-BDT molecules can now form conductive bridges between closely spaced adjacent gold nanoparticles.

Since the plot of  $\alpha$  versus  $\ln(R_o/\Omega)$  for 1,3-BDT on a gold nanoparticle array deviates from linearity at a value of  $\ln(R_o/\Omega) \sim 19$ , this implies that only larger gold nanoparticle coverages (with lower sheet resistances) can be bridged without forming oligomer chains. If it is assumed that a 1,3-BDT molecule can attach from each gold nanoparticle, and taking a gold atom spacing for 1,3-BDT on gold to be  $\sim 0.5$  nm (*Figure 5.12*), suggests that the interparticle spacing is  $\sim 1$  nm. Thus, for values of  $\ln(R_o/\Omega)$  less than  $\sim 19$ , there exists a percolation pathway between adjacent nanoparticles that bridge between electrodes that is  $\sim 1$  nm. This further implies that gold

nanoparticle arrays with higher initial resistance have larger interparticle separations and strongly suggests that they are bridged by several molecules by forming oligomer chains.

In addition, the observation that the plots of  $\alpha$  versus  $\ln(R_0/\Omega)$  are linear for  $\ln(R_0/\Omega)$  values greater than  $\sim 19$  (for example 1,4-BDT, *Figure 5*), implies that the conductive properties of the oligomer chains are primarily dictated by the individual repeat units, rather than the whole oligomer.

## 5.5 Conclusion

In this chapter, the surface structure and electrical properties of 1,4-benzenedithiol and 1,3-benzenedithiol oligomers on gold films was investigated. ATR-IR results show that the vibrational modes at  $\sim 2550\text{ cm}^{-1}$  and  $\sim 907\text{ cm}^{-1}$  that are assigned to S-H stretching and rocking modes respectively disappear after adsorbing BDT molecules on gold, which confirms the formation of S-Au bonds. Conductivity measurements reveal that 1,4-BDT is a better conductor than 1,3-BDT due to the ability of 1,4-BDT to oligomerize on gold and this result was confirmed using both STM and DFT.

STM images show that 1,4-BDT form *zig-zag* chains on Au(111) [7], whereas 1,3-BDT does not form ordered structures under the same conditions [8]. DFT calculations show that 1,4-BDT has an upright orientation on the Au(111) surface, which provides high mobility for these molecules and the ability to move on the surface to form chains. 1,3-BDT has a different structure that causes both thiols to bond to gold adatoms, which rationalizes why this molecule has little mobility on the surface and form chains. However, at higher gold coverages ( $>4\text{ nS}$ ), the presence of more closely spaced gold nanoparticles allows 1,3-BDT molecules to bond to adjacent gold nanoparticles and form conductive bridges between them.

## References

- [1] Laibinis, P. E.; Whitesides, G. M.; Allara, D. L.; Tao, Y.-T.; Parikh, A. N.; Nuzzo, R. G. *J. Am. Chem. Soc.* **1991**, *113*, 7152.
- [2] Nuzzo, R. G.; Zegarski, B. R.; Dubois, L. H. *J. Am. Chem. Soc.* **1987**, *109*, 733.
- [3] Joo, T. H.; Kim, K.; Kim, M. S. *J. Mol. Struct.* **1987**, *162*, 191.
- [4] Kwon, C. K.; Kim, K.; Kim, M. S. *J. Mol. Struct.* **1989**, *197*, 171.
- [5] Alves, C. A.; Smith, E. L.; Porter, M. D. *J. Am. Chem. Soc.* **1992**, *114*, 1222.
- [6] Nupur, G.; Edwin C.; Randall L. *Langmuir* **2002**, *18*, 2717-2726
- [7] Kestell, J.; Abuflaha, R.; Garvey, M.; Tysoe W. T.; *J. Phys. Chem. C* **2015**, *119*, 23042–23051
- [8] Kestell, J. 2014. Ph.D. dissertation, University of Wisconsin-Milwaukee.
- [9] Kestell, J.; Abuflaha, R.; Boscoboinik, J.; Bai, Y.; Bennett, D.; Tysoe, W.T.; *Chem. Comm.* **2012**, *49*, 1422-4.
- [10] Abeles, B.; Sheng, P.; Coutts, M. D.; Arie, Y. *Advances in Physics* **1975**, *24*, 407.
- [11] Kestell, J.; Abuflaha, R.; Boscoboinik, J. A.; Garvey, M.; Bennett, D. W.; Tysoe, W. T.; *J. Phys. Chem. Lett.* **2014**, *5*, 3577– 3581.

## Chapter 6

# Surface Chemistry and Electron Transport of 4,4'- Biphenyldiisocyanide and 4,4''-Terphenyldiisocyanide on Gold Films from Solution

### 6.1 Introduction

It was demonstrated in *Chapter 3* that 1,4-phenylene diisocyanide (1,4-PDI) self assembles with gold to form oligomers that are sufficiently mobile to bridge between gold nanoparticles; the conductivity of gold nanoparticles on mica increases substantially when exposed to PDI. The barrier height of the bridging oligomer is  $0.10 \pm 0.02$  eV [1]. In *Chapter 4*, infrared spectra were analyzed for 1,4-PDI on gold films dosed from solution as a function of solution dose using attenuated total internal reflection infrared spectroscopy (ATR-IR) to determine the structure and orientation of adsorbed PDI, which displayed a single isocyanide stretching mode at low solution exposures, consistent with the presence of  $-(\text{Au-PDI})-$  oligomer chains. Higher PDI doses causes the isocyanide mode to split into two features, one of which is due to a free isocyanide [2], indicative of a change from parallel to perpendicular adsorption geometry (*Chapter 5*).

Many previous studies explored the adsorption of organic cyanides on metal surfaces [3-8]. SAMs prepared from the diisocyanides that have a flexible alkyl chain between the two isocyanide end groups were found to form monolayer films in which both isocyanide groups are bound to the surface [3]. SAMs prepared from the diisocyanides that have rigid aryl or phenylethynyl structures between the two isocyanide end groups, were found to bind to gold

through only one  $C\equiv N$  group [3]. Analyses of the RAIR spectra of these SAMs are consistent with surface selection rules for adsorbates that are oriented with their long molecular axes normal to the surface. Measurements of advancing water droplet contact angles and ellipsometric film thicknesses of aromatic diisocyanide SAMs further support a surface structure in which the diisocyanide molecules are oriented vertically with one  $C\equiv N$  group bound to the surface and the other remote from the surface [4-6].

Analogous systems are 4,4'-biphenyldiisocyanide (BPDI) and 4,4''-terphenyldiisocyanide (TPDI) self-assembled monolayers with vertical orientation on different metal surfaces [4,6], where a small contact barrier can be formed as the delocalized  $\pi$  orbitals allow electron density to shift between the metal and the molecule [3]. BPDI and TPDI SAMs were characterized by polarization-modulated infrared reflection-absorption spectroscopy (PM-IRRAS), and grazing-angle attenuated total reflectance infrared spectroscopy (GATR). Based on the position of the metal-coordinated isocyanide stretching band, IR data show that the BPDI and TPDI molecules have a high degree of alignment perpendicular to the interface. The IR data suggest that the isocyanide SAMs bind on gold with terminal  $\eta^1$  geometry, since two  $N\equiv C$  stretching frequencies were observed, one for the coordinated end of the isocyanide ( $\sim 2190\text{ cm}^{-1}$ ) and the other for the free end ( $\sim 2122\text{ cm}^{-1}$ ) [3-7]. However, it was found in *Chapter 4* that PDI could undergo a transition from forming chains parallel to the surface, to forming perpendicular species as the PDI coverage increases. This raises the possibility that similar behavior might occur for longer-chain diisocyanides and this is explored in this chapter.

Here, electrical measurements have been made for gold nanoparticles linked with BPDI and TPDI SAMs dosed from solution. The conductivity of gold-nanoparticle arrays grown on mica



substrate were measured after exposure to BPDI and TPDI from solution. A decrease in resistance was found when gold nanoparticle arrays on mica were dosed with BPDI and TPDI.

Adsorbed overlayers of BPDI and TPDI on gold films were also characterized using ATR-IR as a function of solution dose. The results show that, at lower doses, a single isocyanide peak appears at a similar frequency to that found for 1,4-PDI molecules on gold. At higher exposures, the free isocyanide mode appears in accord with BPDI and TPDI decoordinating to form  $\eta^1$  species, similar to the behavior found for 1,4-PDI.

## 6.2 Experimental

The conductivity of BPDI and TPDI on nanoparticle-covered mica was measured as described in detail in previous chapters. Briefly, after gold electrodes were fabricated, gold nanoparticle arrays were deposited between gold electrodes to some initial resistance. The film was then left to age until there was no further change in the sheet resistance (*Figure 3.1, Chapter 3*). A series of samples with different initial resistance values were prepared and dosed with various volumes of 4 mM BPDI and 4 mM TPDI solutions. Electrical measurements were made in a HV chamber where the temperature was monitored by means of a chromel-alumel thermocouple attached to the sample, and the *I/V* characteristics were measured by applying a voltage *via* a D/A converter and the resulting current measured by means of a picoammeter that was monitored by an A/D converter to yield *I/V* curves directly.

The concentration dependence of conductivity was measured by preparing a sample with an initial conductivity of  $\sim 0.4$  nS, and the sample was dosed with 30  $\mu$ L aliquots of 0.005 mM BPDI and 0.005 mM TPDI solutions in benzene using an Eppendorf pipette on the surface of the nanoparticle-covered sample until all of the solvent had evaporated. The sample was then rinsed with benzene to remove any remaining weakly bound diisocyanides and allowed to dry in air. The

conductivity was measured under vacuum at a base pressure of  $\sim 2 \times 10^{-8}$  Torr. The sample was then taken out of the chamber, dosed again with 30  $\mu\text{L}$  aliquots of 0.05 mM solutions, the dosed samples were rinsed with pure benzene to remove excess diisocyanide, and the conductivity was again measured under vacuum. This process was repeated several times until the sample was saturated and there was no further change in conductivity.

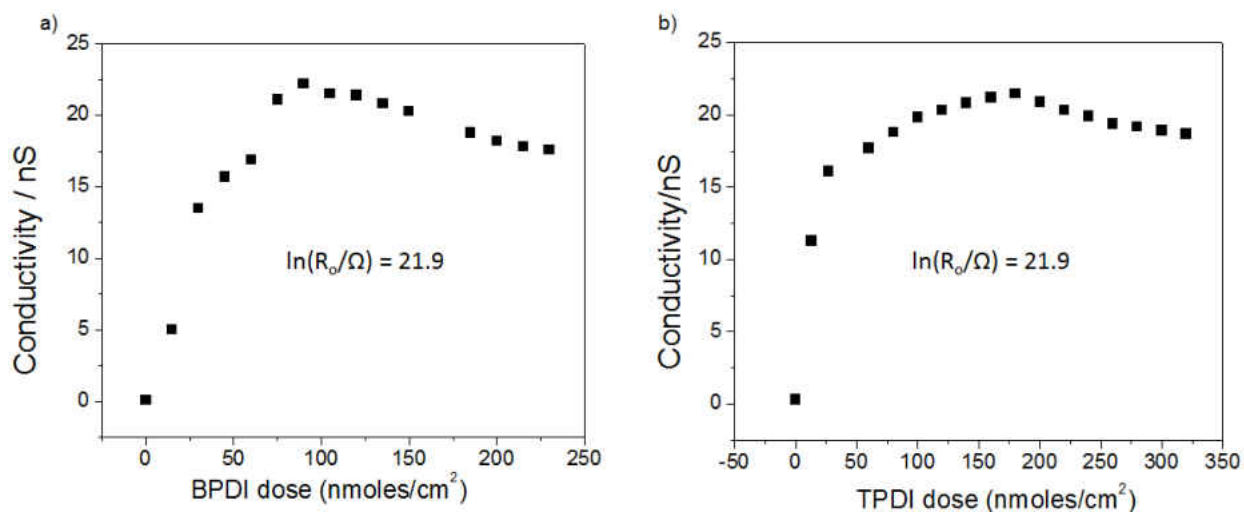
Infrared spectra of BPDI and TPDI adsorbed on gold films were also collected by evaporating gold onto a zinc selenide ATR plate with an  $\sim 8 \text{ cm}^2$  area, and the infrared spectra collected using a Bruker Vertex infrared spectrometer operating at a resolution of  $4 \text{ cm}^{-1}$ , typically for 2000 scans using a DTGS detector. The gold film thickness was selected to allow reasonable infrared transmission through the sample to be obtained and spectra were collected after dosing with 200  $\mu\text{l}$  aliquots of a 0.05 mM diisocyanide solutions in benzene. The sample was allowed to dry in air and then rinsed with benzene to remove any residual, weakly bound molecules.

## 6.3 Results

### 6.3.1 Electrical Studies

The conductive properties of gold nanoparticles deposited onto a mica substrate exposed to aliquots of 0.05 mM BPDI solutions in benzene are summarized in *Figure 6.1a*. In this case, the BPDI dose was normalized to the total area of the nanoparticle array between the gold electrodes. The initial conductivity of the sample before dosing BPDI was  $\sim 0.4 \text{ nS}$ . The conductivity of the sample increased substantially as the BPDI concentration was increasing to reach a maximum value of  $\sim 22 \text{ nS}$ , after a BPDI dose of  $\sim 90 \text{ nanomoles/cm}^2$ . At higher doses, the conductivity decreased slightly, to a value of  $\sim 17.6 \text{ nS}$ . *Figure 6.1b* displays the conductive properties of a gold nanoparticle array exposed to aliquots of 0.05 mM TPDI solutions in benzene. Before dosing with

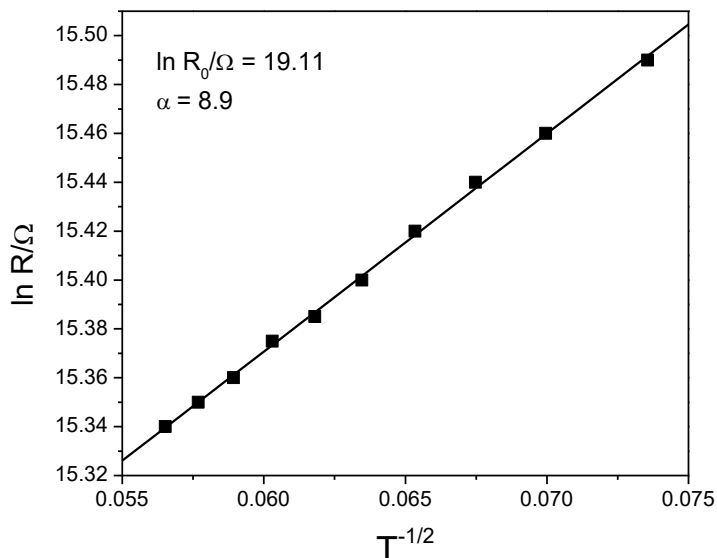
TPDI, the initial conductivity was  $\sim 0.2$  nS, and a considerable increase in conductivity to a maximum value of  $\sim 25$  nS was observed after dosing with  $\sim 180$  nanomoles/cm<sup>2</sup> of TPDI, then a slight decrease in conductivity was observed at higher doses.



**Figure 6.1:** Plot of the conductivity of gold nanoparticles deposited onto a mica substrate, with an initial conductivity of 0.4 nS ( $\ln(R_0/\Omega) = 21.9$ ) after exposure to aliquots of (a) 0.05 mM BPDI in benzene as a function of the solution dose in nmole/cm<sup>2</sup>, and (b) 0.05 mM TPDI in benzene as a function of the solution dose in nmole/cm<sup>2</sup>

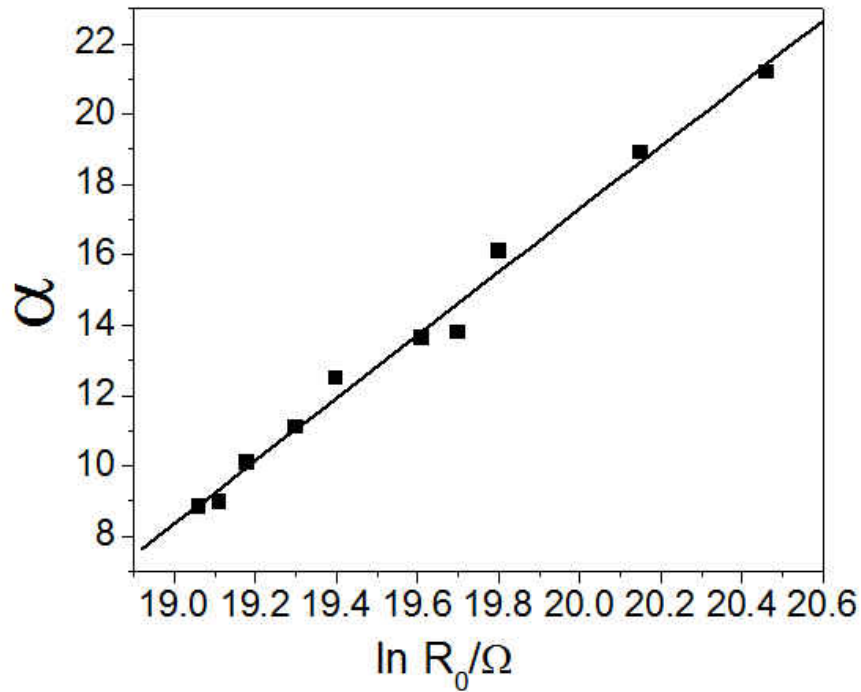
It has been shown previously that  $-(\text{Au}-\text{PDI})_n-$  oligomer chains are capable of bridging between gold nanoparticles deposited onto a mica surface and enhance the conductivity between gold electrodes (*Chapter 3*). A similar effect observed here when dosing a gold-nanoparticle covered mica surface with BPDI and TPDI provides evidence for the formation of similar one-dimensional chains as found for 1,4-PDI. The resistance varied as a function of the sample temperature and, in *Figure 6.2*, a typical resistance variation with temperature is plotted as  $\ln(R)$  versus  $T^{-1/2}$ . This variation is consistent with the Abeles model for thermally assisted tunneling

through an array of nanoparticles [9]. This linear behavior provides evidence that  $-(\text{Au}-\text{BPDI})_n-$  oligomer chains are formed between gold nanoparticles. Additional evidence for the formation of oligomeric bridges between particles is that the value of  $\alpha$  (the slope of  $\ln(R)$  versus  $T^{-1/2}$  plots) varies linearly with  $\ln(R_o)$  as shown in *Figure 6.3*, where  $R_o$  is the initial resistance of the gold nanoparticle array before dosing.



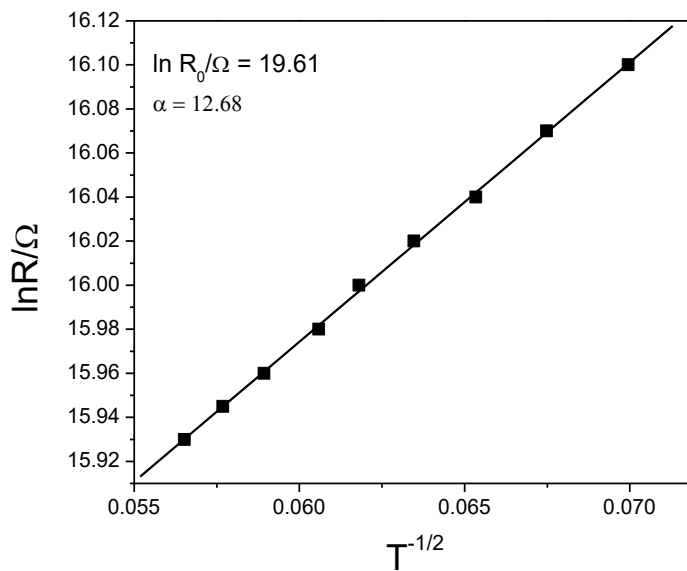
**Figure 6.2:** The linear  $\ln(R)$  versus  $T^{-1/2}$  dependence for a sample with initial conductivity of 3.00 nS dosed with 0.15  $\mu\text{mole}/\text{cm}^2$  of BPDI, is predicted by the model of Abeles and Sheng.  $R_o$  is the sheet resistance of the film prior to dosing

The slopes of the plots of  $\ln(R)$  versus  $T^{-1/2}$  were obtained for BPDI-linked gold nanoparticles films spanning a wide range of initial (undosed) conductivities,  $R_o$ . The slopes of these plots ( $\alpha$ ) was found to vary linearly with  $\ln(R_o)$  (*Figure 6.3*), with a slope that was found to be equal to  $9.0 \pm 0.3$ .

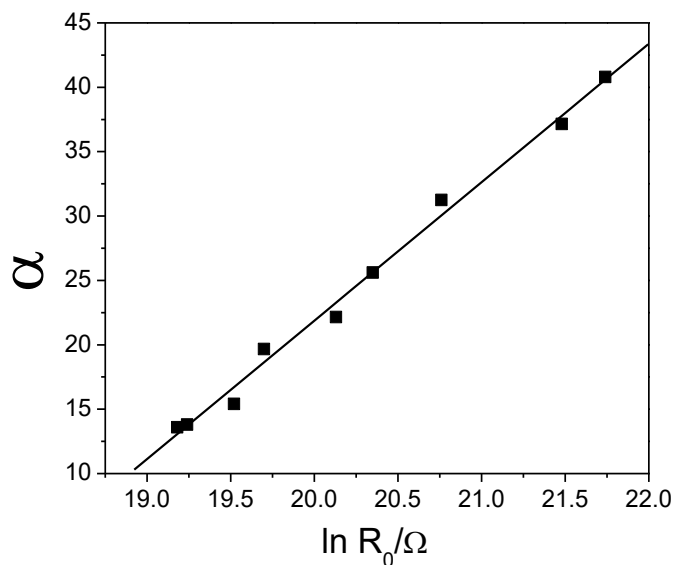


**Figure 6.3:** Indicative of the formation of Au-BPDI oligomers between nanoparticles, the values of  $\alpha$  scale linearly with  $\ln(R_o)$ . The slope of the plot for BPDI is  $9.0 \pm 0.3$

In *Figure 6.4*, the resistance variation with temperature for films of TPDI-linked gold nanoparticles also shows a linear variation of  $\ln R$  with  $T^{-1/2}$ , and this variation is also consistent with the Abeles model, which indicates the formation of  $-(\text{Au}-\text{TPDI})_n-$  oligomer chains between gold nanoparticles. The slopes of the plots of  $\ln(R)$  versus  $T^{-1/2}$  were obtained for TPDI-linked gold nanoparticles films with a wide range of initial conductivities, and the slope of this plot is equal to  $10.8 \pm 0.4$  (*Figure 6.5*).



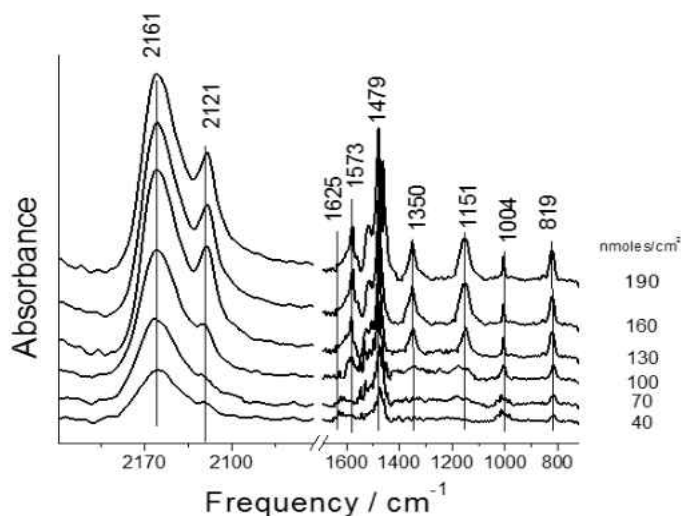
**Figure 6.4:** The linear  $\ln(R)$  versus  $T^{-1/2}$  dependence for a sample with initial conductivity of 4.5 nS dosed with  $0.15 \mu\text{mole}/\text{cm}^2$  BPDI, is predicted by the model of Abeles and Sheng.  $R_o$  is the sheet resistance of the film prior to dosing



**Figure 6.5:** Indicative of the formation of Au-TPDI oligomers between nanoparticles, the values of  $\alpha$  scale linearly with  $\ln(R_o)$ . The slope of the plot for TPDI is  $10.8 \pm 0.4$

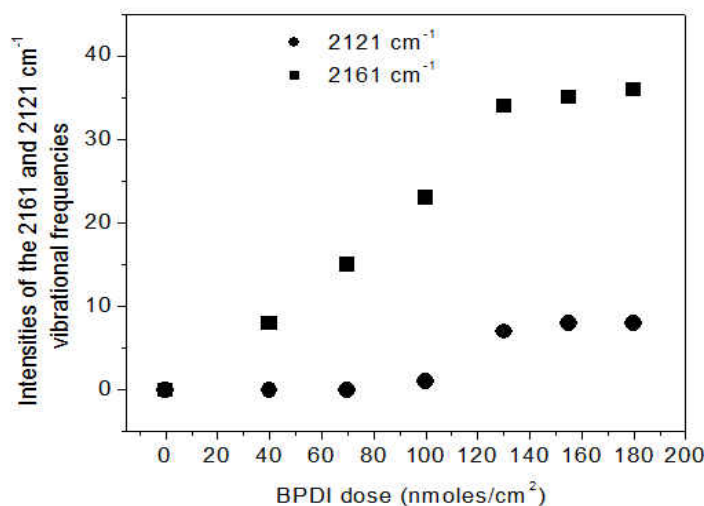
### 6.3.2 Attenuated total internal reflection infrared spectroscopy (ATR-IR) characteristics

Figure 6.6 shows a series of ATR-IR spectra of a gold film dosed sequentially with solutions of BPDI in benzene as a function of BPDI solution dose in  $\text{nmol}/\text{cm}^2$ , where the BPDI doses are indicated adjacent to the corresponding spectrum. Initial BPDI exposure gives rise to a single feature centered at  $\sim 2161 \text{ cm}^{-1}$  in the  $\text{C}\equiv\text{N}$  stretching region. After dosing with 130  $\text{nmol}/\text{cm}^2$  of BPDI solution, a sharper peak appeared at  $\sim 2121 \text{ cm}^{-1}$  which increase in intensity with the addition of BPDI. These  $\text{C}\equiv\text{N}$  vibration frequencies are in reasonable agreement with the results from previous work on 1,4-PDI on gold films (*Chapter 4*, [2]) that suggested that the molecules adsorb perpendicularly to the surface with the free isocyanide group exhibiting a vibrational frequency of  $2120 \text{ cm}^{-1}$ . After dosing more than 100  $\text{nmol}/\text{cm}^2$  of BPDI, the spectrum is thus indicative of the formation of a vertical BPDI species since it clearly exhibits a free isocyanide mode at  $\sim 2121 \text{ cm}^{-1}$ .



**Figure 6.6:** A series of ATR infrared spectra of BPDI adsorbed on a thin gold film using aliquots of 0.005 mM BPDI. The resulting BPDI doses, in  $\text{nmol}/\text{cm}^2$ , are indicated adjacent to the corresponding spectrum.

Figure 6.7 plots the variation in intensities of the 2161 and 2121  $\text{cm}^{-1}$  vibrational frequencies as a function of BPDI dose (in  $\text{nmol}/\text{cm}^2$ ). The intensity of the 2161  $\text{cm}^{-1}$  mode increases with dose up to  $\sim 130 \text{ nmol}/\text{cm}^2$  and then saturates. The 2121  $\text{cm}^{-1}$  feature starts to grow at doses of  $\sim 100 \text{ nmol}/\text{cm}^2$  indicating the formation of species in which the BPDI coordinates via a single  $\text{C}\equiv\text{N}$ , in good agreement with the dose at which the conductivity reaches its maxima value and starts to decrease (Figure 6.1a). Similar behavior was seen for 1,4-PDI (Chapter 4), indicating to a transition from flat-laying to perpendicular geometry.



**Figure 6.7:** The variation in intensities of the 2161 and 2121  $\text{cm}^{-1}$  vibrational frequencies as a function of BPDI dose (in  $\text{nmol}/\text{cm}^2$ ).

This conclusion is confirmed by spectral changes in the region between 700 and 1700  $\text{cm}^{-1}$  (Figure 6.6). At low exposures (40 and 70  $\text{nmol}/\text{cm}^2$ ), where only a single isocyanide mode is evident, the spectrum consists of peaks at 1623, 1465 and 819  $\text{cm}^{-1}$ , with a multiplet feature with



discernible peak at 975, 1010 and 1030  $\text{cm}^{-1}$ . The frequencies of these peaks are summarized in *Table 6.1*.

The peak intensities increase and additional peaks appear as the BPDI dose increases corresponding to the appearance of the 2121  $\text{cm}^{-1}$  isocyanide mode, consistent with the change in BPDI geometry. Peaks grow at 1573  $\text{cm}^{-1}$  where the  $\sim 1610 \text{ cm}^{-1}$  is evident as a shoulder. Additional peaks appear at  $\sim 1510$ , 1350 and 1151  $\text{cm}^{-1}$  and the multiplet peak at  $\sim 1000 \text{ cm}^{-1}$  at low doses collapses into the 1004  $\text{cm}^{-1}$  peak. Frequencies of these features are also summarized in *Table 6.1*.

The symmetry of biphenyl species depends on the angle  $\theta$  between aryl rings, having a  $D_{2h}$  point group when they are parallel,  $D_{2d}$  when  $\theta = \theta^0$  and  $D_2$  when  $\theta < \theta^0 < 90^0$ . Note that biphenyl has  $D_{2h}$  symmetry in the solid and a constrained BPDI bonding parallel to the surface is expected to have  $D_{2h}$  symmetry. In this case, only normal modes of  $B_{1u}$ ,  $B_{2u}$  and  $B_{3u}$  symmetry are allowed. Removing a mirror plane by adsorbing BPDI parallel to the surface, the postulated structure at low doses, reduces the symmetry to  $C_{2v}$ , so that only modes of  $B_{3u}$  symmetry in the free, planar biphenyl group will be detected in ATR-IR.

The frequencies of solid biphenyl groups, their intensities and reducible representations are also displayed in *Table 6.1*, where the modes of  $B_{3u}$  symmetry are indicated by an asterisk. They are the features that appear at lower doses, consistent with the biphenyl ring laying parallel to the surface. The exception is the 819  $\text{cm}^{-1}$  mode. However, in para-disubstituted benzene, the wagging mode of two adjacent hydrogens appears at a characteristic frequency of  $817 \pm 13 \text{ cm}^{-1}$ , consistent with this frequency.

70 nmoles/cm <sup>2</sup>	190 nmoles/cm <sup>2</sup>	Biphenyl frequencies	Assignment
819	819	-	-
975	-	985 <sub>(w)</sub>	B <sub>3u</sub> *
1010	1004	1006 <sub>(s)</sub>	B <sub>3u</sub> *
1030	-	1041 <sub>(s)</sub>	B <sub>3u</sub> *
-	1151	1169 <sub>(s)</sub>	B <sub>2u</sub>
-	1350	1344 <sub>(m)</sub>	B <sub>2u</sub>
1465	1465	1480 <sub>(vs)</sub>	B <sub>3u</sub> *
-	1510	-	-
-	1573	1568 <sub>(s)</sub>	B <sub>2u</sub>
1610	-	1597 <sub>(s)</sub>	B <sub>3u</sub> *

**Table 6.1:** Vibrational frequencies and assignments of BPDI on gold

At higher doses, the orientation of the BPDI is proposed to change, in principle, allowing B<sub>1u</sub> and B<sub>2u</sub> modes to become infrared allowed. Reference to *Table 6.1* indicates that the additional frequencies that appear at higher doses are due to modes with B<sub>2u</sub> symmetry consistent with this interpretation.

Analogous spectra are shown in *Figure 6.8* for TPDI on gold as a function of dose in (nmoles/cm<sup>2</sup>). Low coverages of TPDI (~90 nanomoles/cm<sup>2</sup>) on gold show one isocyanide band at 2167 cm<sup>-1</sup> consistent with a bound C≡N group. Similarly to 1,4-PDI and BPDI molecules, the unbound C≡N band appeared at ~ 2122 cm<sup>-1</sup> after dosing ~120 nanomoles of TPDI, where the coverage is high enough so the C≡N group is bound in an η<sup>1</sup> coordination mode to gold. All infrared frequencies obtained for TPDI are summarized in *Table 6.2*.

Similarly to BPDI, *Figure 6.8* show a variation in intensities of the 2167 and 2122 cm<sup>-1</sup> vibrational frequencies as a function of TPDI dose (in nmoles/cm<sup>2</sup>). The intensity of the 2167 cm<sup>-1</sup> mode increases with dose up to ~120 nmoles/cm<sup>2</sup> and then saturates. At larger doses, the 2122 cm<sup>-1</sup> feature grows indicating that the flat-laying species coordinate to two C≡N groups saturates

at this dose, in good agreement with the dose at which the conductivity reaches its maxima value (Figure 6.1b).

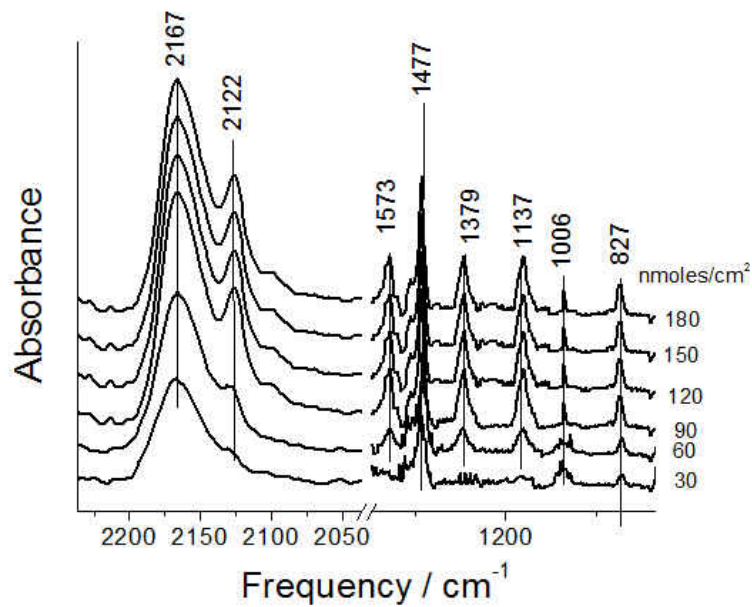


**Figure 6.8:** A series of ATR infrared spectra of TPDI adsorbed on a thin gold film using aliquots of 0.005 mM TPDI. The resulting TPDI doses, in nmole/cm<sup>2</sup>, are indicated adjacent to the corresponding spectrum.

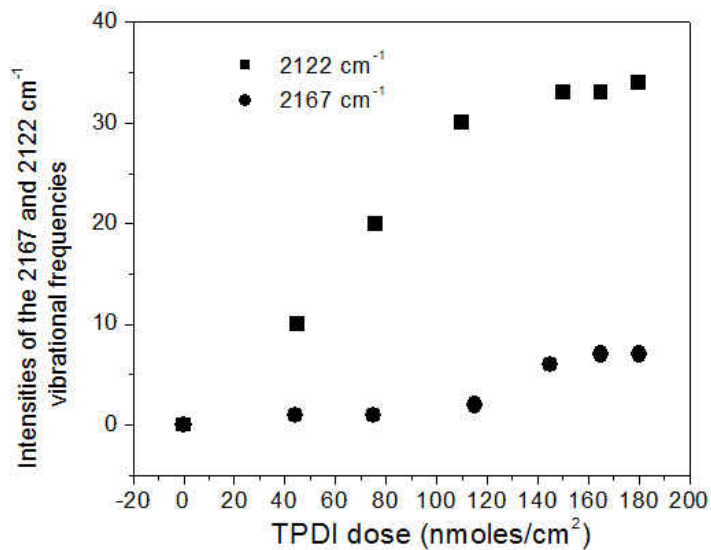


**Figure 6.9:** The variation in intensities of the 2167 and 2122  $\text{cm}^{-1}$  vibrational frequencies as a function of TPDI dose (in  $\text{nmoles/cm}^2$ ).

As shown in *Figure 6.8*, at low exposures (30 and 60  $\text{nmoles/cm}^2$ ), where only a single isocyanide mode is evident, the features appearing from 700-1700  $\text{cm}^{-1}$  are summarized in *Table 2*. TPDI also has a  $D_{2h}$  symmetry where modes of  $B_{1u}$ ,  $B_{2u}$  and  $B_{3u}$  are infrared allowed. At low doses, only  $B_{3u}$  symmetry modes in the terphenyl group will be detected, while at higher doses, the orientation of TPDI changes and becomes perpendicular to the surface allowing  $B_{1u}$ ,  $B_{2u}$  to appear.

30 nmoles/cm <sup>2</sup>	180 nmoles/cm <sup>2</sup>	Assignment
827	827	-
1006	1006	B <sub>3u</sub> *
-	1137	B <sub>3u</sub> *
-	-	
-	1379	B <sub>2u</sub>
1477	1477	B <sub>3u</sub> *
-	1573	B <sub>2u</sub>

**Table 6.2.** Vibrational frequencies and assignments of TPDI on gold

## 6.4 Discussion

Similarly to 1,4-PDI chemistry, the infrared results suggest that BPDI and TPDI on a gold film initially adsorbs with the diisocyanide plane parallel to the surface with symmetrically equivalent isocyanide vibrational modes, consistent with the formation of  $-(\text{Au}-\text{BPDI})-$  and  $-(\text{Au}-\text{TPDI})-$  oligomer chains, but then changes orientation at higher exposures to exhibit a free isocyanide frequency, consistent with a decoordinated species. The ligand spectrum on gold is in good agreement with RAIR spectra for BPDI and TPDI on gold that showed two frequencies for two different C≡N stretching frequencies, one for the coordinated end for the isocyanide, and one for the free end [2-8]. The coordinated C≡N end appears at higher frequency due to the strong polarization of lone pair electron density into the metal, since the lone pair density is antibonding with respect to the C≡N bond [7]. The presence of a single mode at 2161 cm<sup>-1</sup> for BPDI, and 2166 cm<sup>-1</sup> for TPDI is consistent with the formation of oligomer chains, but then changes orientation at higher exposures to exhibit a free isocyanide frequency, consistent with a decoordinated species.

Conductivity measurements as a function of BPDI dose from solution are shown in *Figure 6.1a*. The initial conductivity of the nanoparticle array before dosing BPDI was ~0.4 nS. After dosing 0.005 mM BPDI aliquots the conductivity increased gradually and reached ~22 nS as a

maximum measured value after dosing ~90 nmoles of BPDI solution. At higher doses the conductivity started to decrease slightly. Similarly, dosing TPDI aliquots increased the conductivity to the maximum value of ~22 nS, before it started to decrease slightly at higher coverages.

These results are in a good agreement with the ATR infrared spectra of BPDI adsorbed on a thin gold film using aliquots of 0.005 mM BPDI; a single mode at  $2161\text{ cm}^{-1}$  appeared in the first two doses of BPDI solution on the ZnSe crystal covered with a thin gold film, where this mode corresponds to coordinated  $\text{C}\equiv\text{N}$ , while after dosing 100 nmoles, a new peak appears at  $2121\text{ cm}^{-1}$ , which is due to a free isocyanide mode, and this corresponds to the highest conductivity value measured after dosing ~90 nmoles BPDI solution. After this point, BPDI molecules start to self-assemble perpendicularly to the surface, and the conductivity decreases slightly. TPDI showed the same behavior, where the bound  $\text{C}\equiv\text{N}$  group appeared at  $2166\text{ cm}^{-1}$ , which is slightly higher frequency than the  $\text{C}\equiv\text{N}$  band of BPDI on gold. After dosing ~150 nanomoles of TPDI, the unbound  $\text{C}\equiv\text{N}$  group appeared at  $2122\text{ cm}^{-1}$ . However, the decrease in conductivity as the vertical species form is less than found for PDI, where a considerable decrease in conductivity was found (*Chapter 4*). This may be due to a greater extent of tunneling between adjacent aryl rings in BPDI and TPDI than in PDI.

Electrical measurements were performed for 20 different samples with a range of different initial gold nanoparticle coverages. The samples were prepared in the vacuum evaporator as described in *Chapter 2*. 4.0 mM BPDI/benzene and a 4.0 mM TPDI/benzene solutions were used to dose the samples. The samples were cooled using liquid nitrogen, and *I-V* curves obtained at different temperatures. The plot of  $\alpha$  versus  $\ln(R_0/\Omega)$  was obtained and the height of the electron tunneling barrier was calculated using the Abeles model for thermally assisted tunneling through

granular materials [9]. From the measured  $\alpha$  values, it was possible to calculate the tunneling barriers for both molecules, where they are found to exhibit increasing barrier heights as the number of benzene rings increases; the data indicate that the slope of a plot of  $\alpha$  versus  $\ln(R_o/\Omega)$ , which increases with the height of tunneling barrier after dosing with BPDI molecules is  $9.0 \pm 0.3$ . The slope of the plot for TPDI-linked gold nanoparticles is slightly higher ( $10.8 \pm 0.4$ ), which indicates that the tunneling barrier is also higher. The calculated tunneling barrier showed a smallest value of  $0.10 \pm 0.02$  eV after dosing with 1,4-PDI (*Chapter 3*). The isocyanide groups have  $\pi$  orbitals that interact significantly with the  $\pi$  system of the phenyl rings. As the number of phenyl rings increases and the highest occupied  $\pi$  orbitals associated with the phenyl rings increases, the  $\pi$  orbitals of isocyanide groups are also influenced and increased in energy [10]. This effect is observed by comparing the IR spectra of PDI, BPDI, and TPDI molecules on gold surface. For BPDI molecules,  $\nu(\text{C}\equiv\text{N})$  bands for the isocyanide attached to the gold surface are observed at  $2162\text{ cm}^{-1}$ , which is a higher frequency than  $\nu(\text{C}\equiv\text{N})$  bands observed for PDI molecules ( $2158\text{ cm}^{-1}$ ). TPDI molecules showed the highest value for  $\nu(\text{C}\equiv\text{N})$  bands for the isocyanide attached to the gold surface ( $2166\text{ cm}^{-1}$ ). The overall increase in  $\nu(\text{C}\equiv\text{N})$  frequencies for isocyanides attached to gold is generally interpreted as an evidence of increased donation of electronic charge from the isocyanide to the gold [11]. Increasing the number of phenyl rings increases the electron donation to the gold, and this causes an increase in  $\nu(\text{C}\equiv\text{N})$  frequencies. The increased electron donation to the gold film leaves a partial positive charge on the isocyanide molecule. This partial positive charge leads to lowering the molecular orbital energies, which moves the HOMO orbital away from the Fermi level [11].

An alternative explanation for higher tunneling barrier may be a loss of planarity of the biphenyl and terphenyl linkers that increase the  $\pi$ -overlap between adjacent rings, causing the barrier to increase.

## 6.5 Conclusion

The conductive behavior of BPDI and TPDI are very similar to what found for PDI. Similar to 1,4-PDI-dosed nanoparticle array, the conductive path was interrupted after higher exposures of BPDI and TPDI solution, where the conductivity slightly decreased due to the de-coordination of BPDI and TPDI molecules, see *Figure 1*.

The sheet resistance  $R$  varies with temperature as  $\ln(R)$  versus  $1/\sqrt{T}$  (*Figure 2*), similar to the behavior found previously for 1,4-PDI. As an indication of the formation of Au-BPDI and Au-TPDI oligomers between nanoparticles, the values of  $\alpha$  scales linearly with  $\ln(R_o)$  as shown in *Figure 3*, and the data showed that BPDI-linked gold nanoparticle have a lower barrier than TPDI-linked gold nanoparticles, based on  $\alpha$  values.

The infrared spectra of BPDI and TPDI adsorbed on gold films display a single isocyanide stretching mode at low solution exposures, consistent with the presence of  $-(\text{Au-BPDI})-$  and  $-(\text{Au-TPDI})-$  oligomer chains. Higher BPDI and TPDI doses cause the isocyanide mode to split into two features, one of which is due to a free isocyanide, consistent with a vertically bonded species bound to the surface by one isocyanide group. The spectra of the ring modes are consistent with this conclusion. This behavior was observed after adsorbing 1,4-PDI on gold nanoparticle array [2].



## References

- [1] Kestell, J.; Abuflaha, R.; Boscoboinik, J.; Bai, Y.; Bennett, D.; Tysoe, W.T.; *Chem. Comm.* 2012, *49*, 1422-4.
- [2] Abuflaha, R.; Olson, D.; Bennett, D. W.; Tysoe, W. T.; *Surface Science*. **2016**, *649*, 56–59
- [3] Robertson, M. J.; Angelici, R. J.; *Langmuir* **1994**, *10*, 1488-1492
- [4] Swanson, S. A.; McClain, R.; Lovejoy, K. S.; Alamdari, N. B.; Hamilton, J. S.; Scott, J. C.; *Langmuir* **2005**, *21*, 5034-5039
- [5] Henderson, J. I.; Feng, S.; Bein, T.; Kubiak, C. P.; *Langmuir* **2000**, *16*, 6183-6187
- [6] Jagtap, S.; Kaji, Y.; Fukuoka, A.; Hara, K.; *Chem. Commun.*, **2014**, *50*, 5046—5048
- [7] Murphy, K.; Tysoe W. T.; Bennett, D. W.; *Langmuir* **2004**, *20*, 1732-1738
- [8] Robertson, M. J.; Anlelici, R. J. *Langmuir*, **1994**, *10*, 1488
- [9] Abeles, B.; Sheng, P.; Coutts, M. D.; Arie, Y. *Advances in Physics* **1975**, *24*, 407.
- [10] Hong, S.; Reifenberger, R.; *Superlattices and Microstructures*, **2000**, *28*, No. 4
- [11] Henderson, J. I.; Feng, S.; Bein, T.; Kubiak, C. T.; *Langmuir*, **2000**, *16*, 6183

## Chapter 7

# Surface Chemistry and Electron Transport of 4,4'-Biphenyldithiol and 4,4''-Terphenyldithiol on Gold Films From Solution

### 7.1 Introduction

Different characteristics can be used to investigate the rate of charge tunneling through organic molecules self-assembled between metal electrodes; different studies have investigated the structure of SAMs containing n-alkyl groups and the rate of charge tunneling in junctions [1-3], it was found that the length of the insulating  $-(CH_2)_n-$  group, which presents a high tunneling barrier, largely controls the rate of charge transport [4]. On the other hand, the relationship between the structure of polyaromatics (molecules that result in a reduction in the height of the tunneling barrier relative to that characterizing aliphatics) and the rate of charge transport was examined [5], and the influence of the chemical structure of the anchoring group that is bonded to the phenyl ring has been explored [6].

As demonstrated in previous chapters, after performing electrical measurements for PDI, BPDI and TPDI molecules, it was found that the tunneling barrier for diisocyanide molecules increased with increasing number of phenyl rings. The isocyanide groups have  $\pi$  orbitals that interact significantly with the  $\pi$  system of the phenyl rings. One possible explanation of this effect is that, as the number of phenyl rings increases and the highest occupied  $\pi$  orbitals associated with the phenyl rings increases, the  $\pi$  orbitals of isocyanide groups are also influenced and increased in energy. An alternative possibility is that the twist of aryl rings with respect to each other increases the tunneling barrier.

Because of important early measurements, *p*-benzene dithiol (BDT) has become a prototypical case for examining transport in such junctions. Thiolated molecules on gold surfaces comprise the majority of studied devices [6-8]. These junctions are relatively stable for reasonable measurement times and are more likely to be formed reproducibly because of the strong Au-S bond [7]. This chapter reports the influence of number of phenyl rings in aromatic dithiols on modulating the height of the tunneling barrier between the gold Fermi level and the energy levels of the organic thiol-terminated linker. In the same way as for the aromatic diisocyanide (*Chapter 3*) and 1,4-BDT (*Chapter 5*) molecules investigated previously, electrical measurements through biphenyl dithiols, 4,4'-biphenyldithiol (BPDT) and terphenyl dithiols, 4,4''-terphenyldithiol (TPDT) dosed onto gold nanoparticle array were made. It was shown in *Chapter 6* that biphenyl and terphenyl isocyanides could bridge between gold nanoparticles and this chapter explores whether linkages can also form with analogous dithiols.

To measure the structure of BPDT and TPDT, attenuated total internal reflection infrared spectroscopy (ATR-IR) was used to characterize the molecules on a gold film. The infrared results showed that the S-H rocking and stretching modes disappear after adsorbing on a gold film, thereby confirming the formation of Au-S bonds, consistent with the presence of oligomer chains.

## 7.2 Experimental

The conductivity of BPDT and TPDT on gold nanoparticle-covered mica was measured as described in details in previous chapters. Briefly, after gold electrodes were fabricated, gold nanoparticle arrays were deposited to some initial resistance and the film was left to age until there was no further change in the sheet resistance (*Figure 3.1, Chapter 3*). A series of samples with different initial resistance values were prepared and dosed with 0.1 mM BPDT and 0.1 mM TPDT

solutions. Electrical measurements were made in a HV chamber, where the temperature was monitored by means of a chromel-alumel thermocouple attached to the sample, and the  $I/V$  characteristics were measured by applying a voltage *via* a D/A converter and the resulting current measured by means of a picoammeter that was monitored by an A/D converter to yield  $I/V$  curves directly.

The concentration dependence experiments were performed by preparing a sample with an initial conductivity of  $\sim 0.5$  nS, and the sample was dosed with 30  $\mu\text{L}$  aliquots of 0.01 mM BPDT and 0.01 mM TPDT solutions in benzene using an Eppendorf pipette on the surface of the nanoparticle-covered sample until all of the solvent had evaporated. The sample was then rinsed with benzene to remove any remaining weakly bound dithiols and allowed to dry in air. The conductivity was measured under vacuum at a base pressure of  $\sim 2 \times 10^{-8}$  Torr, then the sample was taken out the chamber, dosed again with 30  $\mu\text{L}$  aliquots of 0.01 mM solutions, and again the unbonded particles were washed away with pure benzene, and a new conductivity was measured under vacuum. The same process was repeated several times until the sample was saturated and there was no further change in conductivity.

Infrared spectra of BPDT and TPDT on gold films were also collected by evaporating gold onto a zinc selenide ATR plate with an  $\sim 8$   $\text{cm}^2$  area, and the infrared spectra collected using a Bruker Vertex infrared spectrometer operating at a resolution of  $4$   $\text{cm}^{-1}$ , typically for 2000 scans using a DTGS detector. The gold film thickness was selected to allow reasonable infrared transmission through the sample to be obtained and spectra were collected after dosing with 200  $\mu\text{L}$  aliquots of a 0.1 mM dithiol solutions in benzene. The sample was allowed to dry in air and then rinsed with benzene to remove any residual, weakly bound molecules.

## 7.3 Results

### 7.3.1 Electrical Measurements

The conductive properties of gold nanoparticles deposited onto a mica substrate exposed to aliquots of 0.05 mM BPDT solutions in benzene are summarized in *Figure 7.1a*. The initial resistance value of the sample before dosing BPDT was  $\sim 200\text{ M}\Omega$ . The resistance of the sample decreased substantially as the BPDT concentration was increasing to reach a minimum value of  $\sim 1.8\text{ M}\Omega$  ( $\sim 550\text{ nS}$ ). *Figure 7.1b* represents the conductive properties of a gold nanoparticle array exposed to aliquots of 0.05 mM TPDT solutions in benzene. Before dosing with TPDI molecules, the initial resistance was  $\sim 600\text{ M}\Omega$ , while a considerable decrease in resistance to  $\sim 2\text{ M}\Omega$  ( $480\text{ nS}$ ) as a minimum value was observed after dosing with  $\sim 80$  nanomoles of TPDT, and no change in resistance was observed at higher doses. In both cases, an induction period was observed in the conductivity plots as a function of dose.

It has been shown previously that the  $-(\text{Au}-\text{BDT})_n-$  oligomer chains are capable of bridging between gold nanoparticles deposited onto a mica surface and enhance the conductivity between gold electrodes, and a similar effect was observed when dosing a gold-nanoparticle covered mica surface with BPDT and TPDT molecules, which provides evidence for the formation of similar one-dimensional chains as found for 1,4-BDT. The resistance varied as a function of the temperature, and in *Figure 7.2*, typical temperature variations are plotted as  $\ln(R)$  versus  $T^{-1/2}$ , according to Abeles model for thermally assisted tunneling through an array of nanoparticles [9]. This linear behavior provides evidence that  $-(\text{Au}-\text{BPDT})_n-$  and  $-(\text{Au}-\text{TPDT})_n-$  oligomer chains are formed. Additional evidence for the formation of oligomeric bridges between particles is that the value of  $\alpha$  (derived from the slope of  $\ln(R)$  versus  $T^{-1/2}$  plots) varies linearly with  $\ln(R_0)$  as shown in *Figures 7.3 and 7.4*.

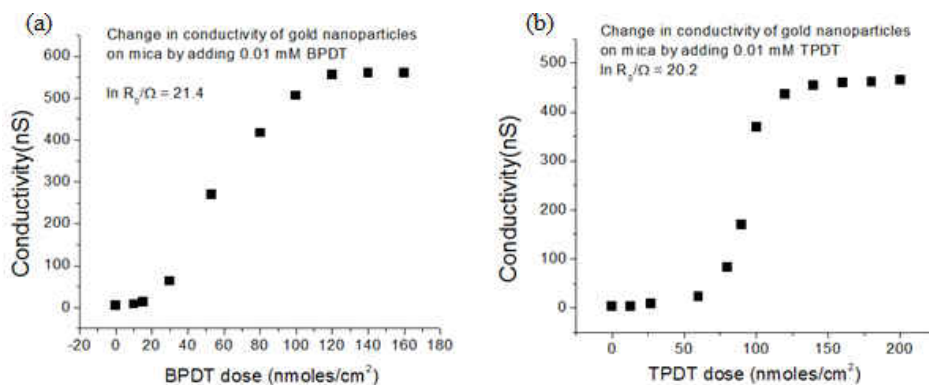


**Figure 7.1:** Plot of the conductivity of gold nanoparticles deposited onto a mica substrate (a) change in conductivity as a function of the BPDT solution dose in nmole/cm<sup>2</sup> for mica sample with initial resistance of ~200 MΩ dosed with 0.05 mM BPDT in benzene. (b) Change in conductivity as a function of the TPDT solution dose in nmole/cm<sup>2</sup> for mica sample with initial resistance of ~600 MΩ dosed with 0.05 mM TPDT in benzene.

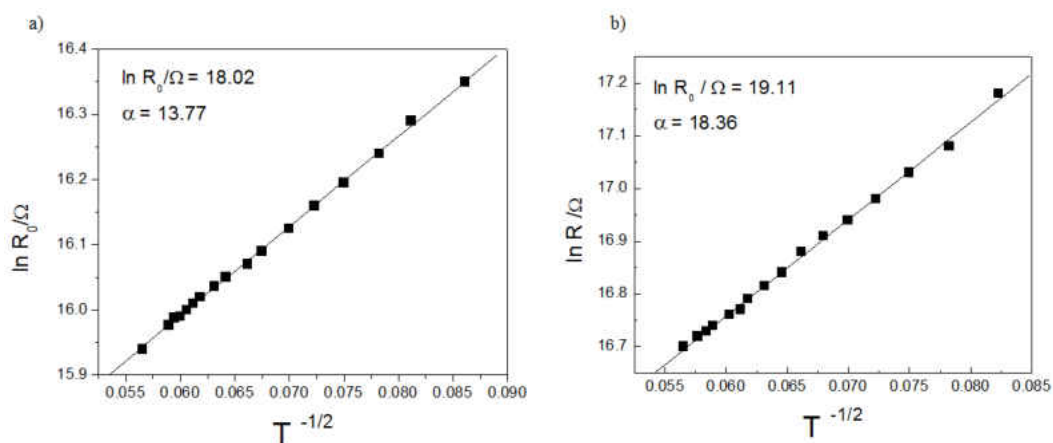


**Figure 7.2:** The linear  $\ln(R)$  versus  $T^{-1/2}$  dependence for two different samples is predicted by the model of Abeles and Sheng.  $R_0$  sheet resistance of the film prior to dosing, and scales with gold coverage. a) Gold nanoparticles with initial coverage of 15.00 nS linked with BPDT molecules and b) gold nanoparticles with initial coverage of 5.0 nS linked with TPDT

The slopes of the plots of  $\ln(R)$  versus  $T^{-1/2}$  for BPDT- and TPDT-linked gold nanoparticles were obtained for films spanning a wide range of initial (undosed) conductivities,  $R_o$ . The slopes of these plots ( $\alpha$ ) was found to vary linearly with  $\ln(R_o)$  (Figures 7.3 and 7.4). The slope for BPDT-linked gold nanoparticles was found to be  $8.3 \pm 0.4$  and for TPDT-linked gold nanoparticles  $11.4 \pm 0.4$ .

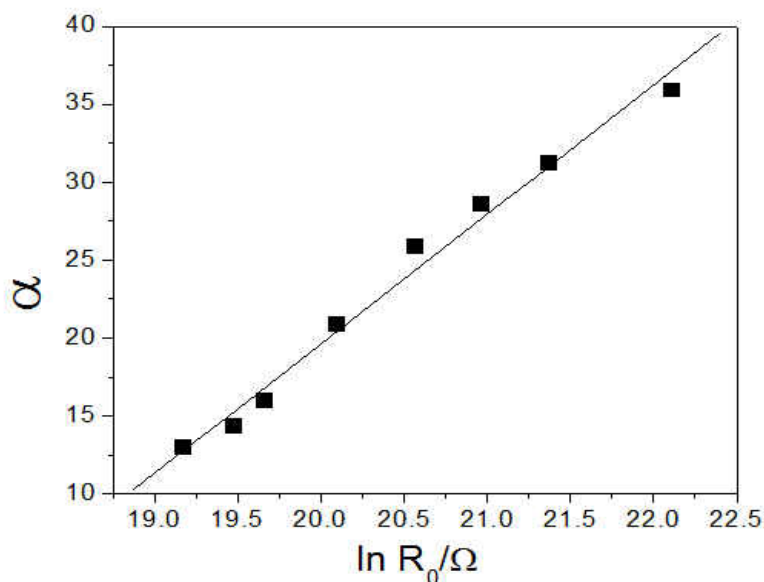


**Figure 7.3.** Indicative of the formation of Au-BPDT oligomers between nanoparticles, the values of  $\alpha$  scale linearly with  $\ln(R_o)$ . The slope of the plot for BPDT is  $8.3 \pm 0.4$

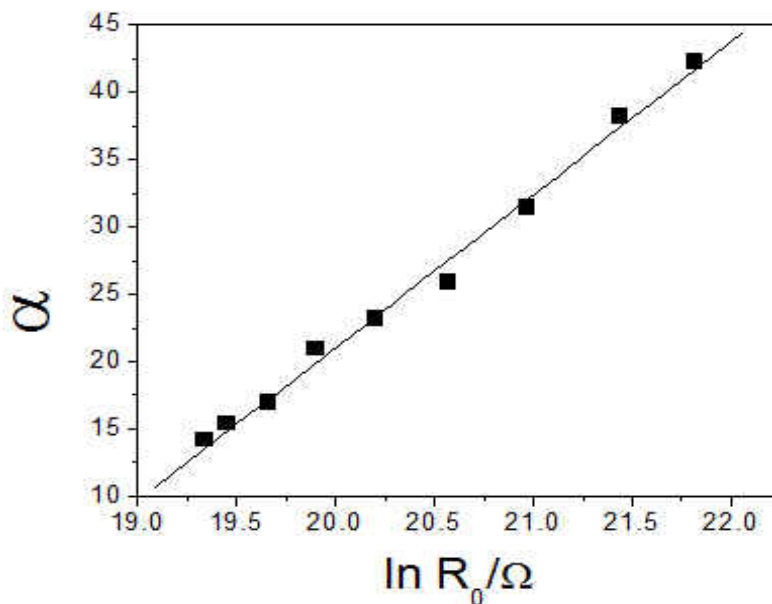


**Figure 7.4.** Indicative of the formation of Au-TPDT oligomers between nanoparticles, the values of  $\alpha$  scale linearly with  $\ln(R_o)$ . The slope of the plot for TPDT is  $11.4 \pm 0.4$

### 7.3.2 Attenuated total internal reflection infrared spectroscopy (ATR-IR) measurements

*Figures 7.5 and 7.6* show ATR-IR spectra for BPDT and TPDT respectively on gold film as a function of dithiol dose in moles/cm<sup>2</sup> of the crystal. The infrared spectra were collected after dosing a gold film-covered ZnSe crystal with 0.1 mM aliquots of BPDT (*Figure 7.5*) and TPDT (*Figure 7.6*), then allowing to dry in air for ~ 5 minutes and rinsing with benzene to remove any residual, weakly bonded molecules.



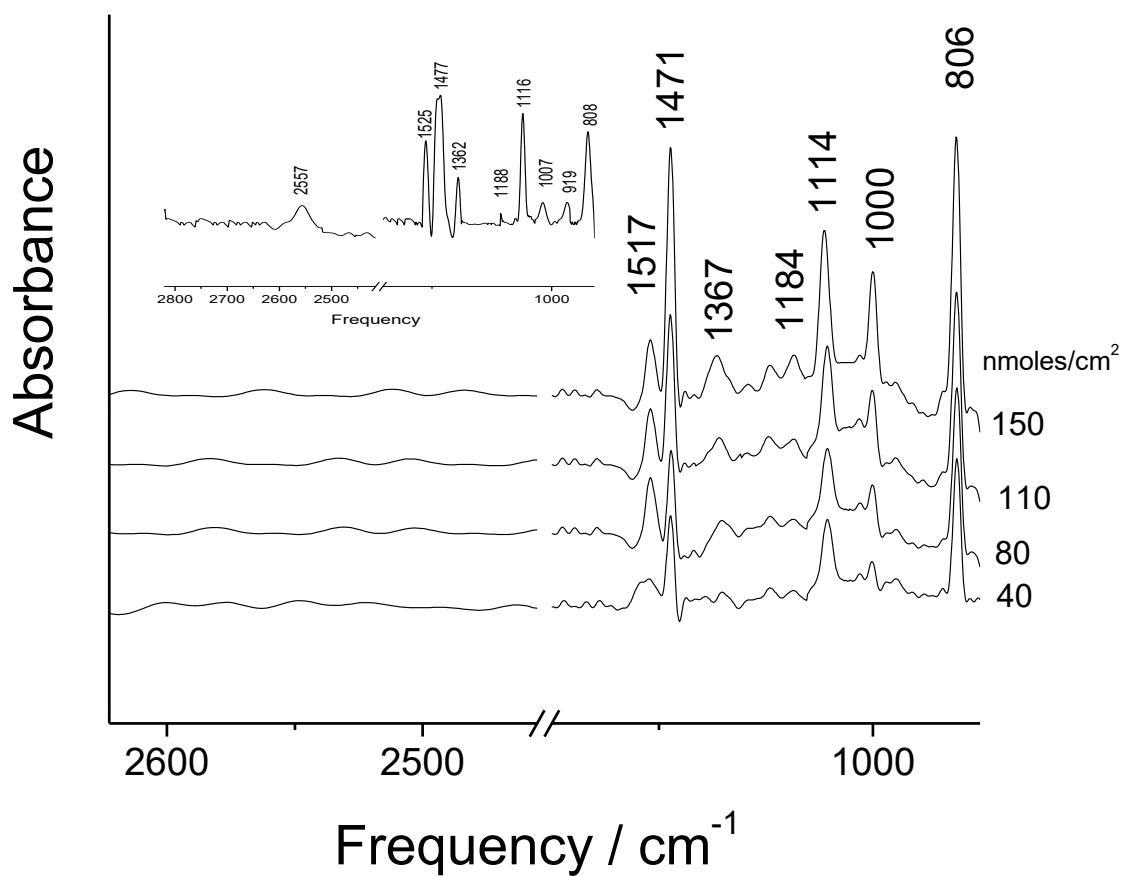


**Figure 7.5:** A series of ATR infrared spectra of BPDT adsorbed on a thin gold film using aliquots of 200  $\mu\text{l}$  of solution of 0.1 mM BPDT. The resulting BPDT doses, in  $\text{nmol}/\text{cm}^2$ , are indicated adjacent to the corresponding spectrum. The inset is a spectrum of 0.1 mM solution of pure BPDT in benzene.

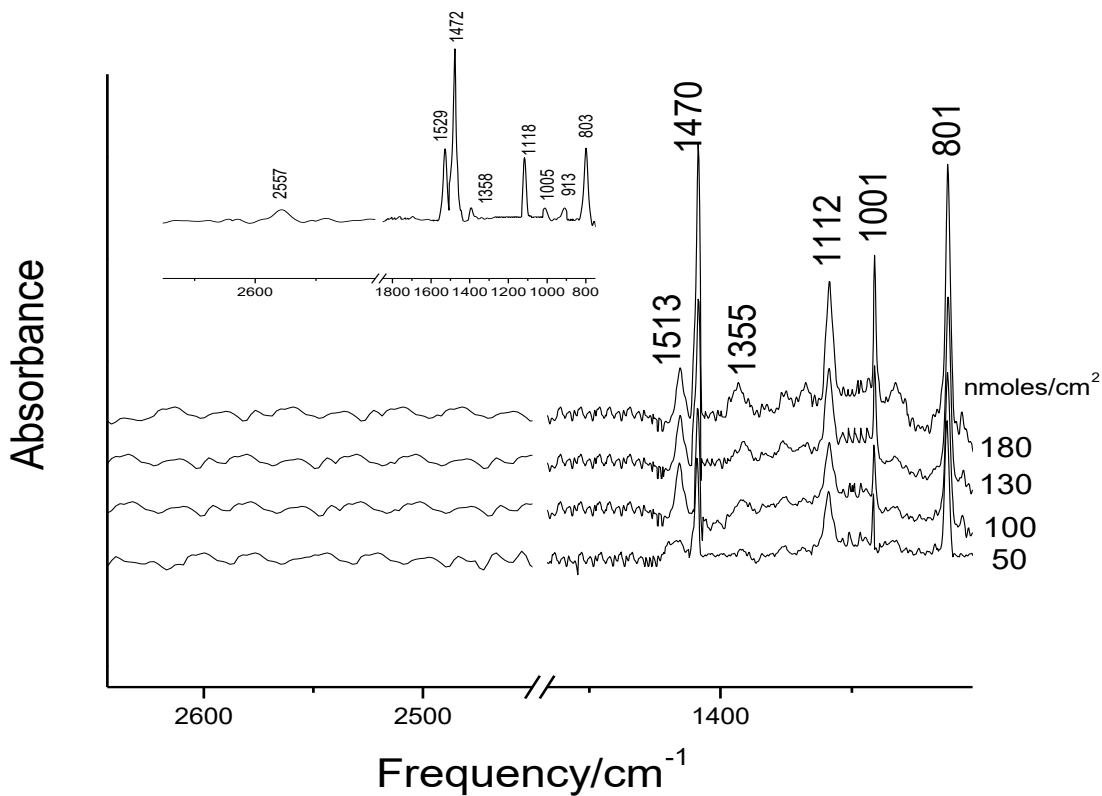


**Figure 7.6:** A series of ATR infrared spectra of TPDT adsorbed on a thin gold film using aliquots of 200  $\mu\text{l}$  of solution of 0.1 mM TPDT. The resulting TPDT doses, in mole/ $\text{cm}^2$ , are indicated adjacent to the corresponding spectrum. The inset is a spectrum of 0.1 mM solution of pure TPDT in benzene.

As demonstrated in *Chapter 6*, the symmetry of biphenyl and terphenyl species with the aryl ring lying parallel to the surface is  $C_{2v}$ , where the majority of the observed modes are due to aryl ring vibrations. As shown in the inset of *Figure 7.5*, for pure BPDT, S-H rocking vibrations are evident at  $\sim 919\text{ cm}^{-1}$  and a stretching mode appears as a broad band centered at  $\sim 2557\text{ cm}^{-1}$ .

The ring modes are still evident for dithiol-linked gold nanoparticle arrays. However, the most drastic changes are noted for the S–H bending and stretching modes, the absence of the  $\sim 919\text{ cm}^{-1}$  S–H rocking and S–H stretching mode at  $\sim 2557\text{ cm}^{-1}$  indicates the formation of a dithiolate species.

The ring modes are assigned in a similar manner as for BPDI (*Chapter 6, Table 6.1*), where only modes with  $B_{3u}$  symmetry (highlighted by asterisks) are expected to be infrared allowed for a biphenyl linker with the aryl rings lying parallel to the surface. The assignments are summarized for BPDT on gold in *Table 7.1*. In the case of BPDI, only modes of  $B_{3u}$  symmetry were detected at low coverages, consistent with the symmetry assignments above. However, a mode at  $1517\text{ cm}^{-1}$  is clearly evident that grows with increasing BPDT exposure (*Figure 7.5*). This implies that the biphenyl chain in BPDT no longer is parallel to the surface. Similar tilting of the phenyl group was found for 1,4-BDT on gold (*Chapter 5*), and ascribed to a ring tilt induced by the non-linear C-S-Au bond. A similar effect may occur here. In addition, this may indicate a lack of planarity of the biphenyl rings and indicate that they are twisted with respect to each other.

40 nmoles/cm <sup>2</sup>	150 nmoles/cm <sup>2</sup>	Biphenyl frequencies	Assignment
806	806	808	-
988	988	919	$B_{3u}^*$
1000	1000	1007	$B_{3u}^*$
1114	1114	1116	$B_{3u}^*$
1184	1184	1188	$B_{3u}^*$
-	1367	1362	$B_{2u}$
1471	1471	1477	$B_{3u}^*$
1517	1517	1525	$B_{2u}$

**Table 7.1:** Vibrational frequencies and assignments for BPDT on gold

Analogous spectra are shown in *Figure 7.6*, for TPDT on gold as a function of dose in (nmoles/cm<sup>2</sup>). Similarly to BPDT, S-H rocking vibrations are evident at  $\sim 913\text{ cm}^{-1}$  and stretching

modes appear as a broad band centered at  $\sim 2557 \text{ cm}^{-1}$  for the solution spectra. The ring modes are still evident for dithiol-linked gold nanoparticle arrays as shown in *Table 7.2*. However, drastic changes are noted for the S–H bending and stretching modes for TPDT on gold film, where the absence of the  $\sim 913 \text{ cm}^{-1}$  S–H rocking and S–H stretching mode at  $\sim 2557 \text{ cm}^{-1}$  indicates the formation of a dithiolate species.

Again, the ring modes can be assigned by comparison with the spectra of TPDI on gold (*Chapter 6, Table 6.2*) and are given in *Table 7.2*. Again, for flat-lying TPDT with the aryl ring parallel to the surface, only  $B_{3u}$  modes (highlighted by asterisks) should be infrared allowed, and are detected. However, modes with  $B_{2u}$  symmetry are also observed and this effect is also ascribed to a distortion of the terphenyl backbone due to the non-linear C-S-Au bonds, possibly resulting in twisting of the aryl rings with respect to each other.

50 nmoles/cm <sup>2</sup>	180 nmoles/cm <sup>2</sup>	Terphenyl frequencies	Assignment
801	801	803	-
1001	1001	1005	$B_{3u}^*$
1112	1112	1118	$B_{3u}^*$
1335	1335	1368	$B_{2u}$
1470	1470	1472	$B_{3u}^*$
1513	1513	1529	$B_{2u}$

**Table 7.2:** Vibrational frequencies and assignments for TPDT on gold

#### 7.4 Discussion

An increase in conductivity was found when gold nanoparticle arrays on mica were dosed with BPDT and TPDT (*Figure 7.1*). When a gold film with an initial resistance of  $\ln(R_o/\Omega) = 21.4$  was dosed 0.05 mM aliquots of BPDT, a slight increase in conductivity was observed after dosing  $\sim 20 \text{ nmoles/cm}^2$  of BPDT solution. The conductivity increased dramatically to  $\sim 520 \text{ nS}$  then

stabilized (*Figure 7.1a*). The same behavior was seen after dosing a gold film where  $\ln(R_o/\Omega) = 20.2$  with 0.05 mM TPDT aliquots, the conductivity increased slightly until after dosing  $\sim 55$  nmoles/cm<sup>2</sup> TPDT solution, then the conductivity increased dramatically and stabilized at  $\sim 420$  nS after dosing  $\sim 130$  nmoles/cm<sup>2</sup>.

In previous measurements of conductivity change with solution dose, the conductivity was observed to initially increase as the nanoparticle arrays were dosed. However, in the case of BPDT and TPDT, an initial dose of  $\sim 20$  nmoles/cm<sup>2</sup> of BPDT and  $\sim 60$  nmoles/cm<sup>2</sup> of TPDT were needed to induce an increase in conductivity. The origin of this induction period is not known, but appears not to be due to the longer backbone, since it was not observed for isocyanide terminated molecules (*Figure 6.1, Chapter 6*).

As shown in *Figure 7.2* the sheet resistance  $R$  varies with temperature as  $\ln(R)$  versus  $1/\sqrt{T}$ , similar to the behavior found previously for 1,4-BDT. As an indication of the formation of Au-BPDT and Au-TPDT oligomers between nanoparticles, the slope of these plots ( $\alpha$ ) scales linearly with  $\ln(R_o)$  and results were obtained for  $\sim 20$  samples (*Figures 7.2 and 7.3*). The data shows that the slope of the plot increases when increasing the number of phenyl groups. The slope is equal to  $8.3 \pm 0.4$  for BPDT-linked gold nanoparticle arrays. For TPDT-linked gold nanoparticles, the slope was found to be  $11.4 \pm 0.4$ . These value of  $\alpha$  increases with the tunneling barrier height, which implies that the height of tunneling barrier for BPDT-linked gold nanoparticles is lower than TPDT-linked gold nanoparticles.

According to the length of dithiol molecules (BDT, BPDT and TPDT), it is expected that longer molecules would conduct better than shorter ones, since more extensively conjugated molecules are generally expected to have a narrower HOMO-LUMO gap. As a result, the HOMO band should be closer to the Fermi energy of the metal electrode, thus, the conduction should be

higher for more conjugated dithiols (molecules with more benzene rings). However, slope values derived from plots for BDT, BPDT, and TPDT show that the height of the tunneling barrier increases with increasing the number of benzene rings, which means that increased extent of conjugation does not necessarily lead to higher current.

It is generally agreed that BDT is a hole type conductor and that the occupied orbitals responsible for the conduction have high amplitude on the sulfur atoms [5]. The extended aromatic dithiol compounds are  $\pi$  type conductors, whose thiol end groups contact gold electrodes similarly to BDT. However, in contrast to the planar BDT, in which the  $\pi$  electrons are delocalized over the entire molecule, the biphenyl and terphenyl molecules have a twisted ring configuration which appear to be observed for BPDT and TPDT as discussed above. This distortion decreases the conjugation by reducing the orbital overlap between the aromatic rings. Therefore, the poly-phenyl dithiol molecules are not expected to be as conductive as benzene dithiol.

## 7.5 Conclusion

Similar to 1,4-BDT-dosed nanoparticle array, the conductive path was not interrupted after higher exposures of BPDT and TPDT solutions and differs from the behavior of diisocyanides, where isocyanide decooordination at higher coverages caused a reduction in conductivity. These thiols adsorb by S-H bond scission, such decooordination is not possible with dithiols, resulting in a saturation in conductivity at higher solution doses. The sheet resistance  $R$  varies with temperature as  $\ln(R)$  versus  $1/\sqrt{T}$  (*Figure 7.2*), similar to the behavior found previously for 1,4-BDT. As an indication of the formation of Au-BPDT and Au-TPDT oligomers between nanoparticles, the values of  $\alpha$  scale linearly with  $\ln(R_o)$  are shown in *Figure 7.3*, and the data showed that BPDT-

linked gold nanoparticle have a lower tunneling barrier than TPDT-linked gold nanoparticles, based on  $\alpha$  slope values.

The infrared spectra of BPDT and TPDT adsorbed on gold films show that vibrational modes at  $\sim 2550\text{ cm}^{-1}$  and  $\sim 907\text{ cm}^{-1}$  are assigned to S-H stretching and rocking modes respectively disappear after adsorbing BPDT and TPDT molecules on gold, which confirms forming S-Au bond.

## References

- [1] Nijhuis, C. A.; Reus, W. F.; Barber, J. R.; Dickey, M. D.; Whitesides, G. M.; *Nano Lett.* **2010**, *10*, 3611–3619
- [2] Boulas, C.; Davidovits, J. V.; Rondelea, F.; Vuillaume, D.; *Physical Review, Letters.* **1996**, *76*, No 25
- [3] Song, H.; Lee, H.; Lee, T.; *J. AM. CHEM. SOC.* **2007**, *129*, 3806-3807.
- [4] Bowers, C. M.; Rappoport, D.; Baghbanzadeh, M.; Simeone, F. C.; Liao, C. K.; Semenov, S. N.; Žaba, T.; Cyganik, P.; Guzik, A. A.; Whitesides, G. M.; *J. Phys. Chem. C* **2016**, *120*, 11331–11337
- [5] Cohen, R., Stokbro, K.; Martin, J. M.; Ratner, M. A.; *J. Phys. Chem. C* **2007**, *111*, 14893-14902
- [6] Mishchenko, A.; Vonlanthen, D.; Meded, V.; Burkle, M.; Li, C.; Pobelov, I. V.; Bagrets, Viljas, J. K.; Pauly, F.; Evers, F.; Mayor, M.; Wandlowski, T.; *Nano Lett.* **2010**, *10*, 156-163
- [7] Wei, W.; Sun, Y.; Zhu, M.; Liu, X.; Sun, P.; Wang, F.; Gui, Q.; Meng, W.; Cao, Y.; Zha, J.; *J. Am. Chem. Soc.* **2015**, *137*, 15358–15361
- [8] Kestell, J.; Abuflaha, R.; Garvey, M.; Tysoe, W. T.; *Phys. Chem. C* **2015**, *119*, 23042–23051
- [9] Abeles, B.; Sheng, P.; Coutts, M. D.; Arie, Y. *Advances in Physics* **1975**, *24*, 407.

## Chapter 8

# Asymmetric Electron Linker Molecule and Conductivity Measurements of 4,4'-Disulfanediyldibenzoisonitrile on Gold Films from Solution

### 8.1 Introduction

In previous chapters, structures and electrical measurements were investigated for symmetric aromatic molecules that consist of one, two, and three benzene rings, terminated either with diisocyanide or dithiol groups. The results showed that these molecules generally form oligomer bridges when dosed on gold-nanoparticle arrays, and that the conductivity can be affected by the number of phenyl rings for each molecule. This raises the issue whether similar bridging can occur when the molecular linker contains different linking groups. Being able to achieve this will raise the possibility of making linkers that also have asymmetric electrical properties, such as molecular rectifiers. The obvious candidate for testing this idea is to use an asymmetric structure of BDT and PDI,  $\text{HS.C}_6\text{H}_4.\text{NC}$ . However, it is a synthetic challenge to specifically functionalize such molecules and instead we use 4,4'-disulfanediyldibenzoisonitrile ( $\text{NC-C}_6\text{H}_4\text{-S-S-C}_6\text{H}_4\text{-NC}$ ) (DBN) (*Figure 8.1*). In this case, the molecule is expected to adsorb onto gold by cleavage of the weak S-S bond to form thiolate species on the surface, analogous to the chemistry found for dithiols (*Chapters 5 and 7*). The formation of DBN SAMs on a gold-nanoparticle array has been investigated by electrical measurements and ATR-IR spectroscopy. Thereby it was found that DBN has ability to form oligomers between gold nanoparticles and contributes to tuning the gold Fermi level and decrease the height of the electron tunneling barrier.



ATR-IR spectra provide information that is complementary to the electrical measurements, and allow the surface structure of DBN molecules on the gold-nanoparticle array to be determined.

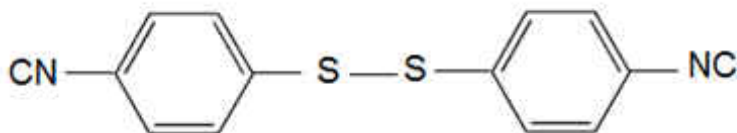


**Figure 8.1:** Structure of 4,4'-Disulfanediyldibenzoisonitrile (DBN)

## 8.2 Experimental

The conductivity of DBN on a nanoparticle array was measured as described in *Chapter 4*. Briefly, gold nanoparticles of  $\sim 8$  nm in diameter were deposited by evaporation onto a cleaved mica substrate. Gold electrodes were fabricated by masking the central portion of the mica substrate and depositing gold electrode pads  $\sim 200$  nm thick. The sample was dosed with DBN from solution after the gold-nanoparticle covered sample had been allowed to age until there was no further change in the sheet resistance, a process that was complete after  $\sim 2$  h, depending on the initial gold coverage. A droplet of DBN solution (0.1 mM in benzene) was placed on the surface of the nanoparticle-covered sample for 10 s, and the excess washed away using benzene.

Electrical measurements were made in a stainless-steel HV chamber that was pumped to a base pressure of  $\sim 2 \times 10^{-8}$  Torr without baking to avoid altering the sample during bakeout. The sample temperature was measured by means of a chromel–alumel thermocouple, and the current versus voltage ( $I/V$ ) characteristics were measured by applying a voltage via a D/A converter and the resulting current measured by means of a Keithly picoammeter that was monitored by an A/D converter to yield  $I/V$  curves directly.

Infrared spectra of isocyanothiol-linked gold films were also collected by evaporating gold onto a zinc selenide (ZnSe) ATR plate with an  $\sim 8 \text{ cm}^2$  area, and the infrared spectra collected for 2000 scans using a DTGS detector. The gold film thickness was selected to allow reasonable infrared transmission through the sample to be obtained and spectra were collected after dosing with 200  $\mu\text{l}$  aliquots of a 0.1 mM DBN solutions in benzene. The samples were allowed to dry in air for  $\sim 5$  minutes and then rinsed with benzene to remove any residual.

## 8.3 Results

### 8.3.1 Electrical studies

The conductive properties of gold nanoparticles deposited onto a mica substrate exposed to aliquots of 0.03 mM DBN solutions in benzene are summarized in *Figure 8.2*. In this case, the DBN dose was normalized to the total area of the nanoparticle array between the gold electrodes. The initial conductivity of the sample before dosing DBN was  $\sim 1.5 \text{ nS}$ . The conductivity of the sample increased substantially as the DBN concentration was increasing to reach a maximum value of  $\sim 155 \text{ nS}$ , after a DBN dose of  $\sim 180 \text{ nanomoles/cm}^2$ . At higher doses, the conductivity does not increase anymore, which means that the surface became saturated.

It has been shown previously that diisocyanide and dithiol oligomer chains are capable of bridging between gold nanoparticles deposited onto a mica surface and enhance the conductivity between gold electrodes. A similar effect was observed when dosing a gold-nanoparticle covered mica surface with DBN, which provides evidence for the formation of similar one-dimensional chains. The resistance varied as a function of the sample temperature and, in *Figure 8.3*, a typical resistance variation with temperature is plotted as  $\ln(R)$  versus  $T^{-1/2}$ . This variation is consistent with the Abeles model for thermally assisted tunneling through an array of nanoparticles [1]. This

linear behavior provides further evidence that DBN oligomer chains are formed between gold nanoparticles. The other evidence for the formation of oligomeric bridges between particles is that the value of  $\alpha$  (the slope of  $\ln(R)$  versus  $T^{-1/2}$  plots) varies linearly with  $\ln(R_o)$  as shown in *Figure 4*, where  $R_o$  is the initial resistance of the gold nanoparticle array before dosing.

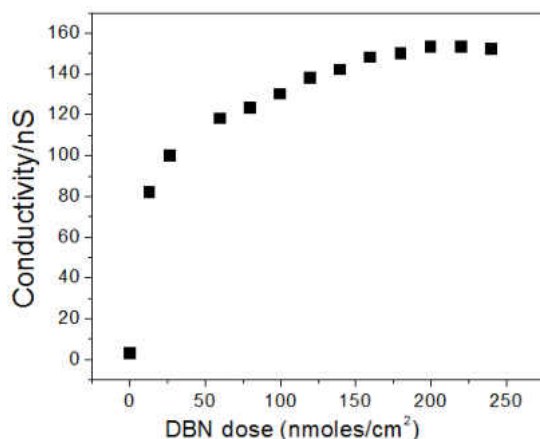


**Figure 8.2:** Variation in conductivity as a function of DBN dose in nmoles/cm<sup>2</sup> measured when dosing a gold-nanoparticle-covered mica surface with an initial sheet resistance  $R_o$  of  $\ln(R_o/\Omega) = 19.47$ , from solution

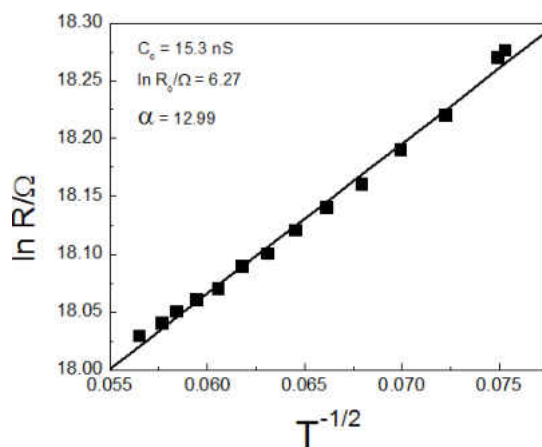


**Figure 8.3:** The linear  $\ln(R)$  versus  $T^{-1/2}$  dependence for a sample with initial conductivity of 15.3 nS dosed with 0.1  $\mu\text{mole}/\text{cm}^2$  BPDI, is predicted by the model of Abeles and Sheng.  $R_o$  is the sheet resistance of the film prior to dosing

The slope of the plots of  $\ln(R)$  versus  $T^{-1/2}$  were obtained for DBN-linked gold nanoparticles films spanning a wide range of initial (undosed) conductivities,  $R_0$ . The slopes of these plots ( $\alpha$ ) were found to vary linearly with  $\ln(R_0)$  (Figure 8.4), with a slope that was found to be equal to  $7.4 \pm 0.3$ .

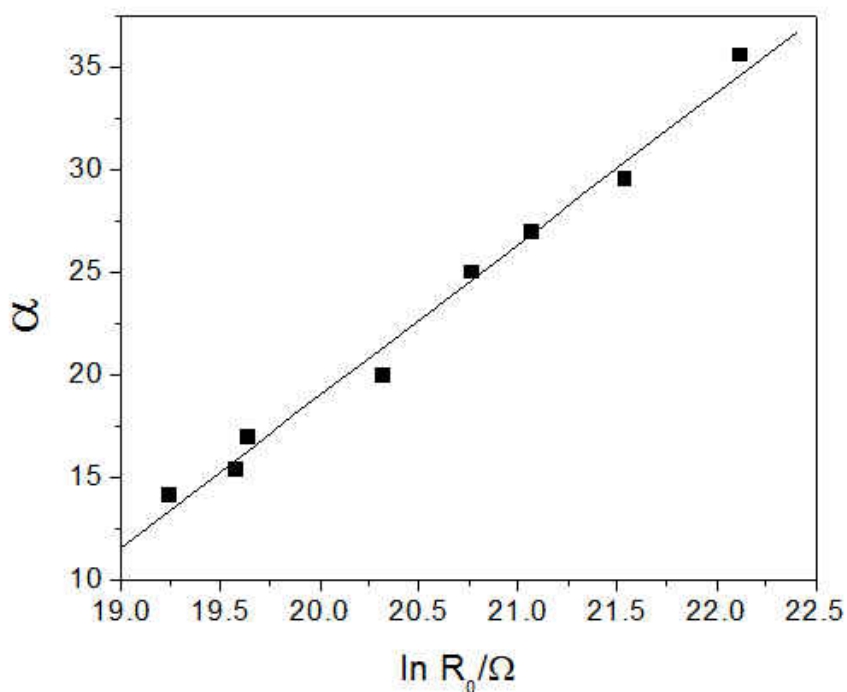


**Figure 8.4:** Plot of  $\alpha$  values versus  $\ln(R_0)$  for the 8 different films obtained for DBN-linked gold nanoparticles, with a slope of  $7.4 \pm 0.3$ . The linear fit is in agreement with the theory of activated tunneling in granular materials put forth by Abeles and Sheng

### 8.3.2 Attenuated total internal reflection infrared spectroscopy (ATR-IR) characteristics

Figure 8.5 shows ATR-IR spectra for DBN as a function of DBN dose onto a gold film in moles per  $\text{cm}^2$  of the crystal, The infrared spectra were collected after dosing a gold film-covered

ZnSe crystal with 0.1 mM aliquots of DBN, then allowing to dry in air for ~ 5 minutes and rinsing it with benzene to remove any residual, weakly bonded molecules.

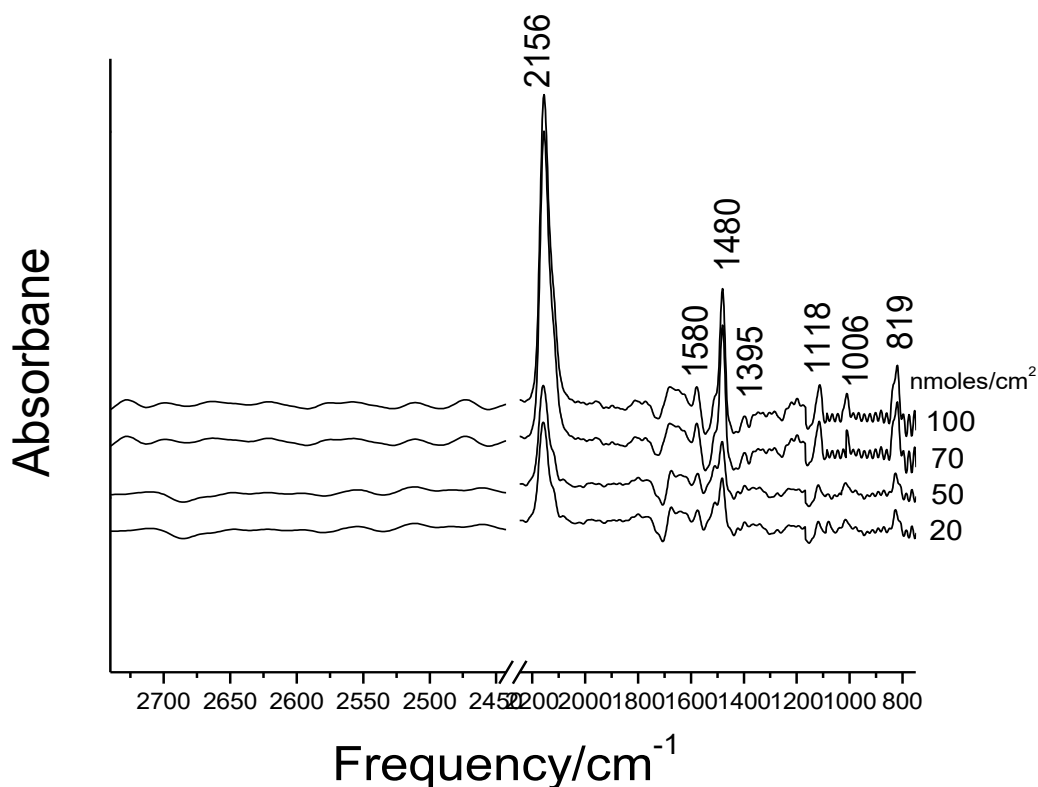


**Figure 8.5** A series of ATR infrared spectra of DBN adsorbed on a thin gold film using aliquots of 200  $\mu\text{l}$  of solution of 0.1 mM DBN. The resulting isocyanothiol doses, in mole/ $\text{cm}^2$ , are indicated adjacent to the corresponding spectrum. The inset is a spectrum of 0.1 mM solution of pure DBN in benzene

An intense mode in pure DBN is found at  $\sim 2123 \text{ cm}^{-1}$  due to the presence of a free  $\text{C}\equiv\text{N}$  mode, which disappears after adsorbing DBN on a gold film, while a peak at  $\sim 2156 \text{ cm}^{-1}$  appears that corresponds the formation of coordinated  $\text{C}\equiv\text{N}$  mode. Vibrational frequencies and

assignments of pure DBN in solution, and adsorbed on a gold nanoparticle array are summarized in *Table 8.1*, and compared with the spectrum of 1,4-BDT (*Chapter 5*).

Frequency (cm <sup>-1</sup> ) of 1,4-BDT adsorbed on gold film	Frequency (cm <sup>-1</sup> ) of DBN adsorbed on gold film	Assignment
804	819	B <sub>3u</sub>
1006	1006	B <sub>1u</sub>
1101	1118	B <sub>2u</sub>
1477	1480	B <sub>3u</sub>
1535	1580	B <sub>3u</sub>

**Table 8.1:** Comparison of vibrations of 1,4-BDT and DBN on gold film

## 8.4 Discussion

ATR-IR spectra for pure DBN appear to be a combination of what was reported for aromatic dithiols [2] and diisocyanides [3] where a vibrational mode at ~2123 cm<sup>-1</sup> is assigned to a free C≡N group. After forming DBN-linked gold nanoparticles, ring modes are still evident and drastic changes are noted for the C≡N modes, where the absence of the ~2123 cm<sup>-1</sup> peak after adsorbing on gold and the appearance of a ~2156 cm<sup>-1</sup> feature indicate that the adsorbed species contain gold-isocyanide modes. In addition, the agreement between the ring modes found for 1,4-BDT and DBN confirms that the ring is present on the surface, and the presence of predominantly B<sub>3u</sub> vibrations suggest that it lies close to parallel to the surface. However, the presence of small peaks at 1006 and 1118 cm<sup>-1</sup> implies that the molecular plane is slightly tilted. It is proposed that after adsorbing on a gold-nanoparticle film, the S-S bond breaks and a flat laying structure forms as shown in *Figure 8.6*.

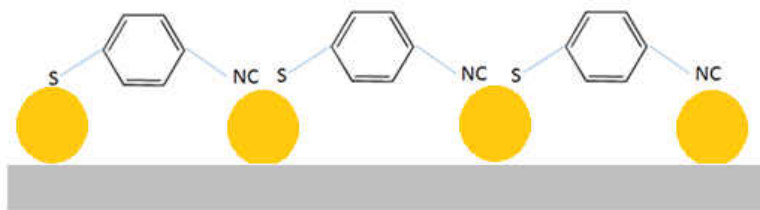


**Figure 8.6:** DBN after adsorbing on a gold nanoparticle array

Conductivity measurements as a function of BPDI dose from solution are shown in *Figure 8.1*. The initial conductivity of the nanoparticle array before dosing DBN was  $\sim 0.4$  nS. After dosing 0.03 mM DBN aliquots the conductivity increased gradually and reached  $\sim 155$  nS as a maximum measured value after dosing  $\sim 180$  nmoles/cm<sup>2</sup> of BPDI solution. At higher doses the conductivity did not change.

As shown in *Figure 8.3* the sheet resistance  $R$  varies with temperature as  $\ln(R)$  versus  $1/\sqrt{T}$ . As an indication of the formation of Au-DBN oligomers between nanoparticles, the values of  $\alpha$  scale linearly with  $\ln(R_0)$  and were obtained for  $\sim 8$  samples (*Figure 8.4*). The data showed that the slope of the alpha plot is equal to  $7.4 \pm 0.3$ . This slope value is nearly equal to the slopes obtained for 1,4-BDT ( $4.2 \pm 0.1$ ) [4] and 1,4-PDI ( $0.10 \pm 0.02$  eV) [5].

## 8.5 Conclusion

It was found that DBN molecule are capable of increasing the conductivity when dosing a gold-nanoparticle covered mica surface with DBN, which provides an evidence for the formation of similar one-dimensional chains as found for PDI and 1,3-BDT. The resistance varied as a function of the sample temperature, and the slope of alpha plot is equal to  $7.4 \pm 0.3$ . ATR-IR results showed the absence of the  $\sim 2123$  cm<sup>-1</sup> free isocyanide mode after adsorbing on gold and the appearance of bound  $\sim 2156$  cm<sup>-1</sup> isocyanide vibration modes indicating that the molecule

structure is parallel to the surface. It is proposed that DBN adsorbs on a gold-nanoparticle film by cleaving the S-S bond to form an asymmetric structure bound by sulfur and isocyanide groups to the gold nanoparticles. This offer the possibility of synthesizing asymmetric molecular electronic component.

## References

- [1] Abeles, B.; Sheng, P.; Coutts, M. D.; Arie, Y. *Advances in Physics* **1975**, *24*, 407
- [2] Noda, H.; Tai, Y.; Shaporenko, A.; Grunze, M.; Zharnikov, M. J. *Phys. Chem. B* **2005**, *109*, 22371-22376
- [3] Henderson, J. I.; Feng, S.; Bein, T.; Kubiak, C. P. *Langmuir* **2000**, *16*, 6183-6187
- [4] Kestell, J.; Abuflaha, R.; Garvey, M.; Tysoe W. T.; *J. Phys. Chem. C* **2015**, *119*, 23042–2305
- [5] Kestell, J.; Abuflaha, R.; Boscoboinik, J.; Bai, Y.; Bennett, D.; Tysoe, W.T.; *Chem. Comm.* **2012**, *49*, 1422-4.



# Chapter 9

## Back-Gate Modulation of Conductivity of Molecular Conductors

### 9.1 Introduction

This chapter details the results of investigations to modulate electronic transport through molecular wires in a field-effect transistor (FET), which is the basic building block for solid-state electronics. This device was first suggested in 1928 by Lilienfeld [1]. The first prototype of a working field-effect transistor was achieved in 1947 by John Bardeen, William Shockley and Walter Brittain [2]. In 1960, several transistors were combined in a single integrated circuit (*Figure 9.1*) [3].



**Figure 9.1:** a) The Lilienfeld transistor patent in 1930. B) The first prototype of a working field-effect transistor demonstrated by Bell labs. c) The first Integrated Circuit of Jack Kilby and Robert Noyce.

A field-effect transistor is a three-terminal electrical device that consists of a source, a drain and a gate. The source and the drain are in direct contact with a semiconductor, and the region

between these two contacts represents the channel. The semiconductor layer is separated from a gate electrode by a layer of an electronically insulating material [4].

The source electrode is grounded and can be used as a reference for the voltage applied to the gate and drain electrodes. The potential difference between the gate and the source is called the gate-source voltage ( $V_{GS}$ ). Similarly, the potential difference between the drain and the source is called drain-source voltage ( $V_{DS}$ ). By applying a potential to the gate electrode, charges can be generated at the insulator-semiconductor interface. A positive gate voltage induces negative charges (electrons) in the semiconductor, while a negative gate voltage induces positive charges (holes). These charges can increase the conductivity of the semiconductor, so that a conducting channel is formed between the source and the drain electrodes. A positively charged channel is doped with an acceptor impurity and a p-type material will be formed and the channel current will consist of holes. A negatively charged channel is doped with a donor impurity and an n-type material is formed and the channel current will consist of electrons [5,6].

N-channel devices generally have greater conductivity than p-channel types, because electrons have higher mobility than holes do; thus n-channel FETs are approximately twice as efficient conductors compared to their p-channel counterparts (*Figure 9.2*) [7].

The applied gate voltage has to exceed the minimum gate-to-source voltage differential that is needed to create a conducting path between the source and drain terminals, the so called threshold voltage ( $V_T$ ), before the channel becomes conductive.

Field-effect transistors have generally been used as unipolar devices, and this has limited the design of integrated circuits to unipolar complementary logic [8].

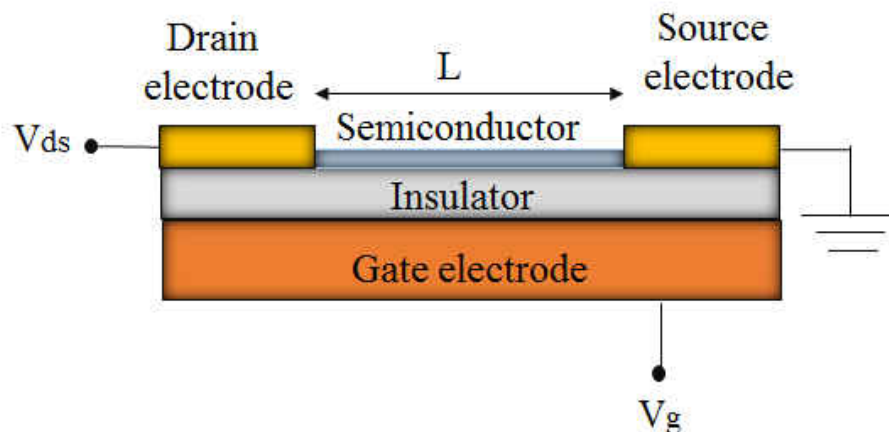


**Figure 9.2** A typical layout of field-effect transistor, consisting of a source and drain electrodes, a gate, a gate dielectric and a semiconductor

The first organic complementary logic circuits were created by combining p-channel and n-channel transistors. Two different semiconductors were used, one for the p-channel and one for the n-channel. Because of the difficulty of depositing and patterning both materials locally and sequentially, it was important to develop an ambipolar transistors based on a single semiconducting film and a single type of electrode [9].

Considerable efforts have been made to develop a single-electron transistor (SET), which can control the transport of only one electron. A SET is made of a metallic island that is connected to the source and drain electrodes through two tunneling junctions, and through a capacitor to the gate electrode. The current through the SET can be modulated by the gate electrode potential due to Coulomb blockade [10]. When there is no bias applied on the source or drain electrode, electrons in the system do not have enough energy to tunnel through the junction. On the other hand, increasing the gate bias will remove the Coulomb barrier and allow the electrons to tunnel through

junctions between the source and the drain; this is basically how the on/off switching system works in modern electronics (*Figure 9.3*) [11], and is discussed in greater details below.

The source and drain electrodes in the SET can be connected by a several-nanometers long single molecule where the electronic spectrum is quantized with the energy scale of  $\sim eV$  [12].

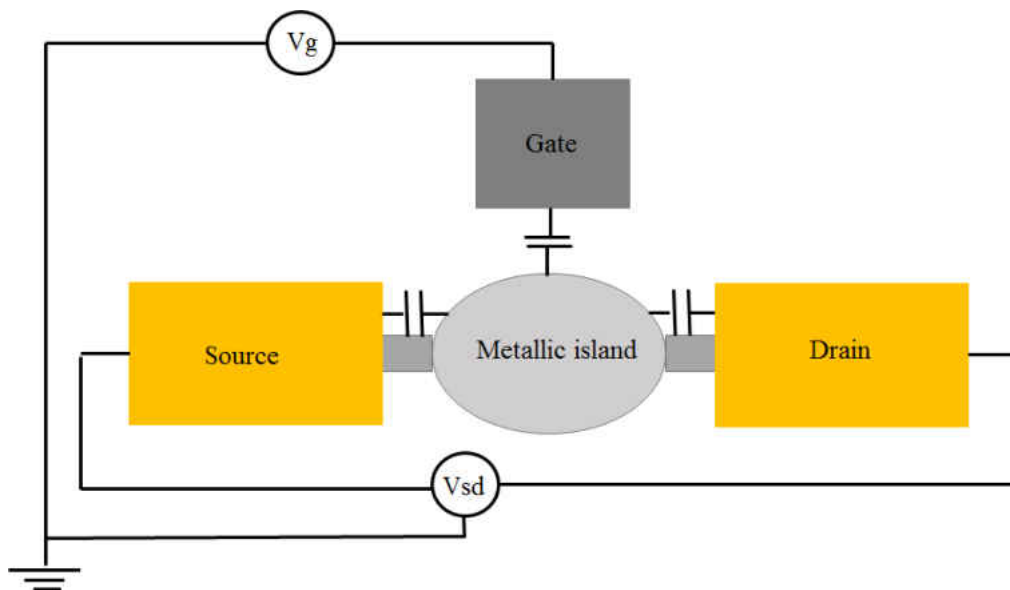


**Figure 9.3:** Schematic drawing of a single electron transistor with a metallic island that is isolated from the source, drain, and gate electrodes using a tunneling junction

Because of the lithography resolution, successful SET operation is possible at temperatures below 1 K [13]. Higher operating-temperature-range technologies are based on granular metallic nanoparticle arrays placed in the source-drain gap [14]. In this approach, the parameters of the SET critically depend on the metallic island size and position, and the way to avoid these problems is to use a structure with a large number of metallic nanoparticles (granules) that are statistically distributed in the gap between the source and the drain. In this case, the performance of the whole

system is independent of the individual metallic particle size or position, but is averaged over the space between the two electrodes. In this system, the current can still be controlled by an external electric field, and the electrons tunnel through the inter-granular tunnel junctions [15].

Two important parameters influence the electrical properties of such systems: the temperature, and the metal concentration. As the temperature increases, more charges exist in the film, and the conductivity increases by the means of single electron hopping [16]. At the same time, as the proportion of metal increases, the metallic islands grow and merge, so that the activation energy falls and the conductivity increases.

Molecular electronics is the study of charge transport through single molecules or through a monolayer of molecules, where the main goal of molecular electronics is to combine different types of functional molecules by self-assembly to form integrated circuits. Molecular electronics based on self-assembled alkane-thiols, for example, show that the resistance of gold/SAM/gold junctions depends on the molecular length and is independent of temperature, which means that the suggested charge transport mechanism is tunneling. In contrast, aromatic thiol molecular junctions are temperature dependent, which is consistent with the hopping mechanism of electron transport [17, 18].

In this study, an external field has been applied by a back-gated device in order to modulate the energy levels of molecular wires that bridge gold nanoparticles in a granular thin film. The external field should modulate the energy of the molecular orbitals of the molecular wire to influence their alignment with respect to the Fermi level of gold nanoparticles, thereby modulating the current through the molecular layer.

## 9.2 Theoretical aspects

In previous chapters, experiments have been performed to study the characteristics of electrical conduction in the granular regime, where all films studied showed a decrease of resistance with increasing temperature. The linear  $\ln(R)$  versus  $T^{-1/2}$  dependence is predicted by Abeles theory of thermally assisted tunneling through a granular material [19], where the conductivity depends on the size and the separation of gold nanoparticles.

On the other hand, electrical conduction in granular metals in the regime of activated conductivity is generally discussed in terms of the model of Neugebauer and Webb [20]. In this chapter, electrical characteristics are presented for granular gold films in which the conductivity was modified by a back-gate field effect. During measurements grains are charged capacitatively from the back-gate, where the charge in the grain is induced by contacting the gold electrodes. *Figure 4* shows the sample configuration for the field effect measurements.

In *Figure 9.4a*,  $C_1$  represents the capacitance between the gate electrode and the grain, and  $C_2$  the capacitance between the grain and the rest of the film,  $C_2 \gg C_1$  and  $V_g$  is the gate voltage. The grains are taken to be uniform in size and separation and therefore have identical capacitance. The two capacitor plates connected to A represent a grain and the total charge on them must be an integral number of elementary electronic charges. If A and B electrodes are connected together, and  $V_g$  increases,  $C_1$  charges reversibly and the system energy remains constant. At an arbitrary  $V_g$  the charge at A will not be an integral number of elementary charges, but will differ by  $\delta$  from the nearest integer, so that, by applying a voltage across AB, the system can be adjusted to form an integral charge on A according to the following equation [21]

$$\frac{\partial V_A}{\partial Q_A} = \frac{1}{c_1} + \frac{1}{c_2} = \frac{1}{c'} \quad (1)$$

The work done in inducing the charge is

$$dW = \frac{\delta^2 e^2}{2C'} = \delta^2 E_C \quad (2)$$

where  $E_C$  is the charging energy, discussed in the Abeles model (*Chapter 3*).

As illustrated in *Figure 9.4b*, for a given charge state of the grain, the system energy increases quadratically with the gate voltage, for example, the parabolic curve centered at 2 corresponds to the energy of charge state  $n = +2$  electrons for various  $V_g$  values [21].

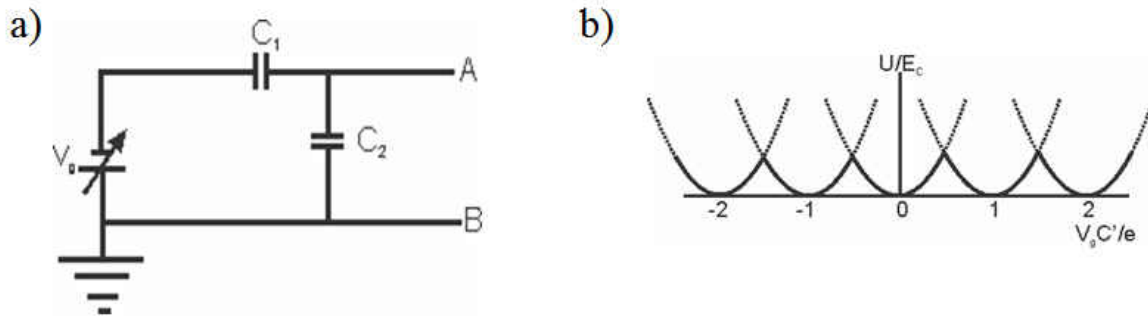


**Figure 9.4:** a) Simplified model for gain charging. b) Energy of different charge states as a function of gate voltage

However, in the experimentally used gold nanoparticle arrays on mica, there will be a distribution of particle distances,  $d$  and separation  $s$ . This means that there will be a distribution of  $C_2$  values so that the voltages at which a unit of charge is transferred will be different for each of them. Thus, it is anticipated that a regular Coulomb blockade, as shown in *Figure 4.4b* will not be observed. Rather the effect of modulation will be expected to initially increase from zero bias but then average out as different nanoparticle capacitor change at different rates.

In addition, the electric field is also expected to polarize the linker molecule to change the tunneling barrier.

These ideas are tested in the following for some of the molecular layers that bridge between gold nanoparticles described in previous chapters.

### **9.3 Device fabrication and experimental setup**

For this study, commercially made silicon dioxide films were used, where p- and n-doped silicon wafers were thermally oxidized to generate a SiO<sub>2</sub> film (300 nm thick) functioning as a gate dielectric.

A 1cm×1cm SiO<sub>2</sub> substrate was used, and two copper wires were glued to the substrate using conductive silver glue, and then the sample was left on a hot plate at ~ 40 °C for one hour to allow the glue to dry. After the glue had dried, small pads of nickel-chrome were added as an adhesion layer for the gold electrodes.

Nickel-chrome pads were deposited as an adhesion layer for the gold pads, by masking the central portion of the silicon substrate (dielectric) and placing it inside the vacuum evaporator and depositing a ~20 nm-thick nickel-chrome alloy film, exactly the same way as when depositing gold pads. Gold source-drain electrodes were fabricated by evaporating ~200 nm-thick gold pads on top of the nickel-chrome film using the thermal evaporator with 99.999% purity gold (Metal-Basis, Alfa-Aesar) by passing a current of ~ 60 A through the tungsten filament. After the gold pads were deposited, the sample was removed from the evaporator, the mask was removed, and then the gold pads were attached to smooth alligator clips inside the evaporator in order to monitor the resistance change while depositing gold nanoparticles on the mica substrate. After placing the sample into the chamber and pumping the evaporator to ~10<sup>-8</sup> Torr, the deposition was carried out



by passing a  $\sim 20$  A current through the tungsten filament, and a copper, back-gate (field) electrode, to which a potential may be applied to induce the charge on the granular film, was attached to the bottom of the substrate using an insulating clip (Figure 9.5).

These back-gated devices function in air; however, to minimize charge trapping by water or oxygen and to allow the samples to be cooled, all measurements were performed in vacuum. In this work, the semiconductor layer in the field-effect transistor is replaced by small organic molecules.

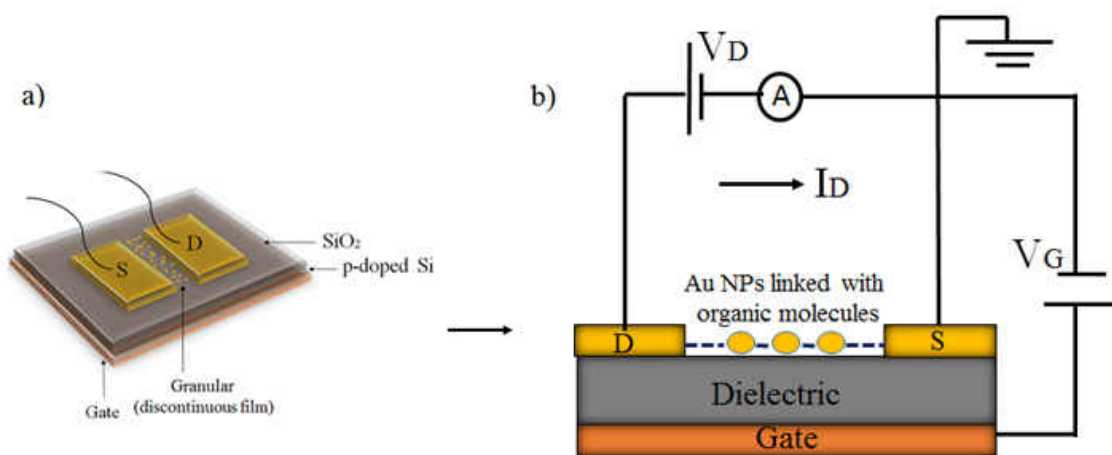


**Figure 9.5** a) Sample configuration for field effect measurements. b) Experimental setup for the field-effect device where the gold nanoparticles are linked with organic molecules.

In this work, the organic compounds used for back-gated device measurements were: 1,4-BDT, 1,3- BDT, and 1,4-PDI.

It has been shown previously that these organic molecules are capable of forming molecular electronic linkages between the deposited gold nanoparticles (*Chapter 3*) which results

in an increase the initial conductivity on a mica surface and, as shown below, similar behavior was observed on a SiO<sub>2</sub> surface. The samples were prepared by evaporating a gold nanoparticle array in a vacuum evaporator and after aging, the films were dosed in two different ways; first, vacuum (in-situ) dosing was carried out, where the silicon oxide substrate covered with gold nanoparticle arrays was placed inside the HV chamber and the 1,4-PDI molecules were dosed directly from the Knudsen source (see section 2.3). Second, they were obtained by dosing the organic compound from solution after dissolving in benzene after the resistance value had stabilized. The film was then washed with pure benzene to remove any excess molecules, and the sample was attached to the sample manipulator and placed in the HV chamber.

Back-gating field-effect devices were fabricated based on 1,4-BDT, 1,3-BDT, and 1,4-PDI, and they show an ambipolar behavior under gate bias. The gate bias is coupled capacitively to the thin film under investigation. The current-voltage characteristics were measured by Keithley 4200 picoameter under vacuum at different temperatures.

## 9.4 Results

All samples studied showed an ambipolar field effect at about zero applied gate voltage. For example, a sample was prepared by depositing gold nanoparticles with an initial conductivity of 1.5 nS. Dosing 1,4-PDI from the gas phase was performed via a directional dosing source. The substrate was mounted on the sample holder in way to be electrically connected through the vacuum feedthrough, and the chamber was pumped to  $\sim 10^{-8}$  Torr, then the 1,4-PDI was dosed (in-situ) until the resistivity of the last two consecutive points were within  $\sim 2\%$  of each other (*Figure 9.6*).

The temperature variation of the gold-nanoparticle-covered SiO<sub>2</sub> samples dosed with 1,4-PDI are plotted as  $\ln(R)$  vs.  $T^{-1/2}$  (*Figure 9.7*) which is predicted by Abeles theory [19] for thermally

assisted tunneling through granular materials, which provides evidence for the formation of oligomeric bridges between gold nanoparticles on silica as described previous for 1,4-PDI on mica substrates (*Chapter 3*).

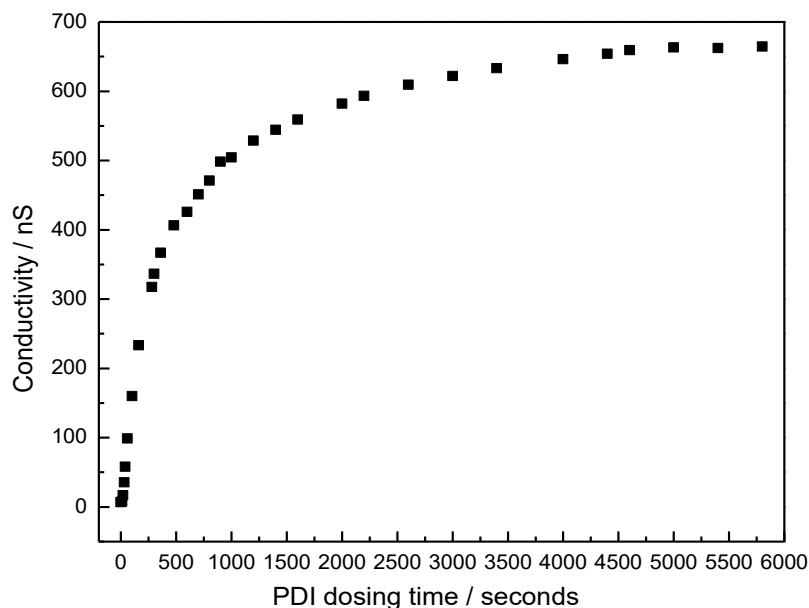


**Figure 9.6:** Typical curve showing dramatic enhancement in conductivity across a granular film as a function of 1,4-PDI dosing

The current was measured at source-drain voltages,  $V_{SD}$  of 0.751 and 1.404 V, as a function of the gate voltages from -70 to +70 V, at a sample temperature of 110 K in high vacuum (*Figure 9.8*). The ratio  $I_{SD}/I_{SD}(0V)$  is plotted versus the applied gate voltage so that, the ratio is unity at 0V gate voltage. The curves show identical behavior at  $V_{SD} = 0.751$  and 1.404 V because of the Ohmic behavior of the granular film.

This reveals that the application of the gate voltage has a measurable effect on the conductivity, which changes by a maximum of ~1.5 to 2.3% at the maximum values of applied gate voltages.

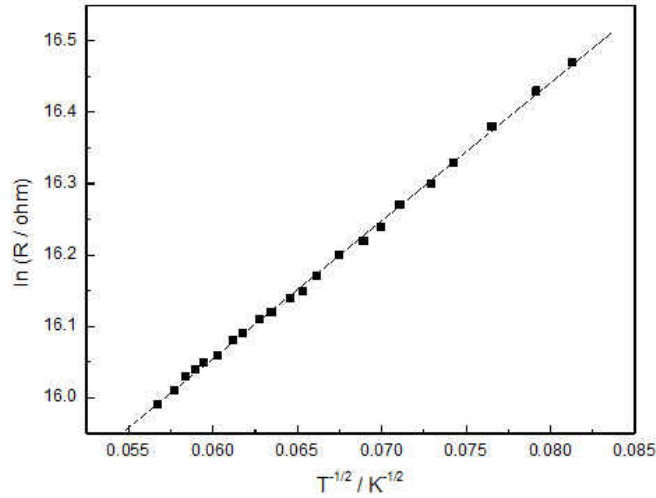


**Figure 9.7:** Temperature dependence of a granular gold film with 1,4-phenylene diisocyanide (1,4-PDI linkers) in a field-effect device

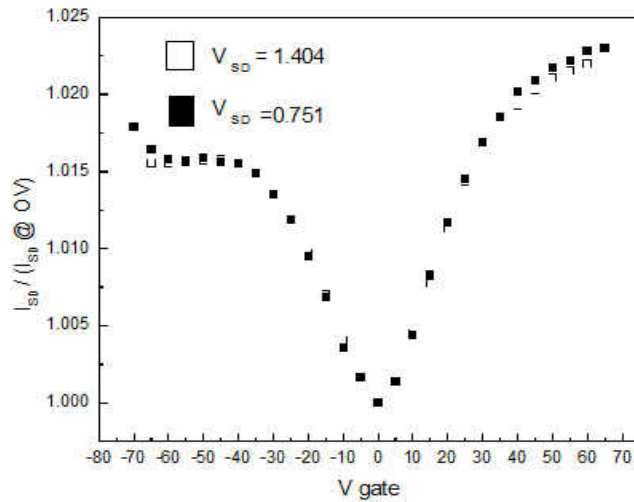


**Figure 9.8:** An ambipolar field-effect in a granular gold film with 1,4-phenylene diisocyanide (1,4-PDI linkers), at ~110 K

Similar back-gated devices were also prepared on a silicon oxide substrate by bridging gold nanoparticles with 1,4-BDT and 1,3-BDT molecules from solution which caused a profound reduction in sheet resistance across the films, where this high conductivity enhancement is a consequence of bridging gold nanoparticles with conductive molecular wires (*Chapter 5*).

Experiments were carried out using 1,4-BDT, which was dosed using a 5mM solution in benzene, after which the sample was washed with benzene and allowed to dry. In this experiment, it was more convenient to dose the sample from solution, because 1,4-BDT cannot sublime as quickly as 1,4-PDI at room temperature in vacuum. Dosing 1,4-PDI until sample saturation required less than three hours, while dosing 1,4-BDT required much longer time, and the HV chamber can be contaminated by sulfur which requires the chamber to be baked in order to clean it. As a consequence, 1,4-BDT molecules were dosed from solution until the sheet resistance changed from an initial value of 813 M $\Omega$  to 10.74 M $\Omega$  after dosing the film with 1,4-BDT at room temperature. The change in resistance relative to the resistance at 0V gate bias, ratioed to the resistance at 0V gate bias ( $(R_{\text{gate}}-R_0)/R_0$ ) is plotted in *Figure 9.9a*. The sample temperature clearly had a significant effect on the back-gating behavior. At a sample temperature of  $\sim 110\text{K}$ , the sheet resistance changed by  $\sim 2.5\%$  with a positive gate voltage and by 4.5% under a negative bias. However, the effect is smaller and the influence of gate voltage is much closer to linear for a sample held at room temperature.

This theory predicts a quadratic dependence of conductivity versus gate voltage as a direct consequence of generating charge carriers by modulating  $E_C$  (*Equation 2*). This quadratic change is shown schematically in *Figure 9.9b*. However, the experimental data also show an additional, approximately linear behavior. It is suggested that the linear component corresponds to the modulation of the energy levels (in this case oligomers) that are coupled to the gold nanoparticles.

The gating properties of 1,3-benzene dithiol (1,3-BDT) were tested in the same way and the results shown in *Figure 9.10* for 1,3-BDT linkers between gold nanoparticles on SiO<sub>2</sub> films. The sample was again dosed using a 5 mM solution of 1,3-BDT in benzene. The results (as shown in *Figure 9.10*), exhibit the same behavior as that found for 1,4-BDT (*Figure 9.9*). The response as a function of gate voltage is approximately linear at room temperature with a parabolic + linear behavior at ~95K. However, the overall response of 1,3-BDT-dosed nanoparticle arrays is less than 1,4-BDT-dosed samples. The relative change in resistance is ~1% at positive gate voltage and ~1.4% at negative bias.

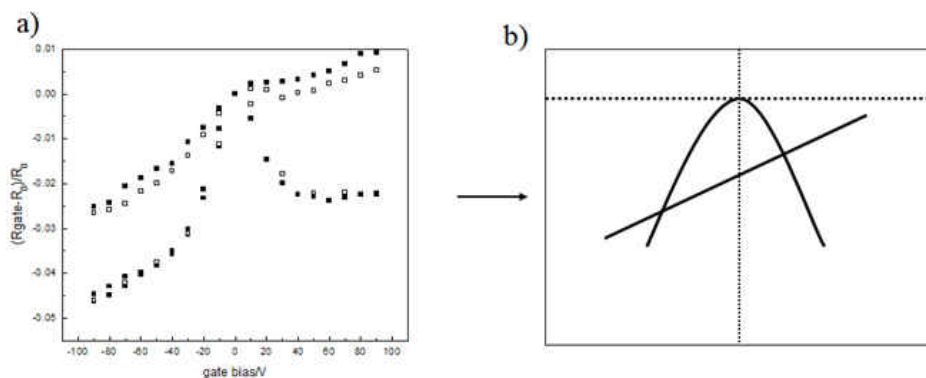


**Figure 9.9:** 1,4-BDT dosed film (813 M $\Omega$   $\rightarrow$  10.74 M $\Omega$ ). a) Upper curve acquired at room temperature. The lower curve acquired at ~110K. b) Proposed theoretical prediction of a quadratic dependence of charge state energy as a function of gate voltage, and a linear component that corresponds to a change in energy alignment compared to the gold Fermi levels.

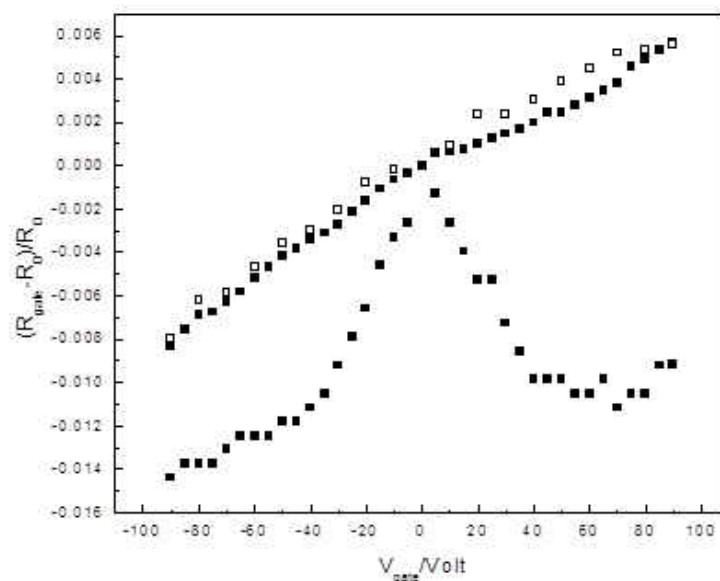


**Figure 9.10:** 1,3-BDT dosed film (235 MΩ → 25.10 MΩ). The upper curve was acquired at room temperature. The lower curve acquired at ~95 K.

## 9.5 Discussion

In this study, efforts have been made to develop methods towards integrating the Au/organic linker self-assembly chemistry with standard fabrication techniques based on silicon oxide, and to explore their back-gating behavior. The field-effect conductivity data for three samples showed that the resistance falls from a maximum value with increasing gate potential of either sign. However, the change in conductivity is very small. For the 1,4-PDI linked gold nanoparticles, the maximum values of applied gate voltage have a measurable effect on the conductivity, with changes by a maximum of ~1.5 to 2.3%. Similar experiments were carried out using 1,4-BDT, the sample temperature had a significant effect on the back-gating behavior. The field effect was very small and close to linear at room temperature, so that, at a sample temperature of ~110K, the sheet resistance changed by ~2.5% with a positive gate voltage and by 4.5% under

a negative bias. Similarly, for the 1,3-BDT linkers between gold nanoparticles on SiO<sub>2</sub> films, the overall response of 1,3-BDT-dosed nanoparticle arrays is less than 1,4-BDT-dosed samples. The relative change in resistance is  $\sim 1\%$  at positive gate voltage and  $\sim 1.4\%$  at negative bias, and the response of resistance as a function of gate voltage is approximately linear at room temperature.

The shapes of the curves of variation in resistance show a temperature-dependent parabolic behavior and a linear response, as suggested in *section 9.2*. The parabolic response arises from the influence of the external field on the charges on the gold nanoparticles to form a Coulomb blockade. The current due to this Coulomb charging energy is expected to depend on temperature (*Eqn. 9*). That gives rise to the temperature dependence in the Abeles model (*Section 3.4.1*)

Another possible explanation for the low potential effect can be the slow dielectric relaxation process that allows some adjustment of each island to its equilibrium charge state, this slightly lowers the energy of the ground state with respect to the excited states and reduces the conductivity [21].

The linear, temperature-independent part of the variation in current with gate voltage is proposed to occur because of the shift in energy of the orbitals closest to the Fermi level that results in a modulation of the tunneling barrier, which is temperature independent. The observation that the conductivity increases at a positive bias for PDI, 1,4-BDT and 1,3-BDT suggests that the tunneling barrier is reduced in all cases for positive voltages.

## 9.6 Conclusion

Back-gating behavior has been explored for three different devices. The field effect conductivity results showed a small increase in the conductivity with increasing the gate potential of either sign. Electrical measurements were performed using 1,4-PDI-, 1,4-BDT- and 1,3-BDT-



linked gold nanoparticles, maximum sheet resistance changes were ~1.5 to 2.3%. At a sample temperature of ~110K, the sheet resistance changed by 4.5% under a negative bias, and the results can be rationalized by a combination of Coulomb blockade effects and polarization of linker molecules.

## References

- [1] Lilienfeld, J. E.; Patent, Jan. 28, **1930**
- [2] Riordan, M.; Hoddeson, L.; Herring, C.; Reviews of Modern Physics. **1999**, *71*, No. 2
- [3] Kilby, J.; Nobel lecture, December 8, **2000**
- [4] Hayes & Horowitz. ECE60L Lecture Notes. Spring **2002** (pp 142-162 and 244-266)
- [5] Orsi, S.; Universit\_e de Gen\_eve, October **2009**
- [6] Field Effect Transistors in Theory and Practice. Freescale Semiconductor, Inc. **1993, 2009**
- [7] Pasupathy, A. N.; PhD Dissertation. Cornell University, **2004**
- [8] Feng, T.; Xie, D.; Lin, Y.; Tian, H.; Zhao, H.; Ren, T.; Zhu, H. Applied Physics Letters. **2012**. 101, 253505
- [9] Park, J.; B.S. thesis. **1996**, Seoul National University.
- [10] A. Fuhrer, Ph.D. thesis, 2003, Swiss Federal Institute of Technology.
- [11] Kumar, A.; Dubey, D. Advance in Electronic and Electric Engineering. **2013**, *3*, 57-62
- [12] Yu. A. Pashkin, Y. Nakamura, and J.S. Tsai, Appl. Phys. Lett. 2000, **76**, 2256
- [13] Likharev, K. K.; IEEE Trans.Magn. **1987**, *23*, 1142
- [14] Zakheimn, D. A.; Rozhansky, I. V.; Smirnova, I. P.; Gurevich, S. A.; Nanostructures: Physics and Technology. **2001**, OAN.09p , 10-18
- [15] Simmons, G. J.; J. Phys. D: Appl. Phys., **1971**, *4*.
- [16] Zakhe, D. A.; Rozhansky, I. V.; Smirnova, I. P.; Gurevich, S. A. Journal of Experimental and Theoretical Physics. **2000**, *91*
- [17] Joachim, C.; Ratner, M. A. PNAS. **2005**, *102*

[18] Nelson, S. F. *Applied Physics Letters*. **1998**. 72

[19] Abeles, B.; Sheng, P.; Coutts, M. D.; Arie, Y. *Advances in Physics* **1975**, 24, 407.

[20] Neugebauer, C. A.; Webb, M. B.; *Journal of Applied Physics*. **1962**, 33, 74.

[21] Adkins, C.J. et. al. *J. Phys. C: Solid State Phys.* 1984, 17

# Chapter 10

## Conclusions

In the 1970s, when top-down integrated circuits still had fairly large dimensions, making electronic circuits by bottom-up techniques using molecules as electronic components was first seriously discussed. At that time, one of the major advantages of molecular electronics was said to be that it would result in circuits much denser than those possible by “top-down” technology [1]. Although great advances have been made using top-down fabrication, some critical components, like the gate oxides, are now only a few atoms thick. However, their lateral dimensions are larger. As a consequence, the idea of a “bottom up” approach was proposed, where the position of every atom in the device is known and the devices can be optimized on the atomic scale. This approach provides the possibility of making transistors by chemical synthesis, which means more transistors will be made in one day than will ever be made by photolithography. This could result in the cost per transistor dropping by orders of magnitude, which is consistent with Gordon Moore’s prediction [2].

The first and simplest molecular device was proposed in 1974 by Aviram and Ratner, who introduced a model consisting of a donor  $\pi$ -system and an acceptor  $\pi$ -system, separated by a  $\sigma$ -bonded tunnelling bridge (see *Figure 1.1*). This system could then, theoretically, be attached at both ends to metallic electrodes thereby completing an electric circuit. Aviram and Ratner predicted that the properties of this ‘molecular rectifier’ must be equivalent to those of the bulk p-n junction. In the donor-insulator-acceptor (D- $\sigma$ -A) structure, the highest occupied molecular orbital (HOMO) and the lowest unoccupied molecular orbital (LUMO) are confined to two different parts of the rectifier and the insulating  $\sigma$  bridge prevents the orbitals from overlapping.

By placing such a molecule between two metallic electrodes and applying voltage in the positive direction, the Fermi level of the electrode on A (cathode) aligns with the LUMO allowing electron tunnelling from the Fermi level to the LUMO. Simultaneously, the D side aligns with the HOMO, resulting in electron transfer from the HOMO to the Fermi level of the electrode on D (anode).

In this work, efforts have been made to study the electrical properties and surface structures for organic linkers bridging between a gold nanoparticle arrays. The main goal is to link gold nanoparticles between two gold electrodes with organic molecules, and align the gold Fermi level with the organic molecules' energy levels to control height of the electron tunneling barrier. Such tuned, self-assembled molecular connections could provide the basis for fabricating molecular electronic devices.

To apply this idea, different isocyanide- and sulfur- terminated aromatic molecules were used to link gold nanoparticle arrays deposited between 300 nm-thick gold electrodes on a mica substrate. It was found that diisocyanides and dithiols with one, two, and three benzene rings can form oligomeric chains on gold nanoparticle arrays in order to decrease the tunneling barrier and enhance the conductivity. The results showed that these molecules generally form oligomer bridges when dosed on gold-nanoparticle arrays, and that the conductivity can be affected by the number of phenyl rings for each molecule. However it was observed that the tunneling barrier increased by increasing the molecular length (number of benzene rings). Slopes derived from plots of the temperature dependence of the conductivity for benzene dithiol (BDT), biphenyl dithiol (BPDT), and terphenyl dithiol (TPDT) show that the height of the tunneling barrier increases with increasing number of benzene rings, which means that increased extent of conjugation does not necessarily lead to higher current. The biphenyl and terphenyl molecules can adopt a twisted ring configuration which appear to be observed for BPDT and TPDT. This distortion decreases the

conjugation by reducing the orbital overlap between the aromatic rings. Therefore, the poly-phenyl dithiol molecules are not expected to be as conductive as benzene dithiol (*Chapter 6*). Similar to dithiols, the energy barrier of diisocyanides increased by increasing the number of phenyl rings either because of the increasing  $\pi$  orbitals associated with increasing the number of phenyl rings which increases the electron donation to the gold, that leaves a partial positive charge on the isocyanide molecule which leads to lowering the molecular orbital energies and moves the HOMO orbital away from the Fermi level, or alternatively by twisting of the rings as found for dithiols (*Chapter 7*).

An asymmetric molecule with both isocyanide and sulfur terminated groups was investigated by studying the surface structure and electrical properties after dosing gold films with 4,4'-disulfanediyldibenzoisonitrile (DBN) from solution. As a result, DBN has ability to form oligomers between gold nanoparticles and results in the formation of an asymmetric linker molecule. The ATR-IR spectra provide information that is complementary to electrical measurements, and allow the surface structure of DBN molecules on the gold-nanoparticle array to be determined.

In *Chapter 9*, back-gating behavior has been explored for three different devices. The field effect conductivity results showed a small increase in the conductivity with increasing the gate potential of either sign. Electrical measurements were performed using 1,4-PDI-, 1,4-BDT- and 1,3-BDT-linked gold nanoparticles, maximum sheet resistance changes were  $\sim 1.5$  to 2.3%. At a sample temperature of  $\sim 110$ K, the sheet resistance changed by 4.5% under a negative bias.

These results confirm that both isocyanide- and sulfur-terminated molecules can self-assemble to form molecules linkages between gold nanoelectrodes either on mica or on silica substrates. The tunneling barrier can be tuned by changing the number of rings in the linker

backbones, and this approach can also be used to link nanoparticles with asymmetric molecules. Finally, preliminary experiments show that the conductivity can also be modulated by applying a back-gate voltage. These results suggest that such a self-assembly chemistry involving isocyanide- and sulfur-terminated molecules could form the basis for fabricating nanoscale, molecular electronic circuits.

## References

- [1] A. Aviram and M. A. Ratner, "Molecular rectifiers," Chem. Phys. Lett. vol. 29 pp. 277-283, **1974**.
- [2] Moore, Gordon E. (1965-04-19). "Cramming more components onto integrated circuits". Electronics. Retrieved **2016-07-01**
- [3] For an overview of single-electron devices and their applications, see: K. K. Likharev, Proceedings of the IEEE 87p. 606 (**1999**).

# CURRICULUM VITAE

Rasha K. Abuflaha

Place of birth: Tuzla, Bosna and Herzegovina

## **Educational Background**

- 2011 – 2016** Ph.D. Candidate, Physical Chemistry, Department of Chemistry and Biochemistry, University of Wisconsin-Milwaukee, USA.  
Advisor: Distinguished Professor W. T. Tysoc  
Thesis title: “Electrical Measurements and Attenuated Total Reflection Infrared Spectroscopic Study of Aromatic Isocyanides and Thiols on Gold”.
- 2006 – 2009** M.Sc. Physical Chemistry, Al-albays University, Jordan  
Thesis title: “Preparation and Characterization of New Lipooligosaccharide Chitosan Derivatives”.
- 2002 – 2006** B.Sc. Chemistry, Al-albays University, Jordan

## **Employment Background**

- 2016 - Present** Research Assistant, Surface Chemistry, University of Wisconsin Milwaukee, Department of Chemistry and Biochemistry USA
- 2015 - 2016** Teaching Assistant, General Chemistry, University of Wisconsin Milwaukee, Department of Chemistry and Biochemistry, USA
- 2009 - 2011** Organic Analyses Laboratory Supervisor, Al-albays University, Department of Chemistry, Jordan
- 2008 - 2009** Shale Oil Extraction and Purification Project, Al-albays University, Arid Regions Research Center, Jordan.

**2007 - 2008** Undergraduate Physical Chemistry Laboratory Supervisor, Al-albait University, Department of Chemistry, Jordan.

### **Experience**

Ultrahigh Vacuum (UHV) Technology

Auger Electron Spectroscopy (AES) in Ultrahigh Vacuum

Temperature-Programmed Desorption (TPD) in Ultrahigh Vacuum

Scanning Tunneling Microscopy (STM) in Ultrahigh Vacuum

Thin Film Preparation

Attenuated total reflection Infra-red (ATR-IR) Spectroscopy

Nuclear Magnetic Resonance: ( $^1\text{H}$ -NMR) spectroscopy

Fourier Transformation Infra-red: (FT-IR) spectroscopy

Gas Chromatography-Mass Spectroscopy (GC-MS)

Elemental Analysis (EA)

Differential Scanning Calorimeter (DSC)

Surface Tensiometer

UV-visible spectrophotometers

Column Chromatography

Organic Synthesis (Substitution Reactions)

### **Scholarships**

Received a four-year scholarship (2011-2015) from Al al-bait University to get the Ph.D in Physical Chemistry from the University of Wisconsin-Milwaukee. Department of Chemistry and Biochemistry.

### **Professional Affiliations**

Member of the American Chemical Society (ACS), USA



## **Publications**

Kestell, J.; **Abuflaha, R.**; Boscoboinik, J. A.; Bai, Y.; Bennett, D. W.; Tysoe, W. T. Linking gold nanoparticles with conductive 1,4-phenylene diisocyanide-gold oligomers. *Chemical Communications*. **2013**, 49, 1422–1424.

Garvey, M.; Kestell, J.; **Abuflaha, R.**; Bennett, D. W.; Henkelman, G.; Tysoe, W. T. Understanding and controlling the 1,4-phenylene diisocyanide–gold oligomer formation Pathways. *Journal of Physical Chemistry*. **2014**, 118, 20899–20907.

Kestell, J.; **Abuflaha, R.**; Boscoboinik, J. A.; Garvey, M.; Bennett, D. W.; Tysoe, W. T. Determination of adsorbate structures from 1,4-phenylenediisocyanide on gold. *Journal of Physical Chemistry letters*. **2014**, 5, 3577–3581.

Kestell, J.; **Abuflaha, R.**; Garvey, M.; Tysoe, W. T. Self-Assembled Oligomeric Structures from 1,4-Benzenedithiol on Au(111) and the Formation of Conductive Linkers between Gold Nanoparticles. *Journal of Physical Chemistry*. **2015**, 119, 23042–23051

**Abuflaha, R.**; Olson, D.; Bennett, D. W.; Tysoe, W. T. Surface chemistry and structures of 1,4-phenylene diisocyanide on gold films from solution. *Surface Science*. **2016**, 649, 56-59.

Kestell, J.; **Abuflaha, R.**; Tysoe, W. T. Surface Structure and Electrical Conductivity of 1,3-Benzenedithiol on Au (111). *In Preparation*.

**Abuflaha, R.**; Tysoe, W. T. Surface Chemistry and Electron Transport of Biphenyl-4,4'-Diisocyanide and Biphenyl-4,4'-Dithiol on gold films from solution. *In Preparation*.

**Abuflaha, R.**; Tysoe, W. T. Surface chemistry and Electrical Measurements of Terphenyl-4,4'-Dithiol on gold films from solution. *In Preparation*.

**Abuflaha, R.**; Tysoe, W. T. Asymmetric Electron Linker Molecule and Conductivity Measurements of 4,4'-Disulfaneyldibenzoisonitriol on gold films from solution. *In Preparation*